

ABSTRACT

Title of Dissertation:

**THE ROLE OF THE F SPIN-ORBIT
EXCITED STATE IN THE F+H₂ AND
F+HD REACTIONS**

Yi-Ren Tzeng, Ph.D., 2004

Dissertation Directed By:

**Professor Millard H. Alexander, Department
of Biochemistry and Chemistry and Chemical
Physics Program**

In this dissertation we study the role of the F spin-orbit excited state (F*) in the F+H₂ and F+HD reactions using quantum mechanical calculations. The calculations involve multiple potential energy surfaces (the Alexander-Stark-Werner, or ASW, PESs), and include an accurate treatment of the couplings (non-adiabatic, spin-orbit, and Coriolis) among all three electronic states.

For the F+H₂ reaction, we calculate the center-of-mass differential cross sections and laboratory-frame angular distributions at the four different combinations of collision energies and hydrogen isotopomer investigated in the experiments of Neumark *et al.* [J. Chem. Phys., **82**, 3045 (1985)]. Comparisons with the calculations on the Stark-Werner (SW) and Hartke-Stark-Werner (HSW) PESs, which are limited to the lowest electronically adiabatic state, show that non-adiabatic couplings greatly reduce backward scattering. Surprisingly, we find the shapes of both the CM DCSs and LAB ADs are insensitive to the fraction of F* presented in the F beam.

For the F+HD reaction, we calculate the excitation functions and product translational energy distribution functions to study the reactivity of F*. Comparisons with the experiment by Liu and co-workers [J. Chem. Phys., **113**, 3633 (2000)] confirm the relatively low reactivity of spin-orbit excited state (F*) atoms. Excellent

agreement with the experiment is obtained under the assumption that the F*:F concentration ratio equals 0.16:0.84 in the molecular beam, which corresponds to a thermal equilibrium of the two spin-orbit states at the experimental temperature (600K). From the accurate calculation of the F* reactivity and its relatively small contribution to the overall reactivity of the reaction, we attribute discrepancies between calculation and experiment to an inadequacy in the simulation of the reactivity of the F ground state, likely a result of the residual errors in the ground electronic potential energy surface.

THE ROLE OF THE F SPIN-ORBIT EXCITED STATE IN THE F+H₂ AND F+HD
REACTIONS

By

Yi-Ren Tzeng

Dissertation submitted to the Faculty of the Graduate School of the
University of Maryland, College Park, in partial fulfillment
of the requirements for the degree of
Doctor of Philosophy
2004

Advisory Committee:
Professor Millard H. Alexander, Chair
Dr. Charles W. Clark
Professor Paul J. Dagdigan
Professor Xiangdong Ji
Professor Robert A. Walker
Professor John D. Weeks

© Copyright by
Yi-Ren Tzeng
2004

Dedication

To my family

Acknowledgements

It is always an emotional moment to look back when a long and challenging journey comes to an end. Through the years I have received help from numerous people, but I have not yet expressed my gratitude for their support. I am very happy to have this opportunity to thank my dear friends.

With great appreciation, I would like first to thank my advisor, Millard Alexander, for having given me the chance to do theoretical calculations on chemical reactions that combined chemistry, physics, mathematics, and programming into my dream research topic. Studying chemical reactions is not an easy task and it was especially challenging for me. Thanks to Dr. Alexander's great patience and consideration, I have learned numerical calculations and computational skills, as well as various techniques in quantum chemistry, while wandering through this extremely complex and dynamic research field. Not only has he reshaped my understanding of what good research is, but he has also taught me by his own example how to face up to difficult challenges and fulfill high expectations. Every sentence and each word in this dissertation are the result of his advising. Without his guidance I could never have gone so far, and this dissertation would not even exist.

It is a great honor to have had the chance to cooperate with several outstanding scientists through my research experience. Professor Paul Dagdigian of Johns Hopkins University has been a long time friend and ally of our research group. We coauthored two papers. This was a valuable experience for me. Professors Javier Aoiz of Universidad Complutense and Bruno Martínez-Haya of Universidad Pablo de Olavide have generously offered us their (Center-of-Mass)-to-(Laboratory) angular distribution transformation package to obtain the LAB AD simulations in Figs. 3.8-3.11. Professor Kopin Liu of Academia Sinica helped us to better understand the

experimental data shown in Chapters 4 and 5. Thanks also to Dr. David Manolopoulos of Oxford University and Professor Millard Alexander of the University of Maryland for providing the scattering codes that made my research possible.

Several people have helped me overcome the biggest challenge in my life so far. I want to thank Professor Ellen Williams, who introduced me to the Chemical Physics program at the University of Maryland six years ago. Since then, I have enjoyed every aspect of my experience here. I also want to thank Professor Michael Coplan, the director of our program, who has enthusiastically devoted himself to mentoring all the first-year students and who continues to offer support afterward. I am one of many students who have benefited from his advice. Dr. Charles Clark of the National Institute of Standard and Technology (NIST), together with Professor Coplan and others from UMCP and NIST, organized special problem-solving sessions to help us prepare for the challenging qualifying exams. His critical thinking and inspiring questioning helped me understand several key concepts in physics that I had failed to grasp in the past. Special thanks to Professor Xiangdong Ji for his excellent teaching in quantum mechanics which led to my decision to seek a research topic in that field. Special thanks also to Professor Jeffery Cooper, who allowed me to take one, and sit in on three, of his mathematics courses. Those courses enabled me to understand the demanding mathematics encountered in my research. Finally, I want to thank Diane Mancuso, Administrative Assistant of the Chemical Physics program, for her kindness, her friendliness, and her professionalism, which have made my life here so much easier.

The friends I have met during these years at the University of Maryland have enriched my life, or, as we say in Chinese, have decorated my sky. Mumtaz Qazilbash and I became good friends after working through all the assignments in quantum mechanics. We prepared for the qualifying exam and passed it together. I was always

impressed by his insistence on having dinner after finishing the homework, no matter how late the hour. Sule Atahan and Qian Wang are my two lovely officemates and dear colleagues. We shared our food, our knowledge and some secrets during long lunches. Without these discussions, I wouldn't have been able to understand some difficult concepts of a three-atom world, even though, most of the time, two of them were hydrogen. My housemates also played an important role in my study here. We discussed our research, consulted each other, and most importantly, enjoyed several hobbies together. They are Yi-Min Huang, Yng-Gwei Chen, Yen-Hui Lu, Yi-Cheng Chen, Ming-Jung Chou, Chian-En Chang, Lewis Chen and Rendy Cheng. My good friends Helene Tara and her family members reformatted my resume, increasing my chances for future research opportunities. My yoga teacher, Dada Vishrupananda, helped me to understand myself better through various meditation techniques. I become more focused on one single task. This helps me to cope with the anxiety and great pressure which accompany the writing of a dissertation. My personal editor, Nina Liakos, is responsible for any grammatical error you find here. She also helped me pass the MEI English test and served as my encyclopedia of American culture.

In my culture, we usually do not thank our family, because naturally they are always there for us. My parents, brother, and sister share the same joys of my graduation. Finally, I must mention my wife and dearest friend, Chiu-Yi Wang. I am so proud of her every accomplishment. While I have been engaged in my studies and research in the United States for six years, she has remained behind in Taiwan, single-handedly raising our two beautiful young children, Tai-Men and Kuan-Yu, while holding down a full-time job as a special educator in an elementary school. Without her my life would have no meaning.

Last but not least, I want to thank all my advisory committee for spending their precious time reading my dissertation and leaving valuable comments to improve its quality.

Table of Contents

Dedication.....	ii
Acknowledgements.....	iii
Table of Contents.....	vi
List of Tables.....	viii
List of Figures.....	ix
1 Introduction.....	1
2 Theoretical Method.....	6
2.1 Time-independent Reactive Scattering Method.....	6
2.1.1 The Hamiltonian Operator, \hat{H}	6
2.1.2 Coordinate Transformations.....	7
2.1.3 The Potential Energy Surface (PES).....	19
2.1.4 Solving the Schrödinger Equation.....	21
2.2 Experimental Observables.....	28
2.2.1 Differential and Integral Cross Sections.....	28
2.2.2 Laboratory Angular Distribution and Newton Diagram.....	30
3 The F+H ₂ → HF+H Reaction.....	35
3.1 Introduction.....	35
3.2 Potential Energy Surfaces.....	37
3.3 Reactive Scattering Calculations.....	38
3.3.1 Reactive Scattering Matrix Elements and Differential Cross Sections.....	38
3.3.2 Laboratory Angular Distributions.....	39
3.3.3 Scattering Calculations and Initial State Populations.....	40
3.4 Results and Discussion.....	42
3.4.1 Center-of-Mass Differential Cross Sections.....	42
3.4.2 DCS ratios.....	46
3.4.3 Laboratory Angular Distributions.....	51
3.5 Conclusions.....	57
4 The F+HD Reaction: Product Excitation Functions.....	59
4.1 Introduction.....	59
4.2 Method.....	62
4.2.1 Details of the scattering calculations.....	62
4.2.2 Comparison with experimental data.....	64
4.2.3 Comparison with calculations on SW PES.....	66
4.3 Results and Discussions.....	66
4.3.1 F+HD → DF+H.....	67
4.3.2 F+HD→HF+D.....	71

4.3.3	Justification for the shift of collision energies in ASW calculations ..	75
4.4	Conclusions ..	77
5	The F+HD Reaction: The Reactivity of F* ..	79
5.1	Introduction ..	79
5.2	Method ..	83
5.2.1	Details of the scattering calculations ..	83
5.2.2	Comparison with experiment ..	84
5.3	Results: Product Translational Energy Distributions ..	88
5.3.1	F+HD→DF+H ..	88
5.3.2	F+HD → HF+D ..	91
5.3.3	Statistical weighting of the ground and the spin-orbit excited states ..	96
5.4	Results: Product Rotational Distributions ..	98
5.5	Discussion And Conclusion ..	99
6	Summary ..	102
	Bibliography ..	106

List of Tables

Table 3.1 Summary of parameters for the F+H ₂ calculations	40
Table 3.2 Population of the H ₂ rotational levels in the 1985 MBE experiment	41
Table 4.1 Summary of parameters for the F+HD calculations	63
Table 4.2 Range of collision energies included in the F+HD calculations	64
Table 5.1 Heats of formation $\Delta_f H^0_{gas}$ for F+HD reactions	87

List of Figures

Fig. 2.1. Laboratory and nuclear center of mass (CM) coordinates	9
Fig. 2.2. The Jacobi coordinates for the F+H ₂ reaction	12
Fig. 2.3. Vector diagram of the total angular momentum \vec{J}	18
Fig. 2.4. Schematic drawing of the PESs for the reaction of F+H ₂ →HF+H	26
Fig. 2.5. Laboratory angular distributions, DCS and the Newton diagram	29
Fig. 3.1. Center-of-mass differential reactive cross sections (SW PES)	42
Fig. 3.2. Center-of-mass differential reactive cross sections (HSW PES)	43
Fig. 3.3. Center-of-mass differential reactive cross sections (ASW PES)	44
Fig. 3.4. Ratios of SW and HSW center-of-mass DCSs	46
Fig. 3.5. Ratios of HSW and ASW center-of-mass	47
Fig. 3.6. Ratios of ASW F*(² P _{1/2}) and F(² P _{3/2}) DCSs	49
Fig. 3.7. Comparison of SW and experimental LAB ADs	52
Fig. 3.8. Comparison of HSW and experimental LAB ADs	53
Fig. 3.9. Comparison of ASW and experimental LAB ADs	54
Fig. 3.10. Comparison of ASW and experimental LAB ADs (0% F*)	56
Fig. 4.1. Excitation function of the F+HD→HF+D reaction (SW)	60
Fig. 4.2. Excitation function of the F+HD→DF+H reaction (ASW)	68
Fig. 4.3. Vib-branching excitation functions of the DF and HF products (ASW)	70
Fig. 4.4. Excitation function of the F+HD→HF+D reaction (ASW)	72
Fig. 4.5. Comparison of the HSW and SW reaction probability	75
Fig. 5.1 Relative energies (to scale) for the F+HD→HF+D, DF+H reaction	80
Fig. 5.2. Energy level diagram (to scale) of the HF and DF product	83
Fig. 5.3. Product translational energy distributions for the DF channel	89
Fig. 5.4. Product translational energy distributions for the HF channel	92

Fig. 5.5. HF($\nu=3$) rotational distributions by Nesbitt and co-workers 97

1 Introduction

In this dissertation we use a quantum mechanical (QM) time-independent scattering method to study the role of the spin-orbit excited state in the F+H₂ and its isotopic F+HD reactions. The calculations involve multiple potential energy surfaces (the Alexander-Stark-Werner, ASW, PESs),¹ and include an accurate treatment of the couplings (non-adiabatic, spin-orbit, and Coriolis) among all three electronic states.¹

The first systematic study of the F+H₂ reaction dates back to the discovery of chemical lasers in late 1960s.² Since then it has been extensively studied both experimentally and theoretically, and subsequently has become the prototype for exothermic chemical reactions.^{1,3-8}

Although the interest in the F+H₂ reaction was inspired by its application to chemical lasers, much study, since the early 1970s, has focused on searching for the existence of the dynamical resonance predicted by various early QM calculations.⁹ In 1985, Lee and co-workers used a high-resolution molecular beam experiment to determine the vibrational-state-resolved center-of-mass angular distribution (CM AD) for the F+H₂ reaction.¹⁰ For the first time, this allowed a direct comparison with theoretical calculations. The prominent forward scattering of HF in the v'=3 product level was attributed to a dynamical resonance.^{4,10,11} Throughout this dissertation we shall use the term DCS to denote the center-of-mass frame differential cross sections, and the term AD to determine the LAB frame differential cross section.

This 1985 molecular beam experiment¹⁰ has stimulated extensive theoretical interest⁴ in the F+H₂ system and led eventually to the fully *ab initio* calculation of a global potential-energy surface (PES) completed by Stark and Werner (SW) in 1996.¹² Subsequently Manolopoulos and co-workers, using a complete QM calculation,¹¹ and Aoiz and co-workers, using quasi-classical trajectories (QCT),¹³

investigated the forward scattering of HF ($v' = 3$). They demonstrated that the forward peak was due mainly to QM tunneling rather than a scattering resonance.¹¹

Although the overall agreement with experiment was a great triumph for theory, some discrepancies still exist.¹⁴ The most noticeable is the underestimation in the theoretical simulation of the intensities of products scattered in the sideways direction. Inclusion into the PES of a correction for the spin-orbit splitting in the F atom¹⁵ unfortunately increased the degree of discrepancy in the sideways scattering.¹⁶ All these calculations^{11,13,14,16} were restricted to a single Born-Oppenheimer (or adiabatic) PES. Consequently, the contribution from the reactivity of the excited spin-orbit state (F*) and the effect of non-adiabatic coupling, which are ignored in these earlier calculations, offer a possible explanation of this discrepancy in the LAB ADs.⁴

The F* ($^2P_{1/2}$) state lies 1.16 kcal/mole (404 cm^{-1}) higher than the F ($^2P_{3/2}$) ground state, while the reaction has a barrier height of (1.80 ± 0.25) kcal/mol (bent)¹² taking into account spin-orbit coupling. Since the (F* – F) energy difference is comparable to the reaction barrier, we would expect F* to be significantly more reactive than F at collision energies < 0.5 kcal/mol. This has been confirmed recently by Alexander and co-workers.¹ Unfortunately, results at this low energy range were not reported in the 1985 experiment. At higher energy, the F ground state is predicted to be more reactive than F*.¹ The population weighted total reaction probability of F* is estimated to be $< 10\%$ of that of F and is thus difficult to be seen experimentally.^{1,10}

Because of its lower statistical weight, the spin-orbit excited state does not contribute much to the overall reaction probability. Still, it can play an important role in the reaction dynamics as shown in a recent series of theoretical studies.¹⁷⁻²¹ For example, in the $\text{Cl} + \text{H}_2 \rightarrow \text{HCl} + \text{H}$ reaction, the presence of multiple PESs enhances the inelastic scattering of $\text{Cl} + \text{H}_2(j=0) \rightarrow \text{Cl} + \text{H}_2(j'=1,2)$, and therefore reduces the

probability of reaction.^{17,18} In the $F+HD\rightarrow HF+D$ reaction, the integral cross section of the F ground state shows a strong resonance feature at low collision energies,²² but that of F^* does not.²⁰ As a result, the resonance feature in the combined cross section (summed over F and F^*) depends sensitively on the amount of F^* presented in the beam.²⁰ For the $F+H_2\rightarrow HF+H$ reaction, the higher internal energy of F^* gives rise to additional translation energy in the products for a given initial translational energy and thus results in a wider spreading of the final product states. Additionally, because the F^*+H_2 asymptote correlates with the an highly excited electronic state of HF,¹ reactions of the F^* must involve a non-adiabatic transition to a lower, reactive PES. Accordingly, we would expect the resulting product AD to be different from that for reaction of atoms in the ground spin-orbit state. This may give rise to enhanced sideways scattering.

It is due to the open-shell character of the F atom that a detailed investigation of the F^* reactivity is needed in order to understand better the role of the F spin-orbit excited state in the $F+H_2$ and $F+HD$ reactions. The rest of this dissertation is organized as follows: Chapter 2 presents an overview of the time-independent reactive scattering theory. We summarize the methods used to solve the Schrödinger equation on a single adiabatic PES and multiple PESs with spin-orbit coupling. We also review in detail the transformation method used to convert the DCSs in the center-of-mass frame to the ADs in the laboratory frame. This enables us to interpret the remaining discrepancy between our calculations and the experiment presented in Chapter 3.

In Chapter 3, we present and discuss the calculated DCSs and ADs for the $F+H_2$ reaction. By clarifying and separating the contribution due to reaction of the excited spin-orbit state and the contribution due to non-adiabatic effects during the reaction of the ground spin-orbit state, we show that non-adiabatic couplings effectively reduce the backward scattering of HF products. Consequently, the three-

state calculations resulted in enhanced sideways scattering in the simulated ADs, in better agreement with experiment.¹⁰ Surprisingly, we find that the DCSs for reactions of F and F* have a very similar angular dependence. Thus we see that the presence of F* in the F beam affects mainly the overall magnitude without changing the shape of DCSs and ADs. As a result, it is the effect of non-adiabatic couplings, rather than the contribution from the reactivity of F*, that brings our calculations to better agreement with the experiment.

In Chapter 4 we present the excitation functions of the HF and DF products for the F+HD reactions. We demonstrate that the reaction of F* to yield HF does not show the resonance structure in the excitation functions (energy dependence of the integral cross sections), while the F does, as seen experimentally^{22,23} and in theoretical simulations based on the single Stark-Werner (SW) PES.²² Consequently, the greater the fraction of F* in the incident beam, the less pronounced will be this resonance structure. We also obtain an excellent agreement in the DF product channel and an improved agreement in the HF product channel with the experiment by a simple upward shift in the collision energies by 0.35 kcal/mol, an amount approximately equal to the difference between the actual and the SW barrier height.²⁴⁻²⁶ This technique, which compensates the overestimation of the calculated reaction barrier height by a simple upward shift in collision energies, can be applied to calculations of other chemical reactions, where the (*ab initio*) calculated PES usually overestimates the actual barrier height.

In Chapter 5 we compare with experiment our simulations of the HF and DF product translational energy distributions for the F+HD reaction. This complements the reactivity of the F spin-orbit excited state found in the experiments.^{22,23,27} From the excellent agreement between our calculations and the experiment of Liu and co-workers, we conclude that the population of F* in the molecular beam experiment of Liu and co-workers reaches thermal equilibrium at the experimental temperature

600K.^{22,23} Therefore, for the first time in both theory and experiment, we confirm that the fraction ratio of F*:F equals 0.16:0.84 in the F beam. This offers the future guidance determining the fractional population of F* in the F beam for simulations of similar molecular beam experiments.

The last Chapter summarizes the role of the F spin-orbit excited state in the F+H₂ and F+HD reactions studied in this dissertation. The most significant effect associated with the F* is the consequence of non-adiabatic couplings, which alters the reaction dynamics of the F spin-orbit ground state in the F+H₂ reaction. Overall, the reactivity of F spin-orbit excited state, after taking account the 16% fraction population of F*, is very small comparing to that of the F spin-orbit ground state. Consequently, the discrepancies between the experiments^{22,23} and the calculations on the lowest adiabatically electronically state,²² on the intensity of HF product excitation functions (energy dependence of integral cross sections) of the F+HD reactions, are not artifacts of an improper treatment of nonadiabaticity in this reaction. Given the fact that there remain residual inaccuracies in the SW PES,²⁴⁻²⁶ we consequently encourage further refinement of global F+H₂ PES. We also suggest future DCS calculations of F+HD → HF(v'=3)+D reaction to explore the F* reactivity in the collision energy range between 1.3 to 2.0 kcal/mol, where we expect the F* to make significant contributions for scattering in the forward direction.

2 Theoretical Method

2.1 Time-independent Reactive Scattering Method

There are several methods which can be used to investigate reactive scattering: time-independent quantum scattering, time-dependent quantum wave packets, or QCT.²⁸ In this Chapter, we will focus on the time-independent quantum scattering method. The goal is to calculate the state-to-state scattering matrix by solving the time-independent Schrödinger equation,

$$\hat{H}\Psi = E\Psi, \quad (2.1)$$

where E is the total energy of the system.

2.1.1 The Hamiltonian Operator, \hat{H}

The total Hamiltonian operator for a triatomic system is

$$\hat{H}_{tot} = \hat{T}_n + \hat{T}_e + \hat{V}_{nn} + \hat{V}_{ee} + \hat{V}_{ne} + \hat{H}_{so} \quad (2.2)$$

where n refers to the nuclei (F, H and H) and e refers to the electrons; \hat{T}_n is the kinetic energy operator of the nuclei; \hat{T}_e is the kinetic energy operator of the electrons; \hat{V}_{nn} is the nuclear repulsion; \hat{V}_{ee} is the electronic repulsion; \hat{V}_{ne} is the nuclear-electronic attraction; and \hat{H}_{so} is the spin-orbit interaction.

Usually, \hat{H}_{so} is added on once the electronic wavefunctions have been determined. Exclusive of this term, the Hamiltonian is, in atomic units,²⁹

$$\begin{aligned} \hat{H} &= \hat{T}_n + \hat{T}_e + \hat{V}_{nn} + \hat{V}_{ee} + \hat{V}_{ne} \\ &= \sum_{n_i} -\frac{\bar{\nabla}_{n_i}^2}{2m_{n_i}} + \sum_e -\frac{\bar{\nabla}_e^2}{2m_e} + \sum_{n_i} \sum_{n_j (n_i < n_j)} \frac{Z_{n_i} Z_{n_j}}{|\vec{r}_{n_i} - \vec{r}_{n_j}|} \\ &\quad + \sum_e \sum_{e' (e' < e)} \frac{1}{|\vec{r}_e - \vec{r}_{e'}|} - \sum_{n_i} \sum_e \frac{Z_{n_i}}{|\vec{r}_{n_i} - \vec{r}_e|} \end{aligned} \quad (2.3)$$

where

$$G_x = G_y = G_z = \begin{pmatrix} m_1 & & 0 \\ & m_2 & \\ 0 & & \ddots \end{pmatrix}, \dot{r}_{ix} \rightarrow \frac{dr_{ix}}{dt}, \dot{r}_{iy} \rightarrow \frac{dr_{iy}}{dt} \text{ and } \dot{r}_{iz} \rightarrow \frac{dr_{iz}}{dt} \quad (2.7)$$

with m_1 and $m_2 \dots$ referring to the mass of particle 1 and 2 ... (nuclei and electrons) of the system and $\dot{\vec{r}} = (\dot{r}_{1x}, \dot{r}_{2x}, \dots, \dot{r}_{1y}, \dot{r}_{2y}, \dots, \dot{r}_{1z}, \dot{r}_{2z}, \dots)$.

Because that the G matrix is block diagonal in each of the x, y and z coordinates and $G_x = G_y = G_z$, we will illustrate explicitly only transformations of the x coordinate. The transformations of the y and z coordinates will be identical.

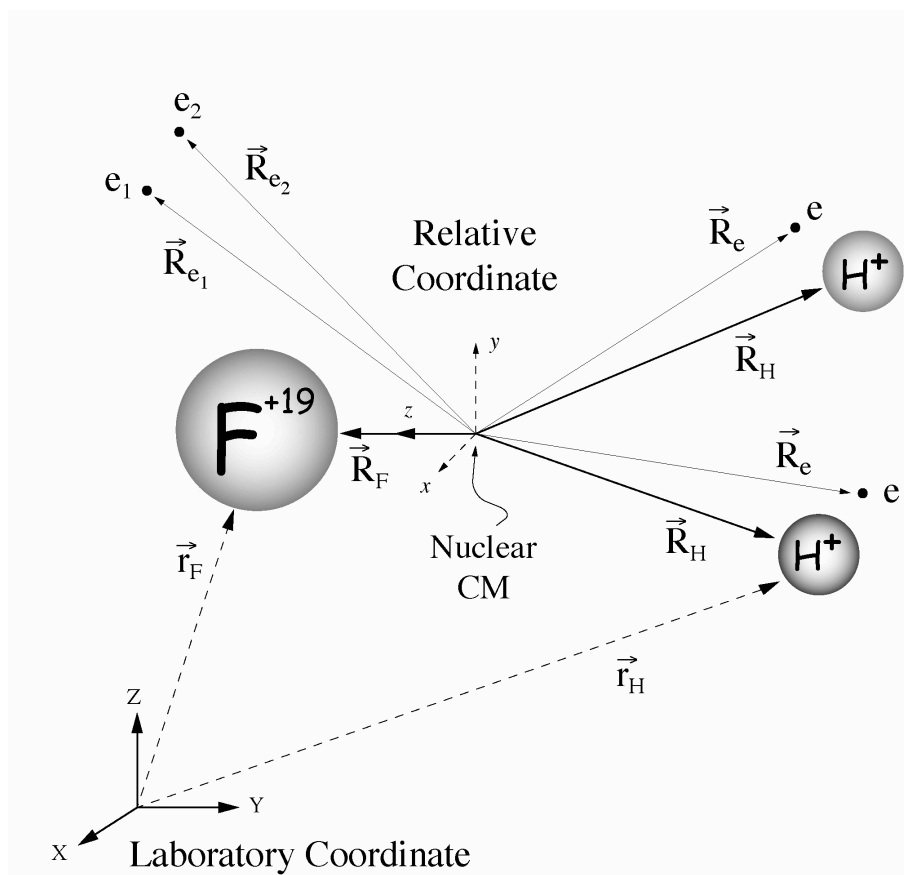


Figure 2.1 Laboratory and nuclear center of mass (CM) coordinates for the triatomic system of $F+H_2$. The vectors \vec{r} and \vec{R} are the position vectors in the laboratory (XYZ) and CM (xyz) coordinates respectively, with the subscripts F, H and e indicating the F and H nuclei and electrons.

Relative Coordinates in the Nuclear Center of Mass Frame

The first step is to separate the translational motion of the center of mass (CM) of the system using the relative (or internal) coordinates with origin at the nuclear CM as shown in Fig. 2.1. The relative coordinates \vec{R} and the space fixed coordinates \vec{r} are related by the transformation matrix, L'_x ,

$$\begin{aligned}
\bar{R}^r = \begin{pmatrix} R_{cm}^r \\ R_{n_2}^r \\ R_{n_3}^r \\ R_{e_1}^r \\ R_{e_2}^r \\ \vdots \end{pmatrix}_x &= \underbrace{\begin{pmatrix} \frac{m_{n_1}}{M_{tot}} & \frac{m_{n_2}}{M_{tot}} & \frac{m_{n_3}}{M_{tot}} & \frac{m_e}{M_{tot}} & \frac{m_e}{M_{tot}} & \cdots \\ -\frac{m_{n_1}}{M_{nuc}} & 1-\frac{m_{n_2}}{M_{nuc}} & -\frac{m_{n_3}}{M_{nuc}} & 0 & 0 & \cdots \\ -\frac{m_{n_1}}{M_{nuc}} & -\frac{m_{n_2}}{M_{nuc}} & 1-\frac{m_{n_3}}{M_{nuc}} & 0 & 0 & \cdots \\ \hline -\frac{m_{n_1}}{M_{nuc}} & -\frac{m_{n_2}}{M_{nuc}} & -\frac{m_{n_3}}{M_{nuc}} & m_e & \mathbf{0} & \\ -\frac{m_{n_1}}{M_{nuc}} & -\frac{m_{n_2}}{M_{nuc}} & -\frac{m_{n_3}}{M_{nuc}} & \mathbf{0} & m_e & \\ \vdots & \vdots & \vdots & \mathbf{0} & & \ddots \end{pmatrix}}_{L_x^r} \begin{pmatrix} r_{n_1} \\ r_{n_2} \\ r_{n_3} \\ r_{e_1} \\ r_{e_2} \\ \vdots \end{pmatrix}_x, \tag{2.8}
\end{aligned}$$

where $M_{tot} = \sum_{n_i,e} m_{n_i,e}$ and $M_{nuc} = \sum_{n_i} m_{n_i}$.

Using Eq. (2.8), we transform the nuclear and electronic energies $[T_n(\vec{r})_x, T_e(\vec{r})_x]$ in space fixed coordinates to nuclear CM, nuclear and electronic energies $[T_{cm}^r(\bar{R}_{cm}^r)_x, T_n^r(\bar{R}_n^r)_x, T_e^r(\bar{R}_e^r)_x]$ in the relative coordinates,

$$\begin{aligned}
T_n(\vec{r})_x + T_e(\vec{r})_x &= \left(\dot{\vec{r}}_x\right)^T \cdot G_x \cdot \dot{\vec{r}}_x \quad \xrightarrow{\text{relative coordinate}} \Rightarrow \\
T_{cm}^r(\bar{R}_{cm}^r)_x + T_n^r(\bar{R}_n^r)_x + T_e^r(\bar{R}_e^r)_x &= \left(\dot{\bar{R}}_x^r\right)^T \cdot G_x^r \cdot \dot{\bar{R}}_x^r, \tag{2.9}
\end{aligned}$$

where

$$G_x^r = \left(L_x^{r-1} \right)^T \cdot G_x \cdot L_x^{r-1}$$

$$= \left(\begin{array}{c|c|c} \boxed{M_{tot}} & & \mathbf{0} \\ \hline \underbrace{\phantom{\boxed{M_{tot}}}}_{G_{cm}^r} & \underbrace{\begin{array}{|c|c|} \hline \frac{m_{n_2}(m_{n_1}+m_{n_2})}{m_{n_1}} & \frac{m_{n_2}m_{n_3}}{m_{n_1}} \\ \hline \frac{m_{n_2}m_{n_3}}{m_{n_1}} & \frac{m_{n_3}(m_{n_1}+m_{n_3})}{m_{n_1}} \\ \hline \end{array}}_{G_n^r} & \\ \hline \mathbf{0} & m_e \times \underbrace{\begin{array}{|c|c|} \hline 1 - \frac{m_e}{M_{tot}} & -\frac{m_e}{M_{tot}} \\ \hline -\frac{m_e}{M_{tot}} & 1 - \frac{m_e}{M_{tot}} \\ \hline & \ddots \\ \hline \end{array}}_{G_e^r} & \end{array} \right) \quad (2.10)$$

and

$$\hat{V}_{nn}(\vec{r}_n), \hat{V}_{ee}(\vec{r}_e), \hat{V}_{ne}(\vec{r}_n, \vec{r}_e) \quad \xRightarrow{\text{relative coordinate}} \quad \hat{V}_{nn}^r(\vec{R}_n^r), \hat{V}_{ee}^r(\vec{R}_e^r), \hat{V}_{ne}^r(\vec{R}_n^r, \vec{R}_e^r). \quad (2.11)$$

As illustrated in Eq. (2.10), the G_x^r matrix is blocked into 1×1 , 2×2 , and $N_e \times N_e$ ($N_e =$ number of electrons) matrices which we designate as G_{cm}^r , G_n^r and G_e^r respectively. Subsequently the coordinates of $T_{cm}^r(\vec{R}_{cm}^r)_x$, $T_n^r(\vec{R}_n^r)_x$ and $T_e^r(\vec{R}_e^r)_x$ are separated. The price we pay for this separation is that G_n^r and G_e^r both contain off-diagonal terms [Eq. (2.10)]. The G_e^r matrix is diagonal if we ignore, comparing to 1, the small contribution of $m_e/M_{tot} \approx 1/40000$ (for F+H₂).^{30,31}

For reasons that will become clear in the section below on the Born-Oppenheimer approximation^{30,31}, we group the $\hat{T}_e^r(\vec{R}_e^r)$, \hat{V}_{nn} , \hat{V}_{ee} , and \hat{V}_{ne} terms together to form the electronic Hamiltonian $\hat{H}_e^r(\vec{R}_n^r; \vec{R}_e^r)$:

$$\hat{H}_e^r(\vec{R}_n^r; \vec{R}_e^r) = \hat{T}_e^r(\vec{R}_e^r) + \hat{V}_{nn}^r(\vec{R}_n^r) + \hat{V}_{ee}^r(\vec{R}_e^r) + \hat{V}_{ne}^r(\vec{R}_n^r, \vec{R}_e^r). \quad (2.12)$$

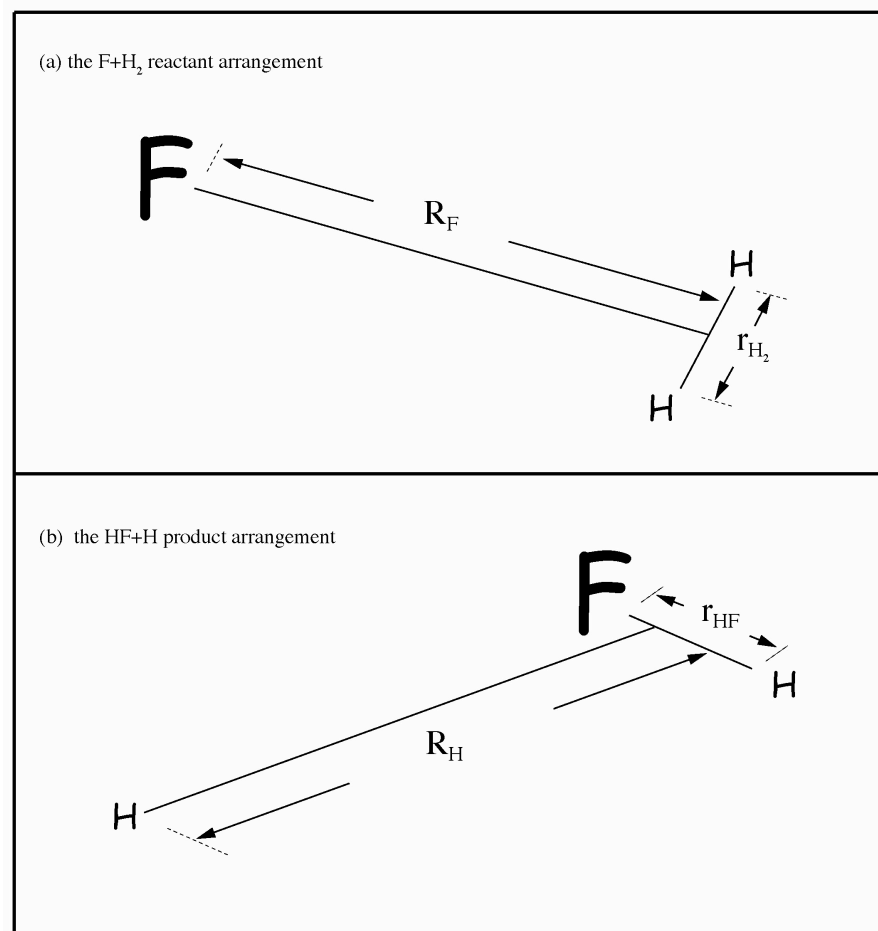


Figure 2.2 The Jacobi coordinates in the (a) $F+H_2$ reactant arrangement and (b) the $HF+H$ product arrangement.

Jacobi and Mass Weighted Jacobi Coordinates

The nuclear kinetic energies $T_n^r(\vec{R}_e^r)$ can be simplified using the Jacobi coordinates as shown in Fig. 2.2(a). The Jacobi coordinates³² $(\vec{R}_{n_1}^j, \vec{r}_{n_{23}}^j)$ and the relative coordinates $(\vec{R}_{n_2}^r, \vec{R}_{n_3}^r)$ are related by the transformation matrix L_x^j ,

$$\begin{pmatrix} R_{n_1}^j \\ r_{n_{23}}^j \end{pmatrix}_x = \underbrace{\begin{pmatrix} -m_{n_2}\mu^j & -m_{n_3}\mu^j \\ 1 & -1 \end{pmatrix}}_{L_x^j} \begin{pmatrix} R_{n_2}^r \\ R_{n_3}^r \end{pmatrix}_x \text{ with } \mu^j = \frac{M_{nuc}}{m_{n_1}(m_{n_2} + m_{n_3})}, \quad (2.13)$$

Using Eq. (2.13), we transform the nuclear kinetic energy and the electronic Hamiltonian $[T_n^r(\vec{R}_n^r)_x, \hat{H}_e^r(\vec{R}_n^r; \vec{R}_e^r)]$ in relative coordinates to $[T_n^j(\vec{R}_n^j)_x, \hat{H}_e^j(\vec{R}_{n_1}^j, \vec{r}_{n_{23}}^j; \vec{R}_e^j)]$ in Jacobi coordinates,

$$T_n^r(\vec{R}_n^r)_x = \left(\dot{\vec{R}}_x^r\right)^T \cdot G_x^r \cdot \dot{\vec{R}}_x^r \xRightarrow{\text{Jacobi coordinate}} T_n^j(\vec{R}_n^j)_x = \left(\dot{\vec{R}}_x^j\right)^T \cdot G_x^j \cdot \dot{\vec{R}}_x^j, \quad (2.14)$$

where

$$G_x^j = \left(L_x^{j-1}\right)^T \cdot G_x^r \cdot L_x^{j-1} = \begin{pmatrix} \frac{m_{n_1}(m_{n_2} + m_{n_3})}{M_{nuc}} & 0 \\ 0 & \frac{m_{n_2}m_{n_3}}{m_{n_2} + m_{n_3}} \end{pmatrix}, \quad (2.15)$$

and

$$\hat{H}_e^r(\vec{R}_n^r; \vec{R}_e^r) \xRightarrow{\text{Jacobi coordinate}} \hat{H}_e^j(\vec{R}_{n_1}^j, \vec{r}_{n_{23}}^j; \vec{R}_e^j). \quad (2.16)$$

We further use mass-weighted Jacobi coordinates³² $(\vec{R}_{n_1}^{mj}, \vec{r}_{n_{23}}^{mj})$ which are defined by

$$\begin{pmatrix} R_{n_1}^{mj} \\ r_{n_{23}}^{mj} \end{pmatrix}_x = \underbrace{\begin{pmatrix} s^{1/2} & 0 \\ 0 & s^{-1/2} \end{pmatrix}}_{L_x^{mj}} \begin{pmatrix} R_{n_1}^j \\ r_{n_{23}}^j \end{pmatrix}_x \text{ with } s = \frac{m_{n_1}}{\mu} \left(1 - \frac{m_{n_1}}{M_{nuc}}\right) \text{ and } \mu = \left(\frac{m_{n_1}m_{n_2}m_{n_3}}{M_{nuc}}\right)^{1/2}, \quad (2.17)$$

to simplify the G_x^j matrix in Eq. (2.15). The $[T_n^r(\vec{R}_n^r)_x, \hat{H}_e^j(\vec{R}_{n_1}^j, \vec{r}_{n_{23}}^j; \vec{R}_e^j)]$ in Jacobi coordinates and $[T_n^{mj}(\vec{R}_{n_1}^{mj}, \vec{r}_{n_{23}}^{mj})_x, \hat{H}_e^{mj}(\vec{R}_{n_1}^{mj}, \vec{r}_{n_{23}}^{mj}; \vec{R}_e^{mj})]$ in mass-weighted Jacobi coordinates are related by the transformations,

$$T_n^j(\vec{R}_{n_1}^j, \vec{r}_{n_{23}}^j)_x = \left(\dot{\vec{R}}_x^j\right)^T \cdot G_x^j \cdot \dot{\vec{R}}_x^j \stackrel{\text{mass-weighted Jacob coordinate}}{\Rightarrow} T_n^{mj}(\vec{R}_{n_1}^{mj}, \vec{r}_{n_{23}}^{mj})_x = \left(\dot{\vec{R}}_x^{mj}\right)^T \cdot G_x^{mj} \cdot \dot{\vec{R}}_x^{mj}, \quad (2.18)$$

where

$$G_x^{mj} = \left(L_x^{mj-1}\right)^T \cdot G_x^j \cdot L_x^{mj-1} = \begin{pmatrix} \mu & 0 \\ 0 & \mu \end{pmatrix}, \quad (2.19)$$

and

$$\hat{H}_e^j(\vec{R}_{n_1}^j, \vec{r}_{n_{23}}^j; \vec{R}_e^j) \stackrel{\text{mass-weighted Jacob coordinate}}{\Rightarrow} \hat{H}_e^{mj}(\vec{R}_{n_1}^{mj}, \vec{r}_{n_{23}}^{mj}; \vec{R}_e^{mj}). \quad (2.20)$$

Explicitly, the kinetic energy T_n^{mj} becomes,

$$T_n^{mj} = \frac{\mu}{2} \left[\left(\dot{\vec{R}}^{mj}\right)^2 + \left(\dot{\vec{r}}^{mj}\right)^2 \right] = \frac{1}{2\mu} \left(\vec{P}_{\vec{R}^{mj}}^2 + \vec{P}_{\vec{r}^{mj}}^2 \right). \quad (2.21)$$

where $\vec{P}_{\vec{R}^{mj}} = \mu \dot{\vec{R}}^{mj}$ and $\vec{P}_{\vec{r}^{mj}} = \mu \dot{\vec{r}}^{mj}$ are the momenta in the \vec{R} and \vec{r} coordinates.

At this point we switch back to a quantum description by the operator substitution $P \rightarrow -i\nabla$ in Eq. (2.21). Thus, in mass-weighted Jacobi coordinates, the kinetic energy operator \hat{T}_n^{mj} is

$$\hat{T}_n^{mj} = -\frac{1}{2\mu} \left(\nabla_{\vec{R}^{mj}}^2 + \nabla_{\vec{r}^{mj}}^2 \right), \quad (2.22)$$

and the Schrödinger equation becomes,

$$\left[-\frac{1}{2\mu} \left(\nabla_{\vec{R}^{mj}}^2 + \nabla_{\vec{r}^{mj}}^2 \right) + \hat{H}_e^{mj}(\vec{R}^{mj}, \vec{r}^{mj}; \vec{R}_e^{mj}) \right] \Psi = E\Psi. \quad (2.23)$$

So far, we have explicitly labeled each coordinate with superscripts to keep track of the coordinate transformations. Hereafter, we will always refer (\vec{R} , \vec{r} and \vec{R}_e) to the mass-weighted Jacobi coordinates (\vec{R}^{mj} , \vec{r}^{mj} and \vec{R}_e^{mj}), thus no longer label those superscripts. We will reassign them only if necessary.

Delves Hyperspherical Coordinates

Considering both the reactant and product coordinates (Fig. 2.2) and using Eq. (2.23), the Schrödinger equation for the F+H₂ reaction becomes,

$$\text{Reactants: } \left[-\frac{1}{2\mu} \left(\nabla_{\vec{R}_F}^2 + \nabla_{\vec{r}_{H_2}}^2 \right) + \hat{H}_e(\vec{R}_F, \vec{r}_{H_2}; \vec{R}_e) \right] \Psi_{F+H_2} = E \Psi_{F+H_2}, \quad (2.24)$$

$$\text{Products: } \left[-\frac{1}{2\mu} \left(\nabla_{\vec{R}_H}^2 + \nabla_{\vec{r}_{HF}}^2 \right) + \hat{H}_e(\vec{R}_H, \vec{r}_{HF}; \vec{R}_e) \right] \Psi_{H+HF} = E \Psi_{H+HF}. \quad (2.25)$$

As illustrated in Fig. 2.2, the coordinates best describing the approach of the reactants in Eq. (2.24) are very different from the coordinates best describing the recoil of the products in Eq. (2.25). This leads to various complications in QM reactive scattering calculations.³³ In order to avoid these difficulties, we look for a new coordinate system that is independent of the reaction coordinates.

Following Smith's work,³⁴ we first attempt to find the transformation matrix between the reactant and product coordinates. The requirements that both coordinates transform inversely back to the same relative coordinate \vec{R}_n^r in Eq. (2.8) leads to the relation,

$$\left(\vec{R}_n^r \right)_x = \left(L_x^j \right)_{\text{reac}}^{-1} \cdot \left(L_x^{mj} \right)_{\text{reac}}^{-1} \cdot \left(\vec{R}_n^{mj} \right)_{x,\text{reac}} = \left(L_x^j \right)_{\text{prod}}^{-1} \cdot \left(L_x^{mj} \right)_{\text{prod}}^{-1} \cdot \left(\vec{R}_n^{mj} \right)_{x,\text{prod}}. \quad (2.26)$$

Thus the reactant and product mass-weighted Jacobi coordinates, $\left(\vec{R}_n^{mj} \right)_{x,\text{reac}}$ and $\left(\vec{R}_n^{mj} \right)_{x,\text{prod}}$, are related by the matrix L_x^{rp} ,

$$\left(\vec{R}_n^{mj} \right)_{x,\text{reac}} = L_x^{rp} \cdot \left(\vec{R}_n^{mj} \right)_{x,\text{prod}}, \quad (2.27)$$

where

$$\begin{aligned}
L_x^{rp} &= \left(L_x^{mj}\right)_{reac} \cdot \left(L_x^j\right)_{reac} \cdot \left(L_x^j\right)_{prod}^{-1} \cdot \left(L_x^{mj}\right)_{prod}^{-1} \\
&= \begin{pmatrix} -\frac{m_{n_1}^{1/2} m_{n_3}^{1/2}}{(m_{n_1} + m_{n_2})^{1/2} (m_{n_2} + m_{n_3})^{1/2}} & \frac{m_{n_2}^{1/2} (m_{n_1} + m_{n_2} + m_{n_3})^{1/2}}{(m_{n_1} + m_{n_2})^{1/2} (m_{n_2} + m_{n_3})^{1/2}} \\ \frac{m_{n_2}^{1/2} (m_{n_1} + m_{n_2} + m_{n_3})^{1/2}}{(m_{n_1} + m_{n_2})^{1/2} (m_{n_2} + m_{n_3})^{1/2}} & -\frac{m_{n_1}^{1/2} m_{n_3}^{1/2}}{(m_{n_1} + m_{n_2})^{1/2} (m_{n_2} + m_{n_3})^{1/2}} \end{pmatrix} \\
&= \begin{pmatrix} \cos\Theta & -\sin\Theta \\ \sin\Theta & \cos\Theta \end{pmatrix}
\end{aligned} \tag{2.28}$$

Here we have defined a skewing angle, Θ :^{35,36}

$$\Theta = \tan^{-1}\left(\frac{m_{n_2}}{\mu}\right), \tag{2.29}$$

with μ defined in Eq. (2.17).

Explicitly, the mass-weighted reactant and product Jacobi coordinates are related by an orthogonal transformation,

$$\begin{pmatrix} R \\ r \end{pmatrix}_{x, reac} = \begin{pmatrix} \cos\Theta & \sin\Theta \\ -\sin\Theta & \cos\Theta \end{pmatrix} \begin{pmatrix} R \\ r \end{pmatrix}_{x, prod}. \tag{2.30}$$

Subsequently, Delves define the hyperspherical coordinates:^{32,37}

$$\text{Hyperradius, } \rho: \quad \rho = \left(\bar{R}^2 + \bar{r}^2\right)^{1/2}, \tag{2.31}$$

$$\text{Hyperangle, } \theta_\alpha: \quad \theta_\alpha = \tan^{-1}\left(\frac{R}{r}\right)_\alpha, \tag{2.32}$$

with α indicating the nuclear arrangement of reactants or products. Note that the hyperradius, ρ , is independent of the reactant or product coordinates as a result of the orthogonal transformation of Eq. (2.30). This is the separation coordinate we shall utilize in the QM treatment of reactive scattering.

With Eq. (2.31) and (2.32) and using the chain rule, the nuclear kinetic energy operator \hat{T}_n in Eq. (2.22) becomes,³⁶

$$\hat{T}_n = -\frac{1}{2\mu\rho^5} \frac{\partial}{\partial\rho} \rho^5 \frac{\partial}{\partial\rho} + \frac{\Delta^2}{2\mu\rho^2}, \quad (2.33)$$

where the Δ^2 is the square of Smith's grand angular momentum operator,³⁴

$$\Delta^2 = -\frac{1}{\sin^2 2\theta_\alpha} \frac{\partial}{\partial\theta_\alpha} \sin^2 2\theta_\alpha \frac{\partial}{\partial\theta_\alpha} + \frac{\hat{j}^2}{\sin^2 \theta_\alpha} + \frac{\hat{L}^2}{\cos^2 \theta_\alpha}. \quad (2.34)$$

As shown in Fig. 2.3(a), \hat{j} is the rotational angular momentum operator of the diatomic fragment and \hat{L} is the orbital angular momentum operator of the atom around the CM of the diatomic molecule.

Note that the hyperspherical coordinates still depend on the nuclear arrangement through the hyperangle θ_α . This arrangement dependence can be removed by expanding the wavefunction in sets of orthonormal functions $\Phi(\theta_\alpha)$ (see section 2.1.4). The hyperspherical coordinates, ρ and θ_α together with the other four coordinates of $\hat{R}_\theta, \hat{R}_\phi$ in $\hat{L}(\hat{R}_\theta, \hat{R}_\phi)$ and $\hat{r}_\theta, \hat{r}_\phi$ in $\hat{j}(\hat{r}_\theta, \hat{r}_\phi)$ span the 6 mass-weighted Jacobi coordinates \vec{R} and \vec{r} .

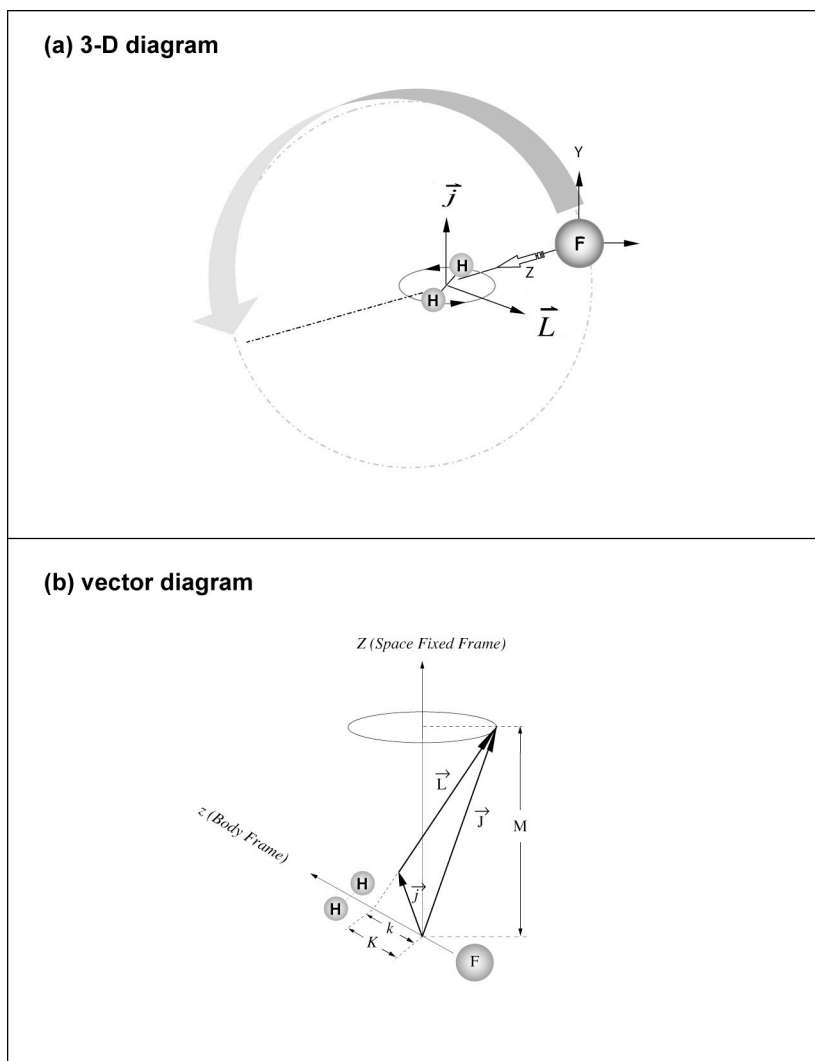


Figure 2.3 (a) Schematic drawing showing the rotational angular momentum \vec{j} of the diatomic molecule H_2 and the orbital angular momentum \vec{L} of the F atom around the center-of-mass of H_2 . (b) Vector diagram showing the addition of \vec{j} and \vec{L} to form the total angular momentum \vec{J} with projections M along the space (laboratory) frame Z axis and K along the body frame z axis.

2.1.3 The Potential Energy Surface (PES)

In this section, we review the concept of the PES derived from the Born-Oppenheimer approximation^{30,38} as well as several important definitions, including adiabatic^{30,39} and diabatic³⁹ PESs and non-adiabatic coupling^{30,39}.

Born-Oppenheimer and Adiabatic Approximation

Based on the observation that electrons move much faster than the massive nuclei in the molecule, the Born-Oppenheimer approximation seeks to determine electronic wavefunctions that adjust themselves instantaneously to each nuclear geometry, or in other words, to determine electronic wavefunctions which are independent of the nuclear motion. This separates the electronic Hamiltonian $\hat{H}_e(\vec{R}, \vec{r}; \vec{R}_e)$ from the nuclear kinetic energy operator T_n in Eq. (2.23) leading to a major simplification. Born and Oppenheimer recognized that the electronic Hamiltonian $\hat{H}_e(\vec{R}, \vec{r}; \vec{R}_e)$ in Eq. (2.20) (or Eq. 2.12) depends only on the position of nuclei, not on their momenta. We first solve the electronic Schrödinger equation at fixed nuclear positions (\vec{R}, \vec{r}) ,

$$\hat{H}_e \phi_i(\vec{R}, \vec{r}; \vec{R}_e) = \varepsilon_i \phi_i(\vec{R}, \vec{r}; \vec{R}_e). \quad (2.35)$$

Without any approximation, the total wave function Ψ can then be expanded in this complete set of orthonormal electronic wave functions $\phi_i(\vec{R}, \vec{r}; \vec{R}_e)$, with expansion coefficients $\psi_i(\vec{R}, \vec{r})$ which depend only on the nuclear coordinates (\vec{R}, \vec{r}) ,

$$\Psi(\vec{R}, \vec{r}, \vec{R}_e) = \sum_i \psi_i(\vec{R}, \vec{r}) \phi_i(\vec{R}, \vec{r}; \vec{R}_e). \quad (2.36)$$

Using Eq. (2.35) and (2.36), and expanding Eq. (2.23), we find,

$$\begin{aligned} \sum_i \left[\nabla_{\vec{R}}^2 \psi_i(\vec{R}, \vec{r}) \right] \phi_i(\vec{R}, \vec{r}; \vec{R}_e) + \varepsilon_i(\vec{R}, \vec{r}) \psi_i(\vec{R}, \vec{r}) \phi_i(\vec{R}, \vec{r}; \vec{R}_e) + \sum_i \psi_i(\vec{R}, \vec{r}) \nabla_{\vec{R}}^2 \phi_i(\vec{R}, \vec{r}; \vec{R}_e) \\ + \sum_i 2 \left[\nabla_{\vec{R}} \psi_i(\vec{R}, \vec{r}) \right] \left[\nabla_{\vec{R}} \phi_i(\vec{R}, \vec{r}; \vec{R}_e) \right] = E \left[\sum_i \psi_i(\vec{R}, \vec{r}) \phi_i(\vec{R}, \vec{r}; \vec{R}_e) \right]. \end{aligned} \quad (2.37)$$

Multiplying both sides by $\phi_j(\vec{R}, \vec{r}; \vec{R}_e)$ and integrating over the electronic coordinate \vec{R}_e , we obtain,

$$(\hat{T}_n + \hat{V}_{BO})\psi_i(\vec{R}, \vec{r}) + \hat{U}_{BO} = E\psi_i(\vec{R}, \vec{r}), \quad (2.38)$$

where

$$\begin{aligned} \hat{U}_{BO} = & \frac{-1}{2\mu} \sum_i \left\langle \phi_j(\vec{R}, \vec{r}; \vec{R}_e) \left| \nabla_{\vec{R}}^2 + \nabla_{\vec{r}}^2 \right| \phi_i(\vec{R}, \vec{r}; \vec{R}_e) \right\rangle \psi_i(\vec{R}, \vec{r}) \\ & - \frac{1}{\mu} \sum_i \left\langle \phi_j(\vec{R}, \vec{r}; \vec{R}_e) \left| \nabla_{\vec{R}} + \nabla_{\vec{r}} \right| \phi_i(\vec{R}, \vec{r}; \vec{R}_e) \right\rangle \nabla_R \psi_i(\vec{R}, \vec{r}) \end{aligned} \quad (2.39)$$

and

$$\hat{V}_{BO} = \varepsilon_i(\vec{R}, \vec{r}). \quad (2.40)$$

The first and second terms of \hat{U}_{BO} in Eq. (2.39) define the second- and first-derivative non-adiabatic coupling between various electronic states.³⁰ In the adiabatic approximation, all of the off-diagonal ($i \neq j$) terms in \hat{U}_{BO} in Eq. (2.39) are ignored.³⁰ In the traditional Born-Oppenheimer approximation, even the diagonal terms in \hat{U}_{BO} in Eq. (2.39) are ignored,³⁰ so that the Schrödinger equation, in hyperspherical coordinates, becomes

$$\left(-\frac{1}{2\mu\rho^5} \frac{\partial}{\partial\rho} \rho^5 \frac{\partial}{\partial\rho} + \frac{\Delta^2}{2\mu\rho^2} + \hat{V}_{BO} \right) \psi_i(\vec{R}, \vec{r}) = E\psi_i(\vec{R}, \vec{r}). \quad (2.41)$$

In this approximation the nuclei move on the PES, \hat{V}_{BO} , which is the eigenvalue of the so called clamped nuclei electronic Hamiltonian $\hat{H}_e(\vec{R}, \vec{r}; \vec{R}_e)$.

Adiabatic and Diabatic Basis

The functions which diagonalize the electronic Hamiltonian \hat{H}_e in Eq. (2.35) define the adiabatic basis.³⁹ They have the properties:

$$\left\langle \phi_j \left| \hat{H}_e \right| \phi_i \right\rangle = \varepsilon_i \delta_{ij}, \quad (2.42)$$

and, as shown explicitly by Eq. (2.39),

$$\langle \phi_j | \hat{T}_n | \phi_i \rangle_{i \neq j} \neq 0. \quad (2.43)$$

In the treatment of reactive scattering involving the more than one electronic state, it is more convenient to use diabatic basis functions³⁹ ϕ^{dia} , which by definition have the properties:

$$\langle \phi_j^{dia} | \hat{H}_e | \phi_i^{dia} \rangle_{i \neq j} \neq 0, \quad (2.44)$$

and

$$\langle \phi_j^{dia} | \hat{T}_n | \phi_i^{dia} \rangle = 0. \quad (2.45)$$

The adiabatic and diabatic basis are related by a unitary transformation which is a function of the nuclear coordinates. Equation (2.45) results in ($\hat{U}_{BO} = 0$) in Eq. (2.39). This is the reason we use the diabatic basis to solve the multiple PES Schrödinger equation in section 2.1.4.

2.1.4 Solving the Schrödinger Equation

In this section we consider the method of solving the Schrödinger equation first on a single PES. We then extend the method to multiple PESs. Finally we introduce the additional coupling between the electronic states which is introduced by the spin-orbit Hamiltonian.

Single Potential Energy Surface

Similar to the expansion used in deriving the Born-Oppenheimer approximation, we solve the single PES Schrödinger equation in Eq. (2.41) by expanding the nuclear wavefunction $\psi_i(\vec{R}, \vec{r})$ in the eigenfunctions of the Δ^2 operator, $\Phi_n(\theta_\alpha, \hat{R}_\theta, \hat{R}_\phi, \hat{r}_\theta, \hat{r}_\phi)$, with expansion coefficients $C_n(\rho)$ which depend only on the hyperradius ρ :

$$\psi_i(\vec{R}, \vec{r}) = \sum_n \frac{1}{\rho^{5/2}} C_n(\rho) \Phi_n(\theta_\alpha, \hat{R}_\theta, \hat{R}_\phi, \hat{r}_\theta, \hat{r}_\phi). \quad (2.46)$$

Substituting Eq. (2.46) into Eq. (2.41) leads to a set of “close-coupled” equations for the expansion coefficient $C_n(\rho)$:⁴⁰

$$\frac{d^2}{d\rho^2} C_n(\rho) = 2\mu \sum_{n'} W_{nn'}(\rho) C_{n'}(\rho), \quad (2.47)$$

where

$$W_{nn'}(\rho) = \langle \Phi_n | \hat{H}_\rho | \Phi_{n'} \rangle \quad (2.48)$$

with

$$\hat{H}_\rho = \frac{\Delta^2}{2\mu\rho^2} + \hat{V}_{BO} + \frac{1}{2\mu} \frac{15}{4\rho^2} - E. \quad (2.49)$$

The reason we separate the term $1/\rho^{5/2}$ from $C_n(\rho)$ in Eq. (2.46) is that it can be factored out from the left and right hand sides of Eq. (2.47).

In general, Eq. (2.47) can then be solved using standard techniques.⁴⁰ However it is more efficient to replace the Φ_n in Eq. (2.46) with the basis functions that are the eigenfunctions of \hat{H}_ρ in Eq. (2.49) at a fixed ρ .^{33,36} Also notice that the Δ^2 in Eq. (2.34) contains the uncoupled terms \hat{j}^2 and \hat{L}^2 . Using the conservation of the total angular momentum $\vec{J} = \vec{j} + \vec{L}$, we define the basis functions,^{1,33,36,41,42}

$$\Phi_n \Rightarrow |JMK\alpha v j k\rangle = \frac{2}{\sin 2\theta} \left(\frac{2J+1}{4\pi} \right)^{1/2} D_{MK}^{J*}(\Omega_\alpha) Y_{jk}(\gamma_\alpha, 0) \Phi_{vj}(\theta_\alpha; \rho) \quad (2.50)$$

where J is the total angular momentum; M and K are the projections of J along the space-frame Z axis and along the Jacobi vector \vec{R}_α (the body frame z axis) as shown in Fig. 2.3(b); α indicates the reactant or product arrangements; v is the vibrational quantum number of the diatomic fragment; j is the rotational quantum number of the diatomic fragment with projection k along \vec{R}_α ; $D_{MK}^{J*}(\Omega_\alpha)$ is a Wigner rotation matrix;⁴³ $Y_{jk}(\gamma_\alpha, 0)$ is a spherical harmonic;⁴³ and $\Phi_{vj}(\theta_\alpha; \rho)$ is the solution of a vibrational referenced surface eigenvalue problem at a fixed ρ .³⁶

Using Eq. (2.50) to evaluate Eq. (2.48), we solve Eq. (2.47) by a sector by sector log-derivative propagation^{33,40} to extract the helicity-frame state-resolved reactive scattering S-matrix elements $S_{K\alpha v j k \rightarrow K' \alpha' v' j' k'}^J$.^{33,44} Note that \vec{L} is always perpendicular to the plane containing the Jacobi vector \vec{R}_α , thus the projection of \vec{L} along the Jacobi vector \vec{R}_α always equals zero which results in $K = k$ in Eq. (2.50).

Definite Parity Basis and Interchange Symmetry

We can reduce the size of the basis set by one half using the definite- K ($K \geq 0$) parity basis function $\Phi_n^\eta = |JMK\alpha v j k; \eta\rangle$,³⁹

$$\Phi_n^\eta = |JMK\alpha v j k; \eta\rangle = \frac{1}{\sqrt{2}} (|JMK\alpha v j k\rangle + \eta |JM, -K\alpha v j, -k\rangle), \quad (2.51)$$

where $\eta = \pm 1$. Notice that $\langle \Phi_n^{\eta=+1} | \hat{H} | \Phi_n^{\eta=-1} \rangle = 0$ as a result of the definition in Eq. (2.51).

In terms of the relation between the signed- K and definite- K basis functions, the S-matrix element is:³³

$$\begin{aligned} S_{K\alpha v j k \rightarrow K' \alpha' v' j' k'}^J &= S_{-K\alpha v j -k \rightarrow -K' \alpha' v' j' -k'}^J \\ &= \frac{1}{2} (S_{K\alpha v j k \rightarrow \alpha' v' j' k'}^{J, \eta=+1} + S_{K\alpha v j k \rightarrow \alpha' v' j' k'}^{J, \eta=-1}) \end{aligned} \quad (2.52)$$

and

$$\begin{aligned} S_{K\alpha v j k \rightarrow -K, \alpha' v' j' -k'}^J &= S_{-K, \alpha v j -k \rightarrow K' \alpha' v' j' k'}^J \\ &= \frac{(-1)^J}{2} (S_{K\alpha v j k \rightarrow K' \alpha' v' j' k'}^{J, \eta=+1} - S_{K\alpha v j k \rightarrow K' \alpha' v' j' k'}^{J, \eta=-1}) \end{aligned} \quad (2.53)$$

For a system, like F+H₂, containing the homonuclear H₂ molecule, the Hamiltonian is unchanged under the exchange of the two H nuclei, while the H₂ rotational wavefunctions $Y_{jk}(\gamma_\alpha, 0)$ in Eq. (2.50) have the symmetry $(-1)^j$ with respect this exchange. Consequently the matrix elements $\langle Y_{j'k'} | \hat{H} | Y_{jk} \rangle$ vanish unless j and j' are both even or both odd. Thus the basis need contain only even j (para-H₂) or odd j (ortho-H₂).

Multiple Potential Energy Surfaces

In the multiple PES calculations,^{1,42,45} we use the diabatic electronic states ϕ_i^d defined in Eq. (2.44) and (2.45), or explicitly,¹

$$\phi_i^{dia} = |\lambda\sigma\rangle_\alpha, \quad (2.54)$$

where α indicates the reactant or product arrangements; λ and σ are the projection of electronic and spin angular momenta along the Jacobi vector \vec{R}_α .

With Eq. (2.54), using the expansion in Eq. (2.36), and working through the same procedure in Eq. (2.37) and (2.38), the Schrödinger equation becomes,

$$\hat{T}_n \psi_i(\vec{R}, \vec{r}) + \sum_j \langle \phi_i^{dia} | \hat{H}_e | \phi_j^{dia} \rangle \psi_j(\vec{R}, \vec{r}) = E \psi_i(\vec{R}, \vec{r}). \quad (2.55)$$

Note that the $\hat{U}_{BO} = 0$ in Eq. (2.38-2.39) as a fact of Eq. (2.45).

For a two electronic state system, Eq. (2.55) becomes, in matrix form,⁴⁶

$$\left[\hat{T}_n \begin{pmatrix} 1 & 0 \\ 0 & 1 \end{pmatrix} + \begin{pmatrix} \hat{H}_{e,11} & \hat{H}_{e,12} \\ \hat{H}_{e,21} & \hat{H}_{e,22} \end{pmatrix} \right] \begin{pmatrix} \psi_1 \\ \psi_2 \end{pmatrix} = E \begin{pmatrix} \psi_1 \\ \psi_2 \end{pmatrix}, \quad (2.56)$$

where

$$\hat{H}_{e,ij} = \langle \phi_i^{dia} | \hat{H}_e | \phi_j^{dia} \rangle. \quad (2.57)$$

We can extend the basis function of Eq. (2.50) by explicit inclusion of the electronic state $\phi_i^{dia} = |\lambda\sigma\rangle_\alpha$, obtaining,^{1,42,45}

$$\Phi_{ni} \Rightarrow |JMK\alpha vjk, \lambda\sigma\rangle = \frac{2}{\sin 2\theta} \left(\frac{2J+1}{4\pi} \right)^{1/2} D_{MK}^{J*}(\Omega_\alpha) Y_{jk}(\gamma_\alpha, 0) \Phi_{vj}(\theta_\alpha; \rho) |\lambda\sigma\rangle_\alpha, \quad (2.58)$$

where

$$K = \lambda + \sigma + k. \quad (2.59)$$

Similar to the procedures of Eq. (2.46-2.50) in the single PES calculation, Eq. (2.56) can be solved¹ to extract the helicity-frame state-resolved reactive scattering S-matrix elements,

$$\begin{aligned}
S_{K\alpha\nu jk\lambda\alpha\rightarrow K'\alpha'\nu'j'k'\lambda'\alpha'}^J &= S_{-K\alpha\nu j,-k,-\lambda,-\alpha\rightarrow K'\alpha'\nu'j',-k',-\lambda',-\alpha'}^J \\
&= \frac{1}{2} (S_{K\alpha\nu jk\lambda\alpha\rightarrow K'\alpha'\nu'j'k'\lambda'\alpha'}^{J,\eta=+1} + S_{K\alpha\nu jk\lambda\alpha\rightarrow K'\alpha'\nu'j'k'\lambda'\alpha'}^{J,\eta=-1})
\end{aligned} \tag{2.60}$$

and

$$\begin{aligned}
S_{K\alpha\nu jk\lambda\alpha\rightarrow K'\alpha'\nu'j',-k',-\lambda',-\alpha'}^J &= S_{-K\alpha\nu j,-k,-\lambda,-\alpha\rightarrow K'\alpha'\nu'j'k'\lambda'\alpha'}^J \\
&= \frac{1}{2} (S_{K\alpha\nu jk\lambda\alpha\rightarrow K'\alpha'\nu'j'k'\lambda'\alpha'}^{J,\eta=+1} - S_{K\alpha\nu jk\lambda\alpha\rightarrow K'\alpha'\nu'j'k'\lambda'\alpha'}^{J,\eta=-1})
\end{aligned} \tag{2.61}$$

Comparing to the procedures in single PES calculation, the differences are the replacement of Φ_n in Eq. (2.48) by Φ_{nt} in Eq. (2.58) and the replacement of the \hat{V}_{BO} term in Eq. (2.49) by $\hat{H}_{e,ij}$ in Eq. (2.57).

Spin-Orbit Coupling

The first order correction to the electronic Hamiltonian \hat{H}_e in Eq. (2.55) is to include the spin-orbit Hamiltonian \hat{H}_{so} , which represents the interactions arising from the couplings between the Spin (\vec{S}) and electronic (\vec{L}) orbital angular momenta. Explicitly,

$$\hat{H}_{so} = a_{so}(\vec{R}, \vec{r}) \cdot \vec{S} \cdot \vec{L}, \tag{2.62}$$

where $a_{so}(\vec{R}, \vec{r})$ is the spin-orbit coupling constant whose values depends on the relative position of Jacobi vectors (\vec{R}, \vec{r}) [Eq. (2.13)]. For the F+H₂ asymptote, a_{so} is the same as the spin-orbit coupling constant of F atom, 269 cm⁻¹. The effect of \hat{H}_{so} on the PES is discussed in more detail in the next paragraph. The matrix elements of \hat{H}_{so} give rise to additional couplings between different electronic states. The procedures used for the multiple PES calculations can be used unchanged.

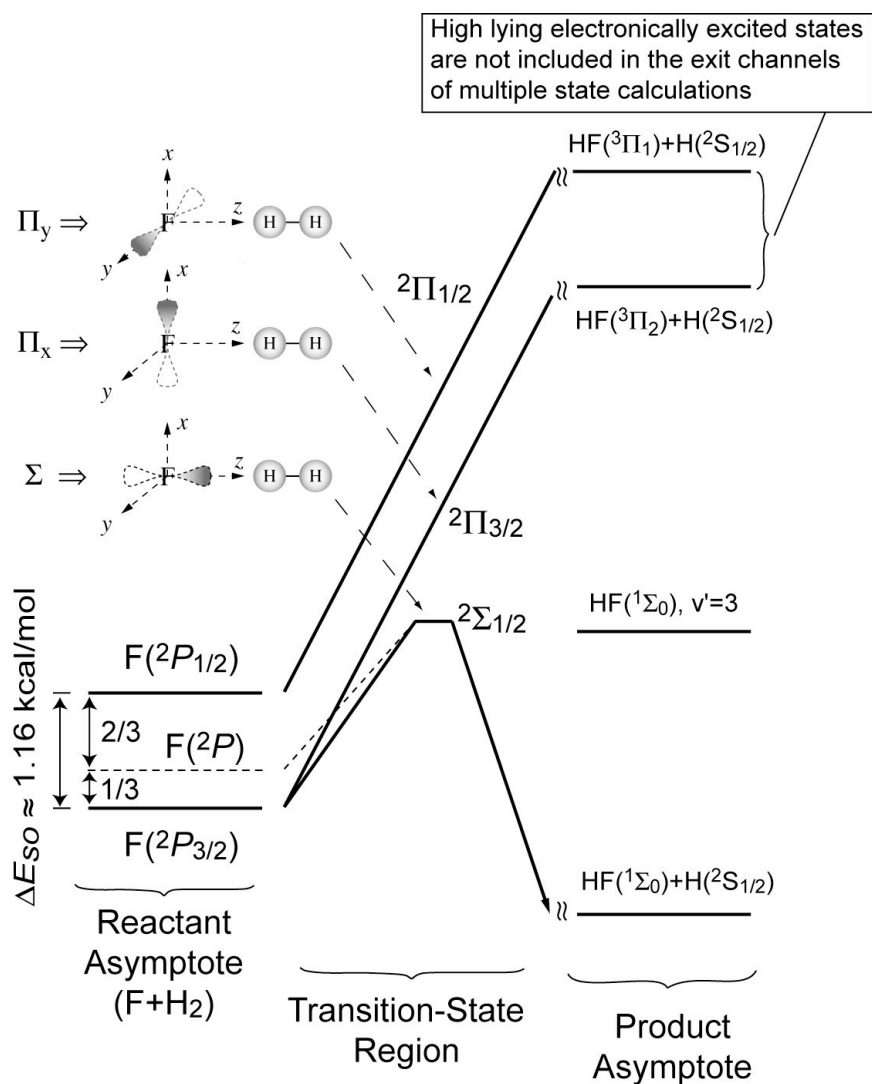


Figure 2.4 Schematic drawing of the PESs for the reaction of $F+H_2 \rightarrow HF+H$ in the reactant asymptote region, transition state region and the product asymptote region. Only the energy levels of the spin-orbit coupling states are drawn to scale. The upper left corner shows the electronic correlation diagram for collinear geometry. The unpaired F $2p$ orbital can point along the z (p_z), x (p_x) or y (p_y) axes to form Σ , Π_x or Π_y electronic states. After inclusion of the electron spin these correlate with the $^2\Sigma_{1/2}$, $^2\Pi_{3/2}$ and $^2\Pi_{1/2}$ states in the transition state region. The dashed line indicates the PES without spin-orbit coupling.

As shown in Fig. 2.4, the effect of the spin-orbit coupling on the PES^{1,4,12} is best illustrated in collinear geometry. In the reactant asymptote the inclusion of spin-orbit coupling splits the degenerate F(2P) states into ground $^2P_{3/2}$ and spin-orbit excited $^2P_{1/2}$ states separated by 404 cm^{-1} (1.16 kcal/mol).⁴⁷ The spin-orbit Hamiltonian does not contribute either to the closed-shell H₂ ground state ($^1\Sigma_0$) or to the HF+H product states, since HF ($^1\Sigma_0$) has a closed shell and $l = 0$ for the H (2S) ground state. In the transition-state region, because of the large splitting between the Σ and Π states and the small value of the spin-orbit coupling,¹² the reactive surface ($^1\Sigma_{1/2}$ in collinear geometry) is not coupled significantly with the non-reactive Π states.^{1,4,12} Therefore the effect of the spin-orbit coupling gradually vanishes [see Fig. 5(a) in Ref. 12]. In summary, the spin-orbit coupling lowers the energy of the F+H₂ reactants and leaves the reactive PES in the transition-state region unchanged. Consequently, the reaction barrier is effectively raised by about 1/3 of the spin-orbit coupling (0.385 kcal/mol).^{1,4,12,42}

The presence of the spin-orbit Hamiltonian has several consequences for the scattering dynamics.¹⁷⁻²¹ First, the tunneling probability for the near isothermal reaction: F $^2P_{3/2} \rightarrow$ HF $^1\Sigma_0$ ($v' = 3$), decreases as a result of the increased reaction barrier. Thus the forward scattering peak in the differential cross section, which is due mainly to the scattering into the HF $v' = 3$ state, is reduced.²⁰ Secondly the presence of the higher energy spin-orbit excited state $^2P_{1/2}$ can enhance the probability of direct reaction without resonance and tunneling effects. This depends on the strength of the coupling between the ground and the excited spin-orbit states. Thirdly, non-adiabatic transitions open a channel for electronically inelastic scattering, which can reduce the probability of chemical reaction.^{17,18} Furthermore, due to the F spin-orbit splitting, the reactions from ground (F $^2P_{3/2}$) and spin-orbit excited (F $^2P_{1/2}$) states will lead to substantially different kinetic energies of final HF products, which will be manifested

in LAB ADs.¹⁹ The detailed investigation of these effects is the main focus of this dissertation and will be described in Chapters 3-5.

2.2 Experimental Observables

2.2.1 Differential and Integral Cross Sections

The connection between the experimental measurements and the theoretical calculations are differential [$d\sigma(\theta)$]^{48,49,50} and integral [σ] cross sections:^{33,44}

$$d\sigma_{if}(\theta) = \left| \frac{1}{2ik_{in}} \sum_J (2J+1) d_{KK'}^J(\pi-\theta) S_{if}^J \right|^2, \quad (2.63)$$

$$\sigma_{if} = \int \sigma_{if}(\theta) d\Omega = \frac{\pi}{k_{in}^2} \sum_J (2J+1) |S_{if}^J|^2, \quad (2.64)$$

where the subscript if designates a particular initial-to-final transition; S_{if}^J is the scattering matrix element in Eqs. (2.52-2.53) or Eqs. (2.60-2.61) for single and multi PES respectively; and $d_{KK'}^J$ is a Wigner reduced rotation matrix element.⁴³ The reason to use $(\pi-\theta)$ rather than θ in Eq. (2.63) is because the experimental angle is conventionally referenced to the F beam,¹⁰ while the angle of $d_{KK'}^J$, defined in Ref. 43 is referenced to the H₂ beam.

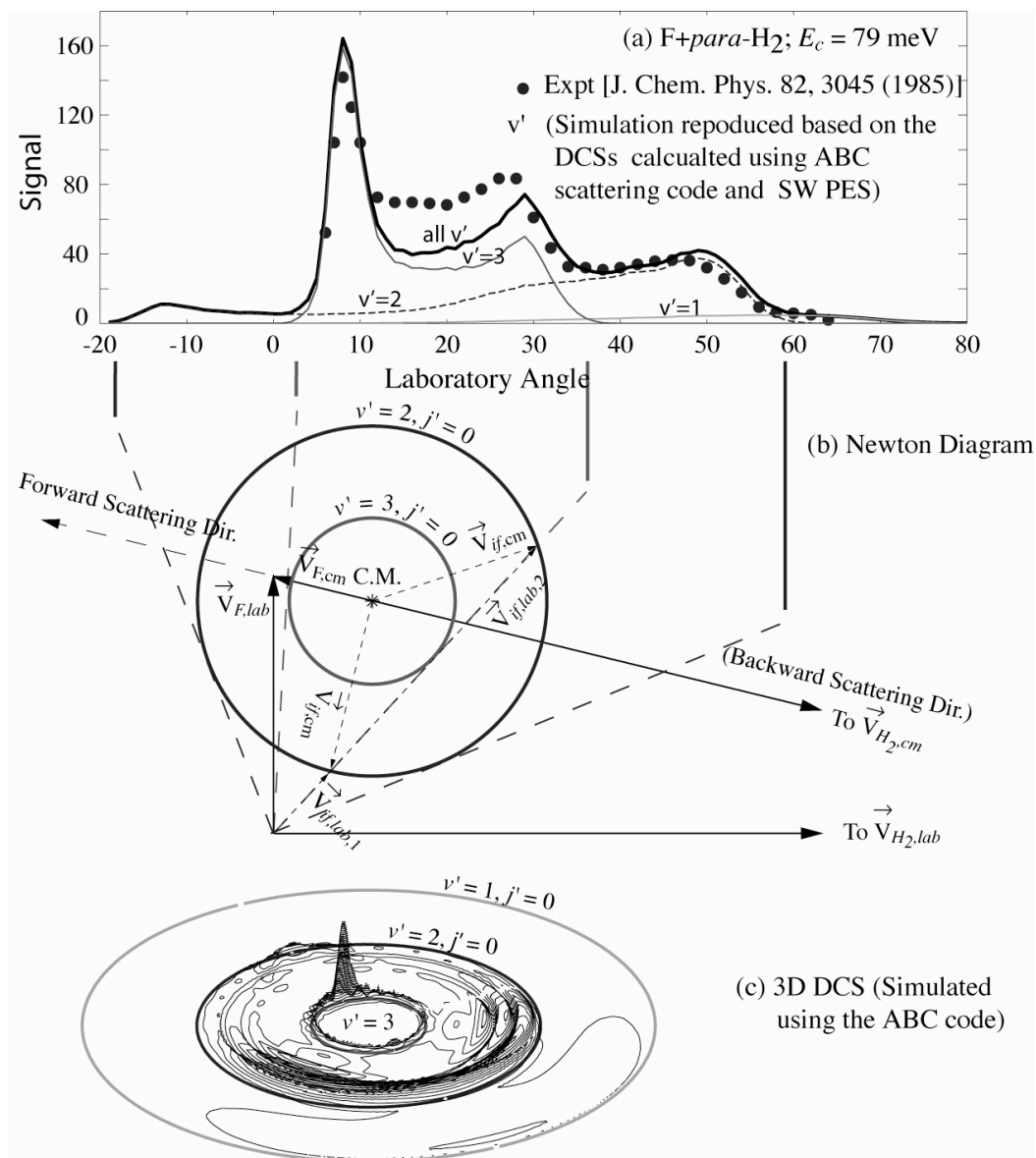


Figure 2.5 (a) Experimental data (●) from Ref. 10 and simulated (solid line) LAB AD⁵² for the reaction of $F+\text{para-H}_2$ at a collision energy of 79 meV. (b) Kinematic (Newton) diagram and (c) Simulated DCS (reproduced using the ABC scattering code³³) in the scattering angle–recoil velocity 3D contour map at this collision energy. The thick solid lines indicate the maximum relative velocities for HF produced in the lowest ($j'=0$) rotational level of the $v'=1, 2$ and 3 manifolds.

2.2.2 Laboratory Angular Distribution and Newton Diagram

The scattering angle θ in Eq. (2.63) is measured relative to the nuclear CM coordinates. However, the experiment measures the laboratory angular distributions (LAB ADs) which refer to a space fixed coordinate system. As shown in Fig. 2.5, the relationship between the CM DCS and the LAB AD is best illustrated by a velocity (or Newton) diagram.⁵¹ The main principle is that the relative velocity

$$\vec{V}_{rel} = \vec{V}_{F,lab} - \vec{V}_{H_2,lab} = \vec{V}_{F,cm} - \vec{V}_{H_2,cm} \quad (2.65)$$

is a direct measure of the available kinetic energy T_{rel} in the CM coordinate,

$$T_{tot} = \frac{1}{2} m_F V_{F,lab}^2 + \frac{1}{2} m_{H_2} V_{H_2,lab}^2 = \underbrace{\frac{1}{2} M_{nuc} V_{CM}^2}_{T_{CM}} + \underbrace{\frac{1}{2} M_{CM} V_{rel}^2}_{T_{rel}}. \quad (2.66)$$

By conservation of energy and momentum,

$$T_{rel} = \underbrace{\frac{1}{2} m_H V_{H,cm}^2 + \frac{1}{2} m_{HF} V_{HF(v'j'),cm}^2}_{T_{prod,rel}} + \underbrace{U_{HF(v'j')}}_{U_{prod}}, \quad (2.67)$$

and

$$m_H \vec{V}_{H,cm} = m_{HF} \vec{V}_{HF(v'j'),cm}, \quad (2.68)$$

the angular distribution of the product HF($v'j'$) is constrained to a circle with radius

$$V_{HF(v'j'),cm}.$$

Beam Spread and Energy Dispersion

Because of the unavoidable spatial spread and energy dispersion in any molecular beam, together with the finite size of the detector acceptance angle, a convolution is needed for a quantitative comparison between the experimental and theoretical results. First described in detail by Warnock and Bernstein in 1968⁵³ and numerically applied by Aoiz,¹⁴ the convolution contains the following major procedures:

First, let us focus on a particular pair of F-and-H₂ velocity vectors ($\vec{V}_{F,lab}, \vec{V}_{H_2,lab}$), or in other words, assume there is no spatial spread or energy dispersion in the F and H₂ molecular beam. Thus, for a particular initial-to-final transition, the flux (number of particles per unit time) collected by a point detector at a chosen laboratory angle θ_{lab} , $I_{pseudo}(\theta_{lab})$, is

$$I_{pseudo}(\theta_{lab}) = \Delta V n_F n_{H_2} V_{rel} d\sigma_{if}(\theta_{cm} \leftarrow \theta_{lab}, V_{rel}). \quad (2.69)$$

where n_F and n_{H_2} are the F and H₂ particle densities per unit volume and ΔV is the scattering volume defined by the intersection of the F and H₂ beams. Here we use the subscript “pseudo” to distinguish the un-convoluted flux I_{pseudo} from the fully convoluted flux I .

Taking into account the finite size of the detector acceptance angle (or solid angle $d\Omega_{lab}$), we have a solid-angle convoluted flux $I_{d\Omega_{lab}}(\theta_{lab})$ which, by conservation of flux, is an integral of the differential cross section $d\sigma_{if}(\theta_{cm})$ over all CM angles (θ_{cm}, ϕ_{cm}) which correspond to the range of the detector solid angle at θ_{lab} ,

$$I_{d\Omega_{lab}}(\theta_{lab}) = \Delta V n_F n_{H_2} V_{rel} \iint_{(\theta_{cm}, \phi_{cm}) \leftarrow d\Omega_{lab}} \sin(\theta_{cm}) d\theta_{cm} d\phi_{cm} d\sigma_{if}(\theta_{cm}, V_{rel}). \quad (2.70)$$

The CM angles (θ_{cm}, ϕ_{cm}) in Eq. (2.70) are both functions of the laboratory angles (θ_{lab}, ϕ_{lab}). This complicated relation between the CM and laboratory angles gives rise to an irregular range of (θ_{cm}, ϕ_{cm}) integration. As a result, it is more convenient to evaluate $I_{d\Omega_{lab}}(\theta_{lab})$ in the laboratory frame where we can use a uniform grid for the integration over the detector solid angle. To do so, several steps of transformation and approximations are needed.⁵³

First, for each particular initial-to-final transition, we assume a delta function distribution of CM product velocities, $\int \delta(V_{if,cm}) dV_{if,cm} = 1$, so that Eq. (2.70) becomes,

$$I_{d\Omega_{lab}}(\theta_{lab}) \approx \Delta V n_F n_{H_2} V_{rel} \iiint_{(\theta_{cm}, \phi_{cm}) \leftarrow d\Omega_{lab}} d\theta_{cm} d\phi_{cm} dV_{if,cm} \delta(V_{if,cm}) \sin(\theta_{cm}) d\sigma_{cm}(\theta_{cm}, V_{rel}). \quad (2.71)$$

Then by means of the transformation of integral theorem

$$\int F(\vec{X}) d\vec{X} = \int F(\vec{Y}) \cdot \left| \frac{\partial \vec{X}}{\partial \vec{Y}} \right| d\vec{Y}, \quad (2.72)$$

Eq. (2.71) becomes

$$I_{d\Omega_{lab}}(\theta_{lab}) \approx \Delta V n_F n_{H_2} V_{rel} \iiint_{lab} d\theta_{lab} d\phi_{lab} dV_{if,lab} \delta(V_{if,cm}) J_{cm \rightarrow lab} \sin(\theta_{cm}) d\sigma_{if}(\theta_{cm}, V_{rel}) \quad (2.73)$$

where $J_{cm \rightarrow lab}$ is the Jacobian of the integral transformation,

$$J_{cm \rightarrow lab} = \left| \frac{\partial \vec{V}_{if,cm}}{\partial \vec{V}_{if,lab}} \right| = \left| \frac{\partial(\theta_{cm}, \phi_{cm}, V_{if,cm})}{\partial(\theta_{lab}, \phi_{lab}, V_{if,lab})} \right| = \frac{V_{if,lab}^2 \cos(\theta_{lab})}{V_{if,cm}^2 \sin(\theta_{cm})}, \quad (2.74)$$

with $\vec{V}_{if,lab}$ being a product velocity vector in the laboratory frame which corresponds to a given $\vec{V}_{if,cm}$ in Eq. (2.71).

We then use a standard property of CM-to-LAB frame transformation for a delta function,^{50,53}

$$\delta(V_{if,cm}) = \delta(V_{if,lab}) \left| \frac{\partial V_{if,cm}}{\partial V_{if,lab}} \right| = \frac{\delta(V_{if,lab})}{|\cos \zeta|}, \quad (2.75)$$

with ζ being the angle between $\vec{V}_{if,cm}$ and $\vec{V}_{if,lab}$.

Substituting Eqs. (2.74-2.75) back into Eq. (2.73), we find

$$I_{d\Omega_{lab}}(\theta_{lab}) \approx \Delta V n_F n_{H_2} V_{rel} \sum_{q=1,2} \iint_{lab} d\Omega_{lab} \frac{V_{if,lab,q}^2}{V_{if,cm}^2} \frac{1}{|\cos \zeta_q|} d\sigma_{if}(\theta_{cm,q}, V_{rel}) \quad (2.76)$$

where $d\Omega_{lab} = \cos \theta_{lab} d\theta_{lab} d\phi_{lab}$ is the solid angle in the laboratory frame with the convention that θ_{lab} is measured from the Y axis (the F beam direction) and the index ($q = 1, 2$) refers to the fast ($\vec{V}_{if,lab,2}$) and slow ($\vec{V}_{if,lab,1}$) component of $\vec{V}_{if,lab}$ (see Fig. 2.5).

The second approximation treats the integrand in Eq. (2.76) as a constant over the small range of the detector acceptance angle $d\Omega_{lab}$. Integrating symbolically, we find

$$I_{d\Omega_{lab}}(\theta_{lab}) \approx \Delta\Omega_{lab} \Delta V n_F n_{H_2} V_{rel} F_{d\Omega_{lab}}(\theta_{lab}), \quad (2.77)$$

where $F_{d\Omega_{lab}}(\theta_{lab})$ is the solid angle convoluted LAB AD,

$$F_{d\Omega_{lab}}(\theta_{lab}) = \sum_{q=1,2} \frac{V_{if,lab,q}^2}{V_{if,cm}^2} \frac{1}{|\cos \zeta_q|} d\sigma_{if}(\theta_{cm,q} \leftarrow \theta_{lab}, V_{rel}). \quad (2.78)$$

The next procedure of convolution is to vary the value of $|\vec{V}_{F,lab}|$ and $|\vec{V}_{H_2,lab}|$, or equivalently to vary the value of V_{rel} as expected from Eq. (2.65). Averaging over the joint probability function $P(V_{F,lab}, V_{H_2,lab})$, we have a $d\Omega_{lab}$ and V_{rel} convoluted flux

$$\begin{aligned} I_{d\Omega_{lab}, dV_{rel}}(\theta_{lab}) &\approx \iint_{lab} dV_{F,lab} dV_{H_2,lab} P(V_{F,lab}, V_{H_2,lab}) I_{d\Omega_{lab}}(\theta_{lab}) \\ &= \Delta\Omega_{lab} \Delta V n_F n_{H_2} \times \left[\iint dV_{F,lab} dV_{H_2,lab} P(V_{F,lab}, V_{H_2,lab}) V_{rel} F_{d\Omega_{lab}}(\theta_{lab}) \right]. \end{aligned} \quad (2.79)$$

Our last procedure of convolution is to vary the direction of $\vec{V}_{F,lab}$ and $\vec{V}_{H_2,lab}$ which has two consequences. First, this brings in additional V_{rel} convolution as expected from Eq. (2.65). Secondly, this changes the position vector \vec{r} defined by the intersection of the paired F-and- H_2 vectors ($\vec{V}_{F,lab}, \vec{V}_{H_2,lab}$). Since all the quantities of $I_{d\Omega_{lab}, dV_{rel}}$ in Eq. (2.79) depends on \vec{r} , a fully (\vec{r} , $d\Omega_{lab}$ and V_{rel}) convoluted flux I becomes,

$$\begin{aligned} I(\theta_{lab}) &\approx \int d\vec{r} I_{d\Omega_{lab}, dV_{rel}}(\theta_{lab}) \\ &= \int d\vec{r} n_F(\vec{r}) n_{H_2}(\vec{r}) \times \left[\Delta\Omega_{lab} \iint dV_{F,lab} dV_{H_2,lab} P(V_{F,lab}, V_{H_2,lab}) V_{rel} F_{d\Omega_{lab}}(\theta_{lab}) \right]_{\vec{r}}. \end{aligned} \quad (2.80)$$

Here the scattering volume ΔV in Eq. (2.79) has been absorbed into a volume integral of $\int d\vec{r}$ in Eq. (2.80).

Approximating $\Delta\Omega_{lab}$ as a constant for each position vector \vec{r} over the small scattering volume and rewriting the double integral, $\left[\iint dV_{F,lab}dV_{H_2,lab}\right]_{\vec{r}}$, in Eq. (2.80) in the vector form, we have,

$$I(\theta_{lab}) \approx \Delta\Omega_{lab} \int d\vec{r} n_F(\vec{r}) n_{H_2}(\vec{r}) \iint d\vec{V}_{F,lab} d\vec{V}_{H_2,lab} P(V_{F,lab}, V_{H_2,lab}) \times \left[V_{rel} F_{d\Omega_{lab}}(\theta_{lab})\right]_{\vec{r}, \vec{V}_{F,lab}, \vec{V}_{H_2,lab}} \quad (2.81)$$

Equation (2.81) is a standard form for Monte-Carlo integration and can be evaluated efficiently.

The advantage of the approximations and transformations in Eq. (2.71-2.78) is ease of subsequent numerical integration in Eq. (2.81). However, due to the CM-to-LAB frame transformation in Eq. (2.71), there exists a singularity in Eq. (2.78) when $\zeta = \pi/2$. Usually, the singularity can be avoided in a careful numerical integration or it can be averaged out in the Monte-Carlo integration. However, when the detector is located so that $\zeta = \pi/2$, it is necessary to go back to Eq. (2.70) and carry the integration explicitly in the relative coordinate.

3 The $F+H_2 \rightarrow HF+H$ Reaction

3.1 Introduction

The historical background for the study of the $F+H_2$ reaction was described in Chapter 1. The same terminology is also followed: we use the term DCS to denote the center-of-mass frame differential cross sections, and the term AD to determine the LAB frame differential cross section.

The goal of this Chapter is the investigation of whether the full open-shell character of the reaction is responsible for the discrepancies between the experimental ADs and the earlier simulations. A few years ago, Alexander and co-workers have presented a framework for the theoretical treatment of reactions involving multiple potential energy surfaces (PES).¹ We then applied this treatment to the determination of reaction probabilities and integral cross sections for the $F+H_2$ and $Cl+H_2$ reactions.^{1,17} More recently, Han and co-workers have carried out similar time-dependent studies of these reactions.^{7,54,55} This past year we have extended the formalism to the determination of differential cross sections (DCSs) for abstraction reactions involving an open-shell atom.⁸

In general, because of its lower statistical weight and because, as shown in Fig. 2.4, there are no adiabatic reactive pathways between the spin-orbit excited state and the electronic ground-state of the products ($HF+H$),^{1,56,57} the excited spin-orbit state does not make a significant contribution to the overall reaction probability.¹ However, in several studies of the $F+HD \rightarrow HF+D$ reaction we have shown that the excited spin-orbit state is responsible for noticeable features in the reaction.²¹ For this reaction, the integral cross section for reaction of the ground spin-orbit state of F shows a strong resonance feature at low collision energies,²² but that of F^* does not.²¹ As a result, the exact shape of the resonance feature in the energy dependence

of the overall reaction cross section will be a sensitive function of the amount of F^* present in the beam.²¹

Reaction of F^* to yield HF products in the electronic ground state must involve a non-adiabatic transition to a lower PES (Fig. 2.4). Accordingly, the resulting product ADs may differ from that for reaction of atoms in the ground spin-orbit state. Furthermore, the existence of spin-orbit and other non-adiabatic couplings between the various PESs may result in ADs which differ from those simulated by calculations on a single PES. Speculation about the magnitude of these effects have appeared in the literature.^{4,10,11,14}

In this Chapter we attempt to answer these questions by determining the state resolved DCSs of F and F^* and then performing a CM-to-LAB transformation to compare the predicted ADs with experiment. It will thereby be possible to clarify unambiguously whether the experimental ADs provide information on the reactivity of the spin-orbit excited atoms. The organization of this Chapter is as follows: Sections 3.2 and 3.3 contain a brief review of the FH_2 PESs and scattering methods used. In Sec. 3.4, we present and discuss the calculated DCSs and ADs with the goal of clarifying and separating the contribution due to reaction of the excited spin-orbit state and the contribution due to non-adiabatic effects during the reaction of the ground spin-orbit state. A brief conclusion follows.

3.2 Potential Energy Surfaces

Approach of an F atom in a 2P electronic state to molecular hydrogen gives rise to three states ($1^2A'$, $2^2A'$, and $1^2A''$). This is shown schematically in Fig. 2.4. The three electronically adiabatic PESs can be transformed into four quasi-diabatic PESs. The two diabatic PESs of A' symmetry are coupled by a fourth PES, which is the off-diagonal electrostatic coupling in the quasi-diabatic basis. The states are also coupled by spin-orbit and Coriolis terms in the total Hamiltonian.

Stark and Werner carried out high-quality *ab initio* calculations of the lowest electronically adiabatic PES, and then produced a global fit to these *ab initio* points.¹² This is designated the SW PES. Subsequently, Hartke, Stark, and Werner diagonalized the spin-orbit Hamiltonian in the full electronic basis, added this to the lowest electronically adiabatic PES, and refit the results.¹⁵ This fit is known as the Hartke-Stark-Werner (HSW) PES. Subsequently, Alexander and Werner^{1,58} extended the original calculations of Stark and Werner in the F+H₂ arrangement, transformed to the quasi-diabatic basis mentioned above, and fit the resulting four quasi-diabatic PESs as well as the coordinate dependence of the spin-orbit coupling. These fits are called the Alexander-Stark-Werner (ASW) PESs.

The effect of the spin-orbit coupling on the lowest ASW PES has been described in Chapter 2.1.4 (see the text of Figure 2.4). In summary, the spin-orbit coupling lowers the energy of the F+H₂ reactants and leaves the reactive PES in the transition-state region unchanged. Consequently, the reaction barrier is effectively raised by about 1/3 of the spin-orbit coupling (0.385 kcal/mol).^{1,4,12,42}

3.3 Reactive Scattering Calculations

We use a close-coupled, time independent method,¹ as described in Chapter 2.1. The scattering wavefunction is expanded in an over-complete set of products of electronic-vibrational-rotational states for each of the arrangement channels [Eq. (2.50 and 2.58)].^{1,33,59} Canonical orthogonalization⁶⁰ is then used to construct the surface eigenfunctions in each sector. A constant-reference-potential, log-derivative propagator^{33,40} is employed to integrate the coupled-channel equations. For the single-state calculations (SW and HSW), the ABC code of Manolopoulos and co-workers³³ was used. For the multi-state calculations (ASW), we use the same code, but modified extensively as described previously.¹ We refer the reader to these earlier publications and the descriptions in Chapter 2.1; here we summarize those equations relevant to the present investigation.

3.3.1 Reactive Scattering Matrix Elements and Differential Cross Sections

Because a definite- K ($K \geq 0$) parity basis [Eq. (2.51)]³⁹ is used in all the calculations, we use Eq. (2.52-2.53) for single state calculations³³ and Eq. (2.60-2.61) for multiple state calculations to extract the helicity-frame^{33,44} state-resolved reactive scattering S matrix elements. Note that Eq. (2.53) and Eq. (2.61) are different not only in the subscripts but also by a pre-factor of $(-1)^J$, which would be a complex number in the multi-state calculations, where J is half-integer.

The molecular beam experiment,¹⁰ in which we compare, measured the differential cross sections (DCSs). In the helicity frame and in terms of the S matrix elements, DCSs are defined as Eq. (2.62).^{33,44}

3.3.2 Laboratory Angular Distributions

A crossed beam experiment determines angular distributions (ADs) which refer to a space-fixed (laboratory) coordinate system, which we designate by LAB AD. The relationship between the DCS, in which the scattering angle is defined with respect to the Jacobi vector of the product arrangement, and the LAB AD is illustrated by the velocity (Newton) diagram⁵¹ shown in Fig. 2 of Ref. 10, or in more detail, shown in Fig. 2.5 of Chapter 2.2.2. Also, a quantitative comparison with experiment must include a convolution over the spatial spread and energy dispersion of the molecular beams, together with the finite size of the detector acceptance angle. To carry out this convolution we use the program developed by Aoiz and co-workers.⁶¹ This program involves reducing the CM-to-LAB frame transformation⁵³ to a form amenable to Monte-Carlo integration^{53,61,62} as shown in Eq. (2) of Ref. 61, or in more detail, as described in Chapter 2.2.2.

Table 3.1 Summary of parameters which define the scattering calculations on the SW, HSW, and ASW PESs.

	J^a	j_{max}^a	k_{max}^a	K_{max}^a	$E_{max}(\text{eV})^a$	$\rho_{max}(\text{bohr})^a$	N_S^a
SW/HSW	0–30	15	4	NA ^b	2.0	12	150
ASW	0.5–30.5	15	NA ^c	3.5	1.7	12	100

- a. J is the total angular momentum; K is the projection of J along the Jacobi vector \vec{R}_α (the body frame z -axis), where the subscript α designates the chemical arrangement; j is the rotational quantum number of the diatomic fragment with projection k along \vec{R}_α and E is the total energy of the system in the CM frame. The subscript “max” in (j , k , K , and E) designate the parameters which delimit the size of the channel basis: all values up to these limits are included.^{1,33} The parameters ρ_{max} and N_S are the maximum value of the hyperradius ρ and the number of sectors used in a scattering calculation.³³
- b. For calculations on a single PES (SW and HSW), K_{max} equals k_{max} and therefore is not specified.
- c. For calculations on multiple PES (ASW), k_{max} depends on the values of K_{max} and on the collision arrangements ($K_{max} = k_{max} + \lambda + \sigma$).

3.3.3 Scattering Calculations and Initial State Populations

Table 3.1 lists the parameters which define the numerical details of our scattering calculations on the SW, HSW and ASW PESs. The subscript “max” (j , k , K and E) defines the size of the channel basis such that only states with indices which are less than or equal to these values are included. The parameters ρ_{max} and N_S are the ending point and number of steps used in the numerical propagation.

Table 3.2 Weighting of H₂ rotational levels used in simulation of the 1985 experiments of Neumark *et al.* (Ref. 10)

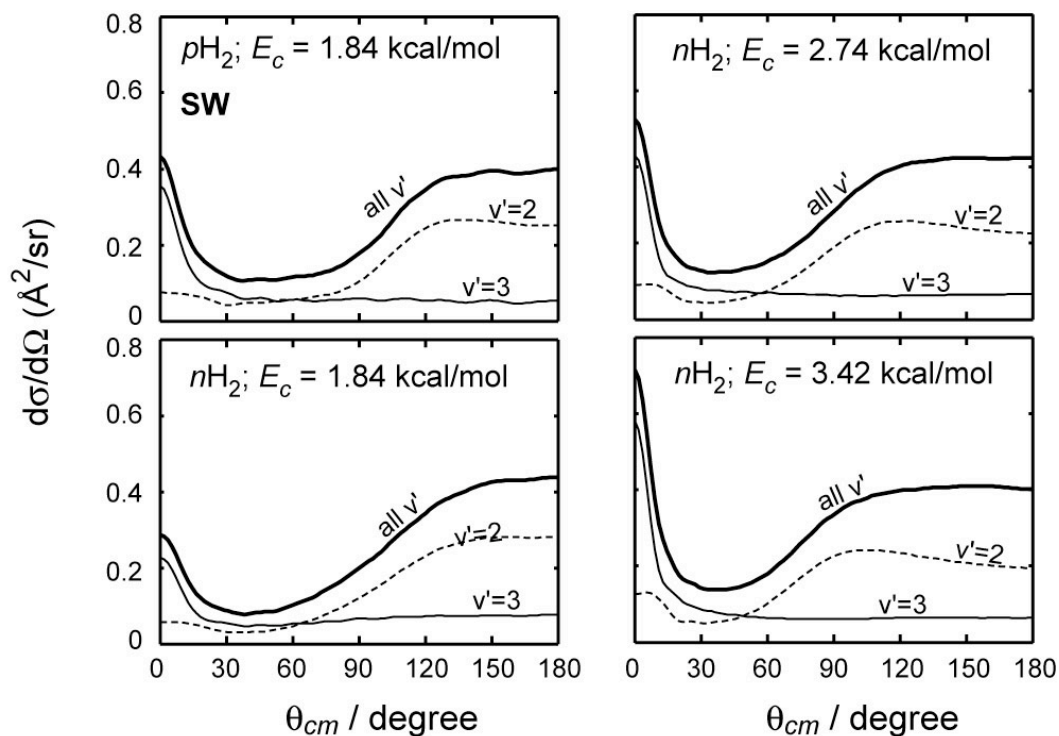
System	E_c (kcal/mol)	$j = 0$	$j = 1$	$j = 2$
$p\text{H}_2$	1.84	0.80	0	0.20
$n\text{H}_2$	1.84	0.20	0.74	0.06
$n\text{H}_2$	2.74	0.15	0.69	0.16
$n\text{H}_2$	3.42	0.12	0.64	0.24

To simulate the 1985 experiments, the calculated DCS (or CM AD) and LAB AD are summed over all the possible product states, including projection quantum numbers, and averaged over the degeneracy of the initial H₂ rotational level. To compare with experiment it is necessary to average the calculated cross sections over a weighted distribution of rotational levels in the initial H₂ beam. Table 3.2 lists these weighting factors for comparison with the experiments on $p\text{H}_2$ and $n\text{H}_2$. In addition, from our study of the F* reactivity in the F+HD reactions in Chapter 5, we find that the relative populations of the ground and excited F spin-orbit states in the beam is best described by a Boltzmann distribution at the temperature of 600K which characterizes the F atom velocity in the atom source used by Liu and co-workers.²³ Since the experiment of Neumark *et al.*,¹⁰ in which we compare, described a similar F atom velocity, we therefore apply the same relative populations of F and F* in this calculations, so that F*:F=0.16:0.84.²³

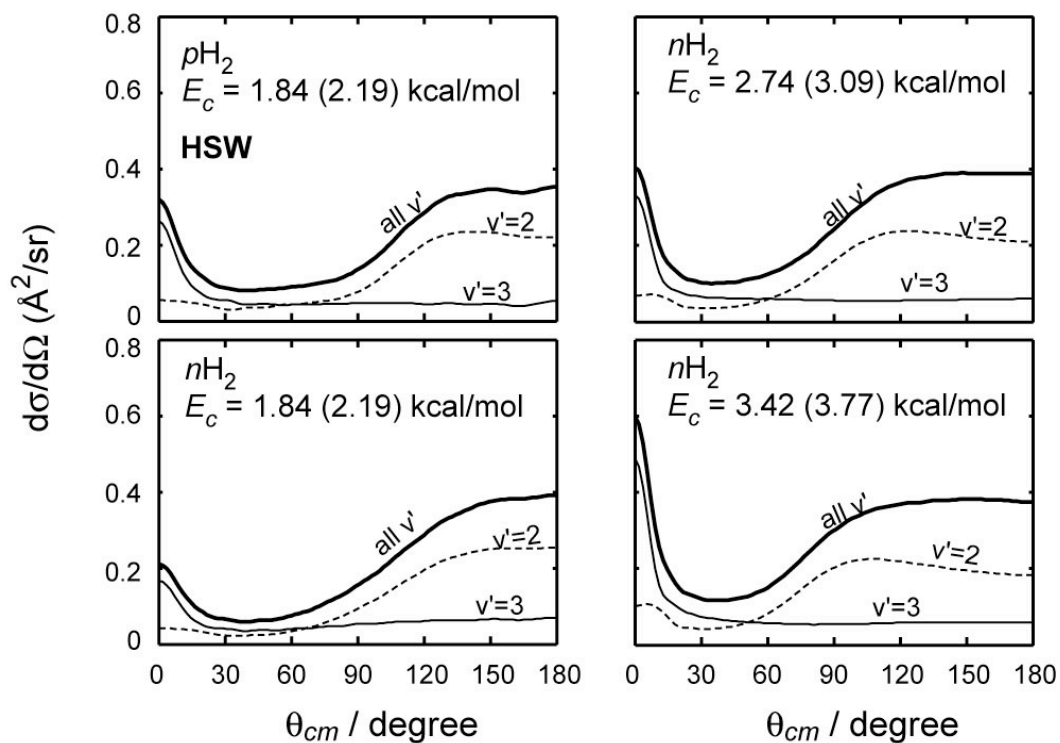
3.4 Results and Discussion

3.4.1 Center-of-Mass Differential Cross Sections

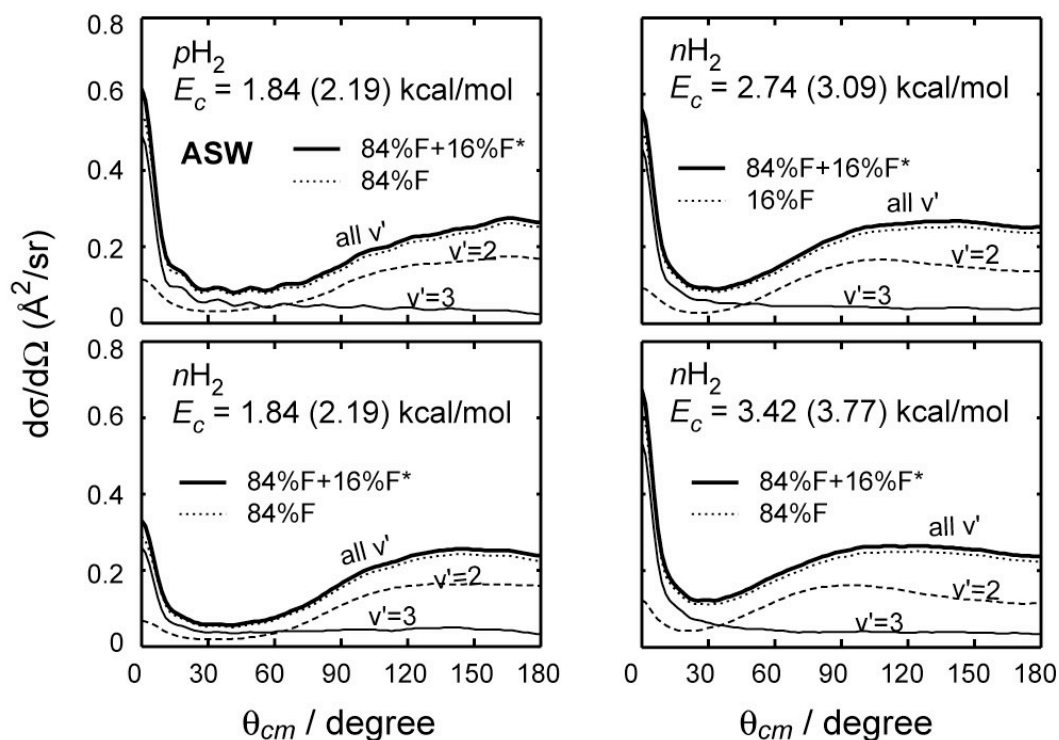
We present here simulations of the experiments¹⁰ involving reactions of F with $p\text{H}_2$ at $E_c = 1.84$ kcal/mol and $n\text{H}_2$ at $E_c = 1.84, 2.74,$ and 3.42 kcal/mol.¹⁰ The vibrationally-resolved DCSs are shown in Fig. 3.1 (for the calculations on the SW PES), Fig. 3.2 (for the calculations on the HSW PES) and Fig. 3.3 (for the calculations on the ASW PESs). For clarity, we show only DCSs for production of the $v'=2$ and 3 products. Although the DCS's for production of $v' = 0$ and 1 show more variations with PES than those for $v'=2$ or 3, the $v' = 0$ and 1 DCSs always give rise to very small ADs, and consequently will not be discussed further here.



Figures 3.1 Center-of-mass differential reactive cross sections calculated on the SW PES.



Figures 3.2 Center-of-mass differential reactive cross sections calculated on the HSW PES. The collision energies in the parentheses indicate the shifted E_c (shifted upward by 0.35 kcal/mol) used in the HSW calculation. We employ this shift to compensate for the overestimation of the activation energy barrier on the *ab initio* Stark-Werner PES.



Figures 3.3 Center-of-mass differential reactive cross sections calculated on the ASW PES. The collision energies in the parentheses indicate the same shift in E_c , as described in Fig. 3.1.

On the basis of comparisons with thermal rate constant measurement, several groups^{24,25} have concluded that, when spin-orbit coupling is properly taken into account, the barrier on the *ab initio* ASW and HSW PESs for the F+H₂ reaction (1.91 kcal/mol)¹ is too high, by 0.3-0.4 kcal/mol. This is consistent with ongoing benchmark *ab initio* calculations,²⁶ aimed at providing guidelines for improvements in the SW and ASW PESs, which are now nearly a decade old. To compensate for the overestimation of the reaction barrier height in the ground electronic state, we have shifted the collision energies for the HSW and ASW calculations upward by 0.35 kcal/mol, as indicated by the values in parentheses in Figs. 3.1 and 3.2.

In Chapter 4, we show that outstanding agreement with the experimental $F+HD \rightarrow FD+H$ reactive excitation function can be obtained by the same shift in the collision energies. We have consistently applied the same shifting in E_c through all of our comparisons between both the HSW and ASW calculations and experiment for the $F+H_2$ and $F+HD$ reactions (justification for this shift in E_c is discussed in Chapter 4.3.3).

Because the ground spin-orbit state of the atom correlates with both a reactive and a non-reactive PESs (Fig. 2.4), in an adiabatic (Born-Oppenheimer) approximation, to zeroth order only 50% of the incoming flux will follow a PES which leads directly to products. However, in a single-state calculation all of the incoming flux will follow the reactive PES. Consequently, we divide the single-state results by a factor of two to compare with the multi-state results (ASW).^{24,56,63}

In Fig. 3.3 (ASW) the short-dashed lines indicate the contribution of the (statistically-weighted) F ground state. Thus the difference between the solid and short-dashed line is the contribution of the (statistically-weighted) spin-orbit excited state (F^*). In general the (statistically-weighted) contribution of F^* is small and is uniformly distributed over all CM scattering angles.

Qualitatively, the simulated SW, HSW and ASW CM DCSs are very similar. Most of the $v'=3$ products are forward scattered while the $v'=2$ products are mainly backward scattered. As the collision energy increases so does the degree of forward scattering of the $v'=3$ products, while the $v'=2$ products show a shift from mainly backward to sideways scattering. These observations agree well with the interpretation by Neumark *et al.* of their beam experiment.¹⁰

3.4.2 DCS ratios

Although the SW, HSW, and ASW results are qualitatively similar, there are noticeable differences. To illustrate these more clearly, we compare in Fig. 3.4 the ratio of the vibrationally resolved HSW vs. SW DCSs. Although Castillo *et al.*¹⁶ have already presented a comparison between the HSW and ASW DCSs, we reproduce here some details which are directly relevant to a comparison of the three (SW, HSW, and ASW) sets of DCSs.

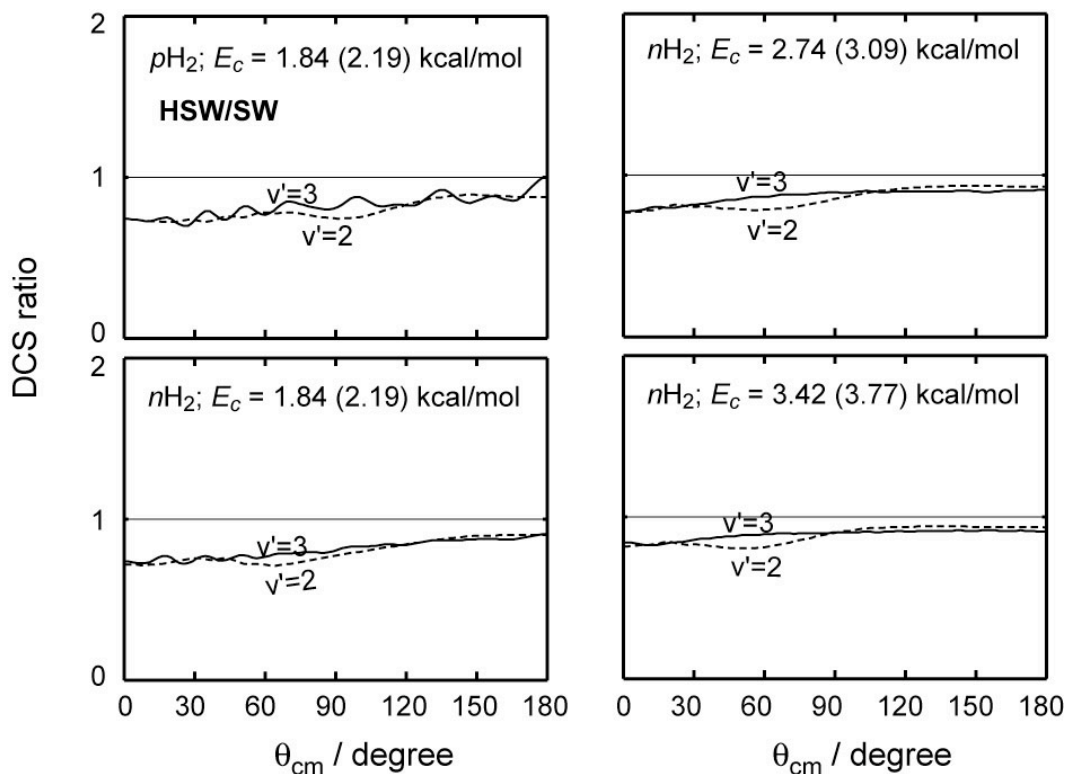


Figure 3.4 Ratios of SW and HSW DCSs. The dashed and solid curves indicate, respectively, cross sections for production of HF products in $v'=2$ and $v'=3$.

The HSW:SW DCS ratios are less than unity over most of the range of CM angles in Fig. 3.4. This indicates that the integral cross sections on the HSW PES will be less than those predicted for the SW PES. As discussed already by other authors,^{12,15,24} the barrier height on the HSW PES is higher because inclusion of the spin-orbit coupling lowers the entrance channel without affecting the transition state. The decrease in the magnitudes of the HSW DCSs is a direct consequence of this increase in the barrier height. This decrease is most pronounced in the forward direction.

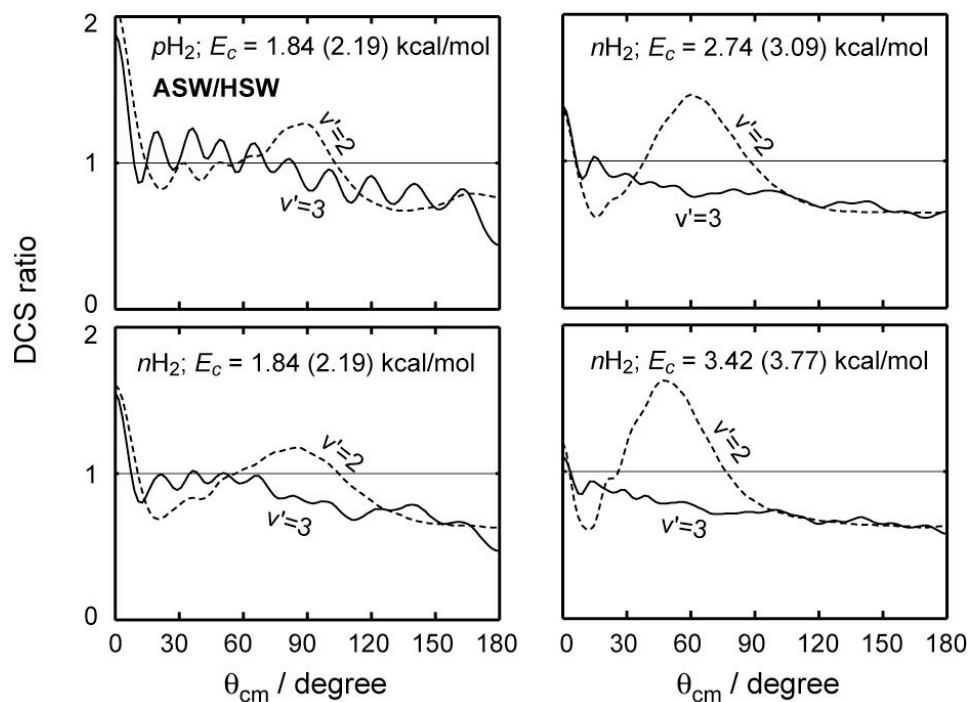


Figure 3.5 Ratios of HSW and ASW DCSs. The dashed and solid curves indicate, respectively, cross sections for production of HF products in $v'=2$ and $v'=3$.

Figure 3.5 presents similar DCS ratios for the HSW *vs.* ASW PESs. The most noticeable feature is that the DCS ratios are consistently smallest in the backward direction. The multi-state calculations on the ASW PESs predict less backward scattering than the single-PES calculations on the HSW PES. For reasons that will become clear later, this reduced backward scattering plays an important role.

If we look in detail at the sideways scattering, especially over the range $30^\circ < \theta_{cm} < 120^\circ$, we observe that, for $v'=2$, relative to the backward scattering amplitude, the ASW:HSW DCS ratio increases as the collision energy increases. At the two higher collision energies (2.74 and 3.42 kcal/mol) and at certain sideways angles, the ASW $v'=2$ DCS becomes larger than the HSW values.

For the $v'=3$ products this sideways scattering enhancement is less apparent. However, we observe that the ASW calculations predict more sideways scattering, relative to the HSW calculations, at the lowest collision energy (1.84 kcal/mol) than at the higher collision energies (2.74 and 3.42 kcal/mol). Overall, again relative to the reduction in backward scattering, the DCS ratios demonstrate enhanced forward and sideways scattering in the ASW calculations, relative to the HSW predictions.

In the discussion below (Sec. 3.4.3) we shall see that this enhancement in sideways scattering considerably improves the comparison with the experimental ADs. Again, with an aim toward the eventual discussion of the ADs, we note that the sideways maximum in the $v'=2$ ASW *vs.* HSW DCS ratios shifts toward smaller scattering angles as the collision energy increases.

One major goal of the present study is the investigation of how the DCSs can shed light on the reactivity of the excited spin-orbit atoms. Since the ASW results in Fig. 3.5 are a weighted sum of DCSs for reaction of both F and F* (with weights given in Chapter 3.3.5), it will be helpful to compare the DCSs predicted by reaction, separately, of each spin-orbit state. This corresponding ratios of the F* *vs.* F DCSs are shown in Fig. 3.6. Here both initial spin-orbit states are given equal weighting.

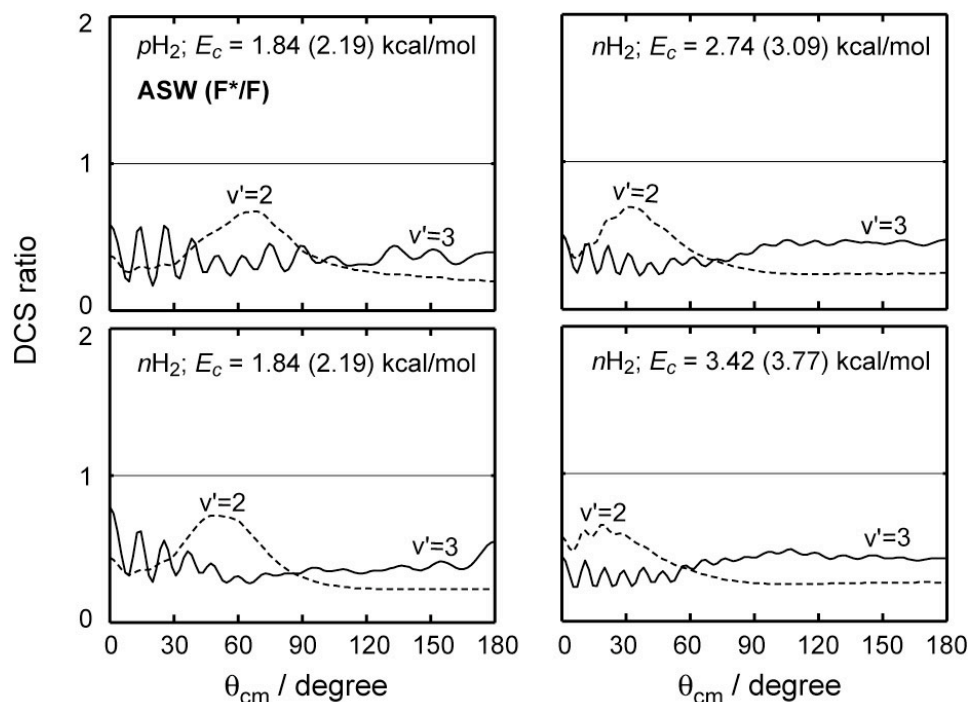


Figure 3.6 Ratios of ASW $F^*(^2P_{1/2})$ and $F(^2P_{3/2})$ DCSs. The dashed and solid curves indicate, respectively, cross sections for production of HF products in $v'=2$ and $v'=3$.

These DCS ratios are quite uniform over the entire range of CM angles. This indicates that the F^* and F DCSs have a very similar angular dependence. This is also apparent in Fig. 3.3, where we plot the DCSs determined with and without the contribution of the F^* state. As can be seen, the shapes are virtually identical in every case. Also we see from Fig. 3.6 that the reactivity of the spin-orbit excited state is $\sim 25\%$ of that of the spin-orbit ground state over the range of energies investigated here.

To a reasonable approximation, if one averages over the oscillatory structure at small angles, for $v'=3$ the $F^*:F$ DCS ratios are approximately 0.25. For $v'=2$ there is a peak in the $F^*:F$ DCS ratio for sideways scattering. However, the amplitude of this peak is smaller and its angular range is narrower than the corresponding $v'=2$

sideways enhancement in the ASW:HSW DCS ratio shown in Fig. 3.5. Since the fractional abundance of F^* in the F atomic beam is only 16%, we can overlook the small sideways modulation in the $F^*:F$ DCS ratio in concluding that for $v'=2$ also the $F^*:F$ DCS ratios are roughly constant.

This uniformity of the F^*/F DCS ratios indicates that, to a very good approximation, and as can be seen in Fig. 3.3, the exact $F^*:F$ population ratio in the F atom beam will only scale the DCS, without affecting its overall shape. In other words, even with all of the F atoms in the ground spin-orbit state, the ASW:HSW DCS ratios would be qualitatively the same as what is shown in Fig. 3.5. However, the HSW PES is identical to the lowest ASW adiabatic eigenvector. Consequently, we conclude that the relative sideways ($v'=2$) and forward ($v'=3$) enhancements in the ASW:HSW DCSs reflect significant non-adiabatic effects, due to the couplings between the various electronic-spin-rotational states which are absent in the HSW calculations, and which are independent of the exact ratio of ground and excited spin-orbit atoms in the beam.

Once we recognize that the exact fraction of F^* has a limited effect on the shape of the DCS, we can simplify our analysis of the dynamics by assuming that all the F atoms are in the spin-orbit ground state. From comparison of rotational state resolved DCSs (not shown here), we discover that the features seen in Fig. 3.5 arise, partially from variations in the forward scattering over a wide range of j' states, partially from shifts from backward toward sideways scattering for intermediate HF rotational states, and partially from the quenching of higher HF rotational states over a large range of scattering angles.

Because of the large difference in the reaction barrier,¹ we think it less instructive to compare the SW and ASW DCSs. Notwithstanding, it is interesting to recognize that the HSW calculations yield less forward scattering than the SW calculations (Fig. 3.4). In contrast the HSF calculations predict more backward

scattering than the ASW calculations (Fig. 3.5). The consequence of these two effects is that the SW and ASW DCSs are very similar in shape. Subsequently, as will be seen in the next subsection, the SW and ASW ADs are also very similar in shape.

3.4.3 Laboratory Angular Distributions

The simulation of the ADs is carried out by Monte-Carlo integration of Eq. (2) in Ref. 14 using the program developed by Aoiz and co-workers.⁶¹ To compare with experiment, the simulated ADs are further rescaled by an angle and energy independent scaling factor,¹⁴ determined from another program kindly lent us by Aoiz and co-workers. In Ref. 14 this scaling factor was determined by minimizing the deviation between the simulated and experimental distributions over all laboratory scattering angles.

Here, in contrast, we deliberately exclude small LAB angles in the determination of this scaling factor. For $0 \leq \Theta_{lab} < 12^\circ$ the major contribution to the ADs arises from $v'=3$ products, forward scattered in the center-of-mass. Castillo *et al.*¹¹ attributed this forward scattering to quantum mechanical tunneling.¹¹ As mentioned earlier in Section 3.4.1, it is likely that the barrier on the HSW and ASW PESs is too high by 0.3–0.4 kcal/mol.²⁴⁻²⁶ In addition, the *ab initio* calculations on which the HSW and ASW PESs are based predict too small a value of the reaction exoergicity (-31.34 kcal/mol¹² as compared to the experimental value of -32.0 kcal/mol⁶⁴). Because tunneling probabilities will be very sensitive to errors in the barrier height and the overall energetics, we thought it best not to include small-angle scattering in the LAB frame in the determination of the overall scaling of experiment relative to the theoretical simulation.

In addition, for small angle scattering in the LAB frame the angle between the laboratory velocity vector of the HF products and the initial relative velocity vector

[the intersection angle ξ_q in Eq. (2) of Ref. 14, or equivalently, the intersection angle ζ_q in Eq. (2.78) of Chapter 2.2.2] for HF($v'=3$) scattering in the forward direction is near $\pi/2$. In this range of intersection angles small inaccuracies in the theoretical simulation can be substantially amplified in the CM \rightarrow LAB transformation, because of the presence of the factor $1/|\cos\xi_q|$ in this transformation.^{14,53}

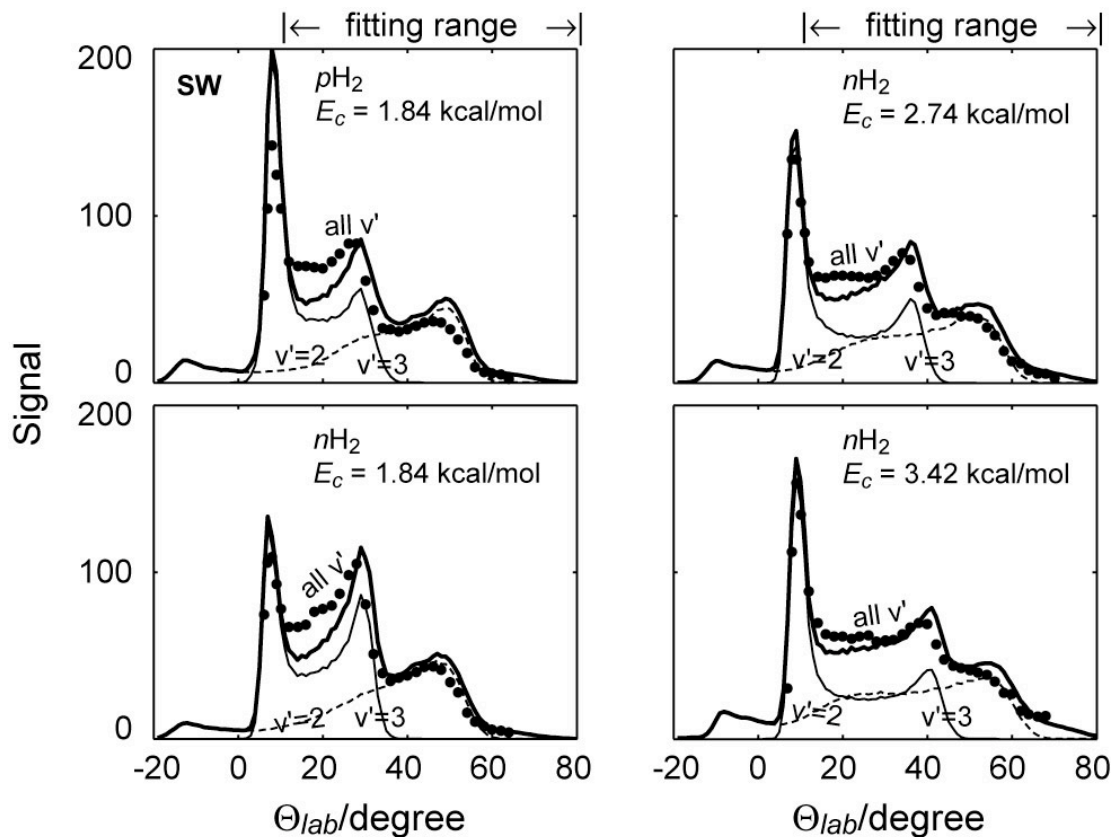


Figure 3.7 Comparison of SW and experimental LAB ADs. As indicated, the fitting is performed only in the LAB angle range $12^\circ < \Theta_{lab} < 80^\circ$.

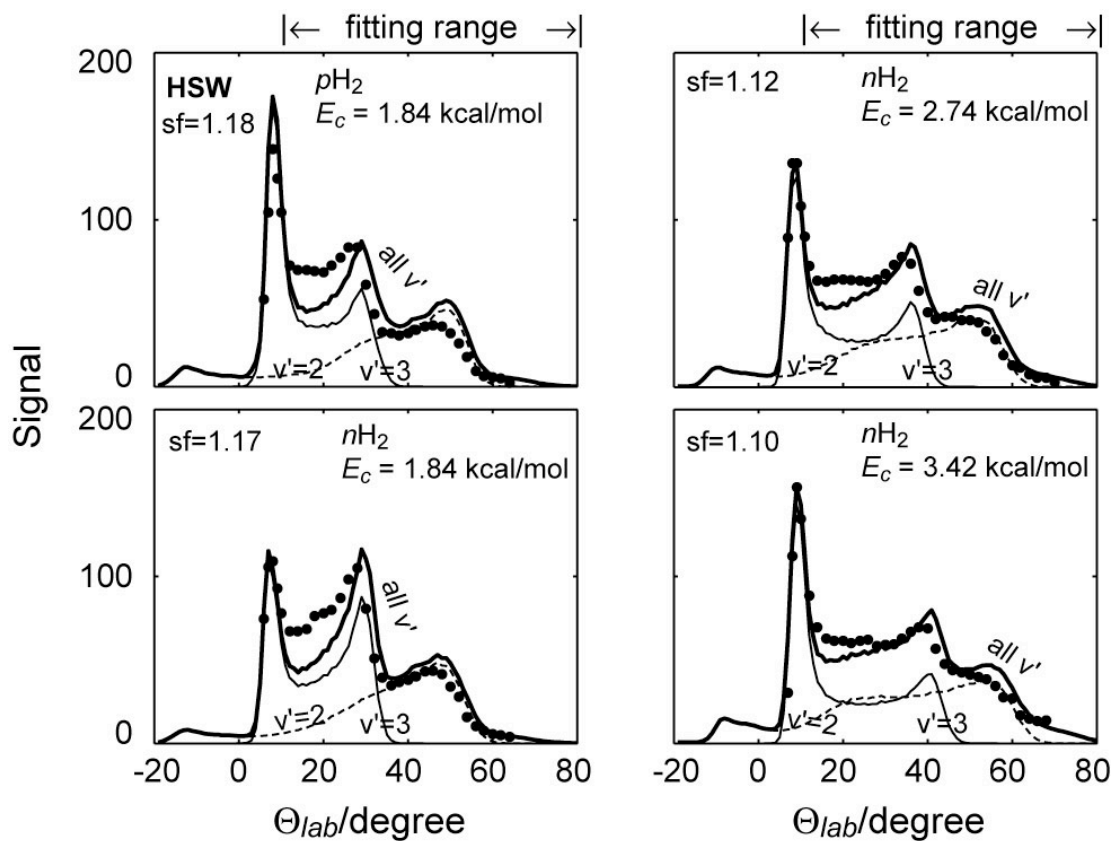


Figure 3.8 Comparison of HSW and experimental LAB ADs. As indicated, the fitting is performed only in the LAB angle range $12^\circ < \Theta_{\text{lab}} < 80^\circ$. The scaling factor for the experimental/theoretical comparison, relative to that for the SW simulations at the upward shifted (+0.35 kcal/mol) energy and for the same H₂ isotopomer, is designated by “sf”.

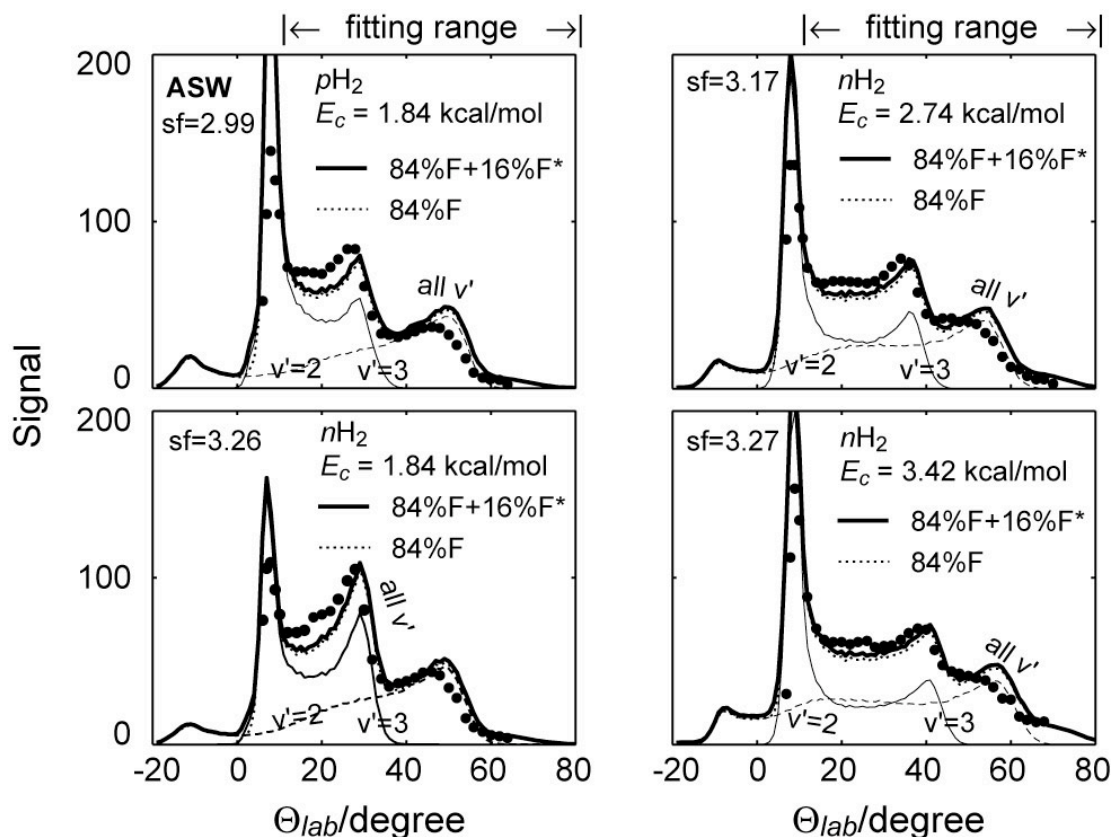


Figure 3.9 Comparison of ASW and experimental LAB ADs. As indicated, the fitting is performed only in the LAB angle range $12^\circ < \Theta_{lab} < 80^\circ$. The scaling factor for the experimental/theoretical comparison, relative to that for the SW simulations at the upward shifted (+0.35 kcal/mol) energy and for the same H₂ isotopomer, is designated by “sf”. The short dash lines indicate the ADs which would be predicted without taking into account the F* atoms in the incoming beam.

For all these reasons we restrict the range of LAB angles to $12^\circ \leq \Theta_{lab} \leq 80^\circ$ in determining the overall scaling factor. Scaling factors were determined, separately for the SW, HSW, and ASW simulations. The resulting ADs are shown in Figs. 3.7-3.9, for, respectively, the SW, HSW, and ASW simulations. For comparison and the purposes of discussion, we re-normalize these three scaling factors to the scaling

factor for the SW PES.¹⁴ The resulting relative scaling factors for the HSW and ASW simulations are displayed in Figs. 3.8 and 3.9.

In Fig. 3.9 (ASW AD simulations) we show the contributions from the weighted F and F* reactions (with relative weights 0.84 and 0.16) and, separately, the contribution from just the ground-spin orbit state (weighted by 0.84). From purely statistical arguments, as discussed earlier, we would expect the reactive cross sections from the ASW simulations would be 50% of that from the HSW simulations, since 50% of the flux would be associated with the nonreactive $^2\Pi_{3/2}$ PES (Fig. 2.4). However, the actual optimum scaling factor for the ASW simulations is more than twice that for the HSW simulations. Because of the variability in these scaling factors, although the HSW and ASW DCSs are quite different in the backward direction in the CM frame ($120^\circ < \theta_{cm} < 180^\circ$) (Fig. 3.5), the predicted HSW and ASW ADs now have a similar behavior in the LAB angle range $30^\circ < \Theta_{lab} < 80^\circ$.

Overall, in the range of angles used in our fit to experiment, the ASW ADs reveal enhanced sideways and reduced backward scattering when compared with the HSW ADs, and look very similar to the SW ADs, as was anticipated in the preceding section. At the two higher collision energies (2.74 and 3.42 kcal/mol) and in the range of fitted angles, the ASW ADs agree very well with experiment, but slightly overestimate the $v'=3$ forward and the $v'=2$ backward scattering.

The major motivation for our investigation was the determination of how the reactivity of spin-orbit excited F atoms is reflected in the LAB angular distribution of the HF $v'=3$ product, especially for angles Θ_{lab} near 20° where simulations based on previous single PES calculations disagree with experiment (Figs. 3.7 and 3.8). Because the DCSs for reaction of F($^2P_{3/2}$) and F*($^2P_{1/2}$) have a very similar angular dependence (Fig. 3.6), we see that the presence of F* in the beam affects mainly the overall magnitude without changing the shape of the ADs. Thus the underestimation of sideways scattering in the single-state simulations cannot be explained by a lack of

consideration of the reactivity of the F* atoms in the beam. Equivalently, this means we would obtain similar ADs even under the assumption that all of the F atoms are in the ground spin-orbit ($^2P_{3/2}$) state, as shown in Fig. 3.10.

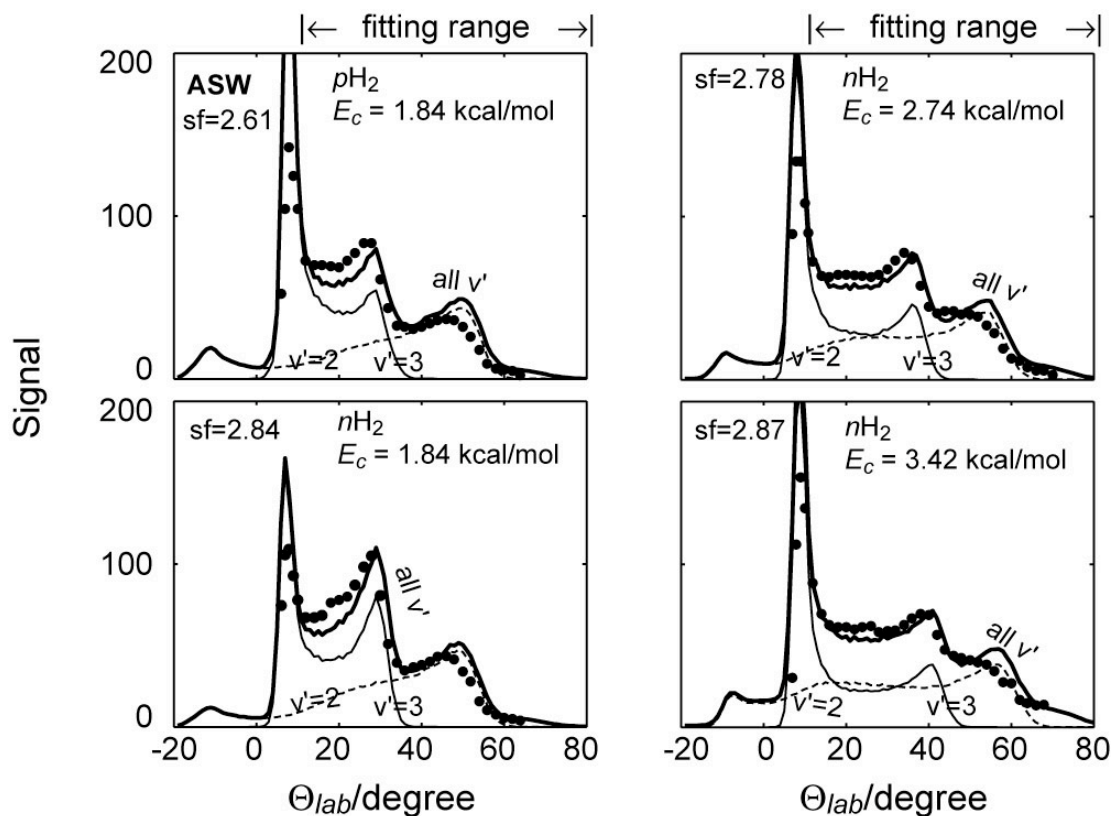


Figure 3.10 Comparison of ASW and experimental LAB ADs, with the assumption that all the F atoms are initially in the ground ($^2P_{3/2}$) spin-orbit state. As indicated, the fitting is performed only in the LAB angle range $12^\circ < \Theta_{lab} < 80^\circ$. The scaling factor for the experimental/theoretical comparison, relative to that for the SW simulations at the same energy and for the same H_2 isotopomer, is designated by “sf”.

3.5 Conclusions

In this Chapter we have presented the quantum mechanical study of center-of-mass differential cross sections and laboratory-frame angular distributions for the F+H₂ reaction on the SW, HSW, and ASW PESs for the four different combinations of collision energy and hydrogen isotopomer investigated in the experiments of Neumark *et al.*¹⁰ Our simulations show that non-adiabatic coupling greatly reduces backward scattering, an effect which Suits called “the shadow of the conical intersection.”⁶⁵ Since backward scattering corresponds to collisions at small impact parameter, in future work, it would be worthwhile to investigate whether there is an associated increase in inelastic scattering at small impact parameters. Also, surprisingly, we find the shapes of both the DCSs and ADs are insensitive to the fraction of F* presented in the F beam.

The reduced backward scattering leads to enhanced forward and sideways scattering. As a consequence, at the two higher collision energies (2.74 and 3.42 kcal/mol), the enhanced sideways scattering bring the ASW ADs to an almost perfect match with experiment over the range $12^\circ < \Theta_{lab} < 80^\circ$. At these energies the major discrepancy is associated with the $v'=3$ forward peaks. Similarly at the lowest collision energy (1.84 kcal/mol), it is the scattering of HF products in $v'=3$ which makes the dominant contribution to the ADs in the sideways direction. Due to the substantial exothermicity error in the *ab initio* calculations on which all the Stark-Werner PESs (SW, HSW, and ASW) are based,²⁶ the $v'=3$ products will have significantly less translational energy in the simulations than in reality. This difference will be relatively more important at lower collision energies. Consequently, we might expect that the simulated ADs will be less accurate at the lower collision energies, which is what is observed in Figs. 3.8-3.10.

Because of the great interest in, and the fundamental importance of, the F+H₂ reaction, it would certainly be worthwhile to develop a better set of global PESs

which would correct, at least partially, the errors in the barrier height and exothermicity of the ASW and HSW PESs.

4 The F+HD Reaction: Product Excitation

Functions

4.1 Introduction

Over the past several years and in Chapter 3, we have presented a number of fully-quantum scattering studies of the reaction of F with H₂.^{1,8} We use quantum-mechanical time-independent scattering calculations to investigate how the open-shell character of the F(²P) atom effect the F+H₂ reaction. These calculations involve multiple potential energy surfaces (the Alexander-Stark-Werner, ASW, PESs),¹ and include an accurate treatment of the couplings (non-adiabatic, spin-orbit, and Coriolis) among all three electronic states.¹ The importance and role of the open-shell character of halogen atoms in reactions with molecular hydrogen has been the object of substantial recent theoretical interest.^{1,6,8,17,24,55,58,66,67}

One major goal of our investigation is to determine whether multi-electronic-state calculations which include reaction spin-orbit excited state [F*(²P_{1/2})] can resolve the remaining discrepancies⁶⁸ between experiment and earlier, single-electronic-state calculations based on the lowest electronically adiabatic PES, the Stark-Werner (SW) PES.^{16,23}

In Chapter 3, we reported center-of-mass differential cross sections (DCSs) and laboratory-frame angular distributions (ADs) for the F+H₂ reaction. Since the difference between experiment and earlier, single-state simulations was largest in the sideways direction, our goal was to explore how inclusion of the spin-orbit excited state would affect the sideways scattering. We found that the presence of non-adiabatic couplings effectively reduces the backward scattering of HF products.¹⁹ Consequently, the three-state calculations resulted in an increase in the simulated ADs in the sideways direction, in better agreement with experiment.

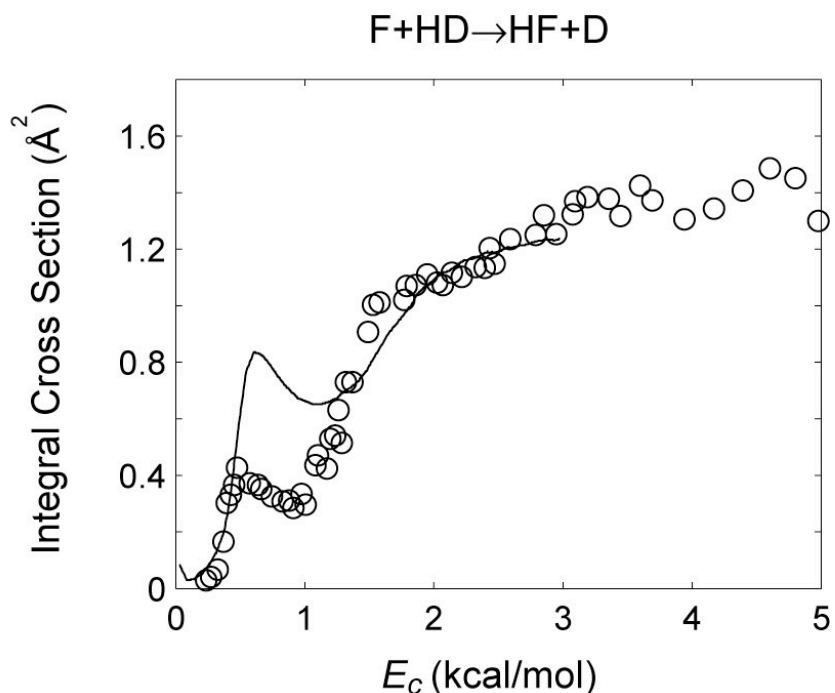


Figure 4.1 Plot of the energy dependence of the total $F+HD \rightarrow HF+D$ reactive cross section, taken from Fig. 3 of Ref. 16. The experimental data by Liu and co-workers are indicated by open circles while the theoretical simulations (solid line) are based on single-state calculations on the SW PES.

Unfortunately, because the $F+H_2$ and F^*+H_2 DCSs are very similar in shape, and because the center-of-mass to laboratory transformation involves rescaling, the predicted ADs are nearly independent of the F^* population in the beam. As a result, comparison of simulated and experimental ADs does not in of itself provide unambiguous evidence of the importance of the F^* reaction.

As an additional probe of the importance of non-adiabatic dynamics we turn our attention to the $F+HD$ reaction. For this reaction there remain important differences in the excitation function (relative reaction cross sections) for the HF product channel between experiment^{22,23} and the predictions of single-electronic-state calculations based on the SW PES.²³ As shown in Fig. 4.1, the most noticeable

is the overestimation of the height of the dynamic resonance peak at collision energies of ~ 0.5 kcal/mol.^{5,22,23}

The F+HD reaction has a barrier height of $E_b \sim 1.92$ kcal/mol.¹ Consequently, reaction at collision energies less than ~ 1.0 kcal/mol certainly involves tunneling.^{5,22} Tunneling probabilities depends on the height of the barrier. Inclusion of the spin-orbit Hamiltonian effectively increases the F+H₂ barrier height by 1/3 of the F spin-orbit splitting ($404 \text{ cm}^{-1} = 1.16 \text{ kcal/mol}$ ⁴⁷).^{1,12,15} Thus, any feature which is sensitive to tunneling will be significantly affected by addition of the F spin-orbit coupling to the single-state calculations.

In addition, since the F*+HD reactant asymptote correlates adiabatically with a repulsive PES ($^2\Pi_{1/2}$ in linear geometry),¹ reaction of the spin-orbit excited atom will occur through indirect coupling to the reactive PES. Consequently, the F* reaction may give rise to a quite different resonance feature, or none at all. Thus, the relative F: F* population in the incoming beam may dramatically change the shape and height of the resonance peak.

In addition to the discrepancy between experiment and earlier calculations of the height of the resonance peak, another noticeable discrepancy is a small rise in the experimental excitation function in the energy range between 1.5 and 2.0 kcal/mol.²³ This rise occurs because the formation of the HF($v'=3$) products from reaction of the F ground state shows a sudden increase, when sufficient energy ($E_c > 1.32$ kcal/mol) is present to overcome the slight endoergicity of the $v'=3$ products.²³ The same phenomenon was not observed in the single-state theoretical calculations.

The F* reaction could contribute here. First, as mentioned above, the presence of the spin-orbit Hamiltonian lowers the F+HD energy, but only in the reactant region.^{1,12} This effectively increases the reaction barrier, which will act to reduce the overall reaction probability. However, lowering the entrance asymptote will also increase the threshold for the formation of HF products in $v'=3$, and therefore delay to

higher energy the contribution of $v'=3$ to the excitation function shown in Fig. 2.4. On the other hand, because of the additional 1.16 kcal/mol of internal energy in the F^* reactants at collision energies below 2 kcal/mol HF products in $v'=3$ can be formed by the F^*+HD reaction.

The goal of this Chapter is to use quantum reactive-scattering calculations with full inclusion of the open-shell character of the F atom to investigate how the spin-orbit excited reaction and/or non-adiabatic effects affect the predicted excitation functions for the F+HD reaction. The rest of this Chapter is organized as follows: Section 4.2 contains a brief review of the theoretical methods used. In Section 4.3, we present the calculated excitation functions of the HF and DF products. By making direct comparisons with experiment data, we examine in detail the role of F^* in the F+HD reaction. A conclusion follows.

4.2 Method

4.2.1 Details of the scattering calculations

The exact quantum description of the reaction of F+HD follows the formalism presented earlier by Alexander, Manolopoulos and Werner.¹ A full description requires three potential energy surfaces (PESs) and an accurate description of the couplings (non-adiabatic, spin-orbit, and Coriolis) among them. We refer the interested reader to Ref. 1, and will reiterate here only those details directly relevant to the present investigation.

The scattering calculations yield the scattering S matrix, in terms of which integral reactive cross sections σ can be determined as:^{33,44}

$$\sigma_{j_a v_j \rightarrow v' j'}(E_{col}) = \frac{\pi}{(2j+1)(2j_a+1)k_{j_a v_j}^2} \sum_{J, k_a, k, k', \sigma_h} (2J+1) \left| S_{j_a k_a v_j k \rightarrow v' j' k' \sigma_h}^J(E) \right|^2. \quad (4.1)$$

Here, the initial (F+HD) states are labeled by the value of the electronic angular momentum of the atom ($j_a = 3/2$ for F and $j_a = 1/2$ for F*), the projection of j_a , the vibrational, rotational, and projection quantum numbers of the diatomic moiety. The primes indicate the corresponding quantities for the product arrangement (FH+D or FD+H) in addition to the spin projection quantum number (σ_h) of the H (D) product. Because the experiments neither select nor resolve the projection quantum numbers, these are added (for the product quantum numbers) and averaged (for the reactant quantum numbers). Here J is the total angular momentum of the system, E is the total energy, and E_{col} is the collision energy for reactants HD(v,j)+F(j_a), so

$$E_{col} = E - \varepsilon_{j_a} - e_{vj}, \quad (4.2)$$

where ε_{j_a} is the energy of the particular spin-orbit state of the F atom, and e_{vj} is the vibration-rotation energy of the HD molecule. Also, the wavevector in Eq. (4.1) is given by $k_{j_a v j}^2 = 2\mu E_{col}$, where μ is the F–HD reduced mass.

Table 4.1 lists the parameters used to define the scattering calculations in Chapters 4 and 5.

TABLE 4.1 Summary of parameters used in the present F+HD scattering calculations.

J^a	j_{max}^a	$K_{max}^{a,b}$	$E_{max}(\text{eV})^a$	$\rho_{max}(\text{bohr})^a$	N_s^a
0.5-30.5	15	3.5	1.3	12	100

a. See the definition in caption *a* of Table 3.1.

b. See Caption *b* in Table 3.1.

Table 4.2 Range of collision energies included in the present F(j_a)+HD(v,j) calculations.

j_a	j	$\max(E_{col})^a$	$\max(E_{col})^b$
3/2	0	4.424	4.074
3/2	1	4.169	3.819
1/2	0	3.288	2.938
1/2	1	3.033	2.683

- a. Maximum collision energy attained in the scattering calculations.
b. Collision energy limit in the simulations. Column 4 = Column 3 – 0.35 kcal/mol.

4.2.2 Comparison with experimental data

Because of the relation between the total energy E and the initial relative translational energy $E_{j_a v j}$ [Eq. (4.2)], the simulation of an “experimental” cross section at a particular initial translational (collision) energy necessitates scattering calculations at a large number of different total energies. In actual practice, cross sections were determined at 156 total energies spanning the range 5.063 – 9.465 kcal/mol. The corresponding maximum collision energies sampled in the calculations are enumerated in Table 4.2. The largest of the scattering calculations included 2440 coupled channels.

Both F* and F are present in the initial molecular beam, as well as a distribution of HD rotational states. The experiments of Liu and co-workers^{5,22,23} measure the following averaged integral cross sections for formation of HF (or HD) products:

$$\sigma(E_{col}) = \sum_{j_a v j} w_{j_a} p_{v j} \sigma_{j_a v j \rightarrow v' j'}(E_{col}), \quad (4.3)$$

where w_{j_a} and $p_{v j}$ are, respectively, the relative populations in the initial beams of the atomic spin-orbit states and molecular vibration-rotation states. In our calculations we chose w_{j_a} to be given by a Boltzmann distribution at the temperature

of 600K, which characterizes the F atom velocity in the atom source used by Liu and co-workers,²³ so that $w_{F^*}=0.16$ and $w_F=0.84$.⁶⁹ We further assume that only the HD $v=0$ vibrational level is populated, and, further, that the molecule is confined to its two lowest rotational levels, with $p_{j=0}=0.82$ and $p_{j=1}=0.18$ at a rotational temperature of 50K.²³

The experiments reported in Ref. 23 determine only relative cross sections, which we designate “excitation functions.” The magnitude of the data shown in Ref. 23 was adjusted to fit simulations based on the SW PES. For comparison with our multi-state calculations, we choose to renormalize the experimental data, which are, after all, only relative quantities, by multiplication by an overall constant scaling factor. This we determine by a least-squares fit to our calculations for the DF product channel. This choice is based on the observation that the calculated excitation function for DF products agrees extremely well with experiment as will be discussed in section 4.3.1. This fit yields a scaling factor of 0.78. To be consistent with the normalization procedure used in the analysis of the experiment,²³ we use an identical scaling factor for both the DF and HF product channels.

In the discussion below we will also distinguish between integral cross sections for reaction of $F(^2P_{3/2})$ and $F(^2P_{1/2})$. To do so, rather than use Eq. (4.3), we average the integral reactive cross sections σ only over the rotational states of the HD molecules,

$$\sigma(E_{col}; j_a) = \sum_{vj} p_{vj} \sigma_{vj \rightarrow v'j'}(E_{col}; j_a). \quad (4.4)$$

Integral cross sections obtained in this way represent the full effect of each spin-orbit state separately. To obtain integral cross sections that take into account the relative populations of F and F* in the beam, we must then multiply Eq. (4.4) by the population of the F spin-orbit states w_{j_a} , which yields Eq. (4.3).

4.2.3 Comparison with calculations on SW PES

To better understand the differences between the calculations on the (multi-state) ASW and (single-state) SW PES, we will also compare our calculations with the excitation functions calculated for the SW PES.^{22,23} Since the SW PES is a fit to just the lowest electronically adiabatic state, the calculations reported in Ref. 22 effectively assume zero F* reactivity. Under this assumption, to zeroth order one can correct for the electronic degeneracy of the $F(^2P_{3/2})+HD$ reactant asymptote by dividing the calculated SW cross sections by a multiple PES factor of 2.²³

In general, because the reactivity of F* is small, this simple renormalization gives a good estimate of the absolute integral cross section. Nevertheless, in a detailed comparison with cross sections which are determined on multiple PESs and which are averaged over the population of F spin-orbit states, this division by 2 will always yield higher values, except when the F* reactivity is larger than the F ground state, which only occurs at very low collision energies. Since we have renormalized the experimental data from Ref. 23 to fit the results of our multi-state calculations, and since the published experimental data were themselves normalized to fit the original SW calculations,²² we will need to renormalize the SW excitation functions by multiplying by the same scaling factor (0.78) used to renormalize the experimental data. Further, we use the identical scaling factor to rescale the SW calculations and experiment in Ref. 23 for both the DF and HF product channels. This will preserve the quality of the original fit of the experiment to the SW calculations.

4.3 Results and Discussions

We begin by making a distinction between reactions of the F ground [$F(^2P_{3/2})$] and spin-orbit excited [$F(^2P_{1/2})$ or F*] states. The F reaction can occur on the lowest electronically adiabatic PES, which directly correlates the reactants in their electronic ground state with HF (or DF) products in their electronic ground state

($^1\Sigma^+$).¹ The F* reaction is adiabatically forbidden, because the excited spin-orbit state correlates adiabatically only to HF (or DF) products in their first excited electronic ground state ($^3\Pi$),¹ which is quite high in energy and therefore inaccessible for reactions at moderate collision energies.^{57,70} Reaction of F* is enabled by non-adiabatic couplings between the ground and excited electronic states. In the discussion that follows, we will make repeated reference to these two mechanisms. To keep the text concise, we will designate the two spin-orbit states, and the corresponding cross sections, by just F and F*. We will use the full (2P_j) description only when necessary.

4.3.1 F+HD \rightarrow DF+H

Using Eq. (4.3), we obtain the calculated energy dependence of the integral reactive cross section $\sigma(E_c)$ for the DF channel which is shown in the upper panel of Fig. 4.2. The thick solid line depicts the total contributions from reaction of F and F*, and the two thin lines depict the contributions of F and F*, separately. To compensate for the overestimation in the *ab initio* calculations of the reaction barrier height in the ground electronic state,²⁴⁻²⁶ we have shifted collision energy abscissa for the ASW cross sections upward by 0.35 kcal/mol. Justification of this shift is discussed in more detail below in subsection 4.3.3. We also compare our calculations with experiment²³ (open circles) and the earlier single-state calculations²² based on the SW PES (filled circles) which were taken directly from Ref. 22 and then renormalized as described above.

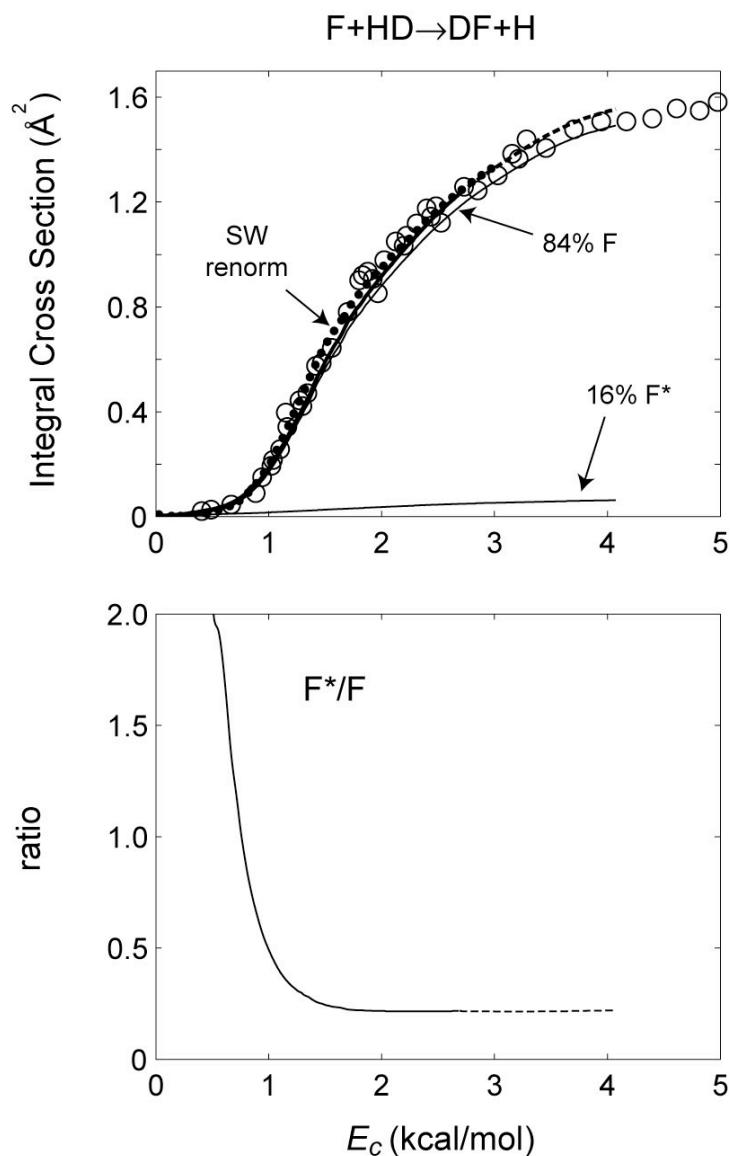


Figure 4.2 (Upper panel) Plot of the energy dependence of the total $F+HD \rightarrow DF+H$ reactive cross section. The renormalized experimental data by Liu and co-workers (Ref. 23) are indicated by open circles. The theoretical simulations based on the three-state ASW calculations are indicated by the heavy solid line. The renormalized single-state SW calculations (solid dots) are indicated, as well as the separate contribution for the ground (F) and excited-state (F*) reactions. (Lower panel) Ratio of the total cross sections for reaction of the ground and excited spin-orbit states, predicted by the multi-state ASW calculations, as a function of energy.

Because of the finite range of total energies spanned in our scattering calculations, determination of the cross sections for the F* reaction are possible only for $E_c \leq 2.68$ kcal/mol (see Table 4.2). Because of the higher internal energy of the F* reactant, at a given total energy the collision energy is larger for F atoms in their ground spin-orbit state. Consequently, the range of total energies spanned in the scattering calculations allows determination of cross sections for the adiabatically-allowed ground-state reaction up to collision energies of 3.82 kcal/mol. We can compare the total cross sections at collision energies between 2.68 and 3.82 kcal/mol only by extrapolating the F*+HD cross sections,⁷¹ which make a small contribution to the total, and then add these to the exact F+HD cross sections. The results of this extrapolation are indicated by thick dashed lines in Fig. 4.2.

Figure 4.2 reveals that both the (multiple-PES) ASW and (single-PES) SW calculations agree perfectly with experiment for the DF excitation function. Because substantial (16%) fraction of the ASW results are due to F* reactivity, the close resemblance of the ASW DF excitation function with the renormalized SW result suggests that, except at low collision energies, the F*+HD \rightarrow DF+H reaction does not make a significant contribution, as observed in our study of the F+H₂ reaction in Chapter 3.

We can use Eq. (4.4) to determine the separate F and F* integral cross sections. The ratios, $\sigma(E_c; j_a=1/2)/\sigma(E_c; j_a=3/2)$, are plotted in the lower panel of Fig. 4.2. We see that the reactivity of F* is relatively small and nearly constant (~25%) for collision energies above 1 kcal/mol. It is not until $E_c < 0.8$ kcal/mol that the F* reactivity dominates. We note that because of the small population of F* in the beam, the effective contribution of the F* reaction under the conditions of the experiment is only 4 % of the total.

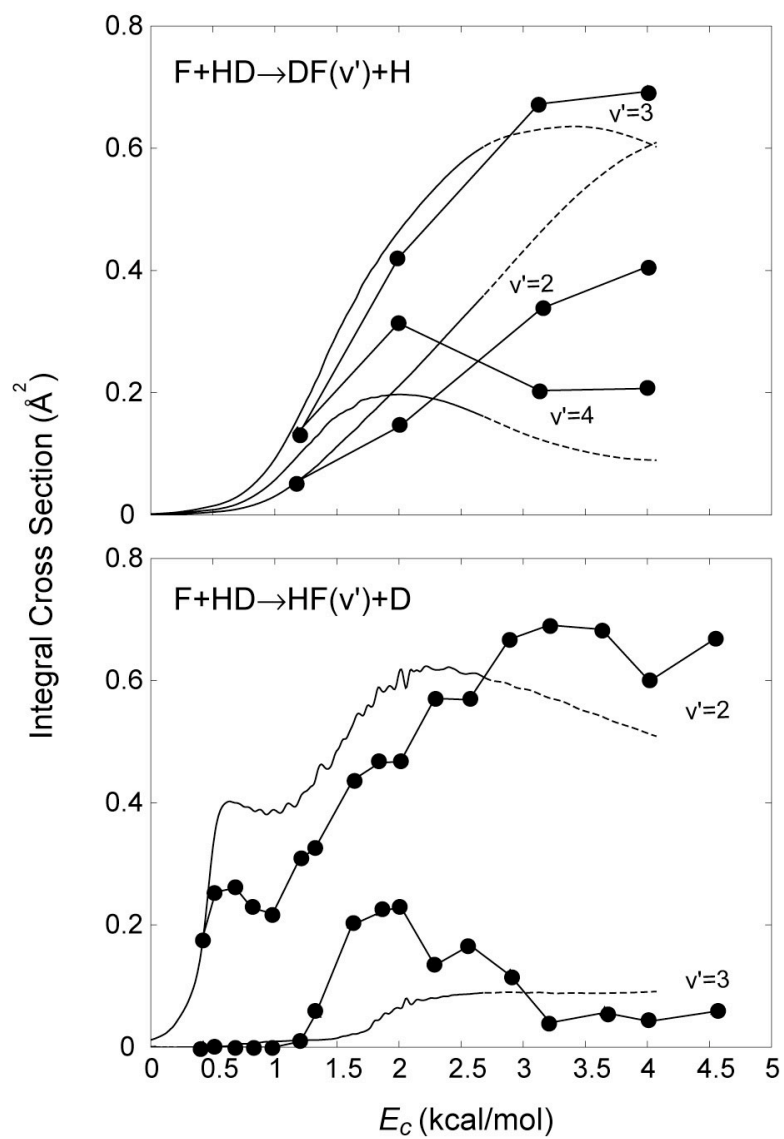


Figure 4.3 (Upper panel) Plot of the energy dependence of the $F+HD \rightarrow DF+H$ reactive cross sections, for DF products formed in $v'=2, 3$, and 4 . The renormalized experimental data by Liu and co-workers (Ref. 23) are indicated by filled circles. The theoretical simulations based on the three-state ASW calculations are indicated by the solid lines. The dashed components indicate the energy range over which the F^* reactive cross sections were extrapolated. (Lower panel) Similar plot but for the $F+HD \rightarrow HF+D$ product channel.

In the upper panel of Fig. 4.3, we plot the excitation functions for each final DF vibrational manifold and compare these to experiment. Given the excellent agreement of the total excitation functions, summed over product vibrational level (Fig. 4.2), we were surprised to find that significant discrepancies exist for DF products in $v'=2$ and 4. Analysis shows that the underestimation, in the theoretical simulation, of product flux in the higher rotational states of DF products in $v'=3$ and 4 is compensated by an overestimation of product flux in $v'=2$ and 1 (not shown in Fig. 4.3). As a result, the excitation function, totaled over all vibrational states, agrees very well with experiment.

4.3.2 F+HD→HF+D

Again, to be consistent with the normalization done in the analysis of the experiment,²³ we used an identical scaling procedure for both the HF and DF product channels. The HF excitation functions and reactivity ratios are shown in Fig. 4.4. The labeling is identical to Fig. 4.2. The corresponding vibrational-state-specific excitation functions are shown in the lower panel of Fig. 4.3.

In the upper panel of Fig. 4.4 we see that both the ASW and SW calculations disagree with experiment in two aspects: One is the overestimate of the resonance peak^{22,23} near $E_c = 0.5$ kcal/mol, and the other is the underestimation of the excitation function in the collision energy range 1.5–2.0 kcal/mol. Compared to the renormalized SW results, the ASW calculation predicts a smaller intensity for the resonance peak. This reduction comes from the effect of the increased barrier height of the ground electronic state which is a consequence of the inclusion of the spin-orbit Hamiltonian, as discussed in the Introduction.

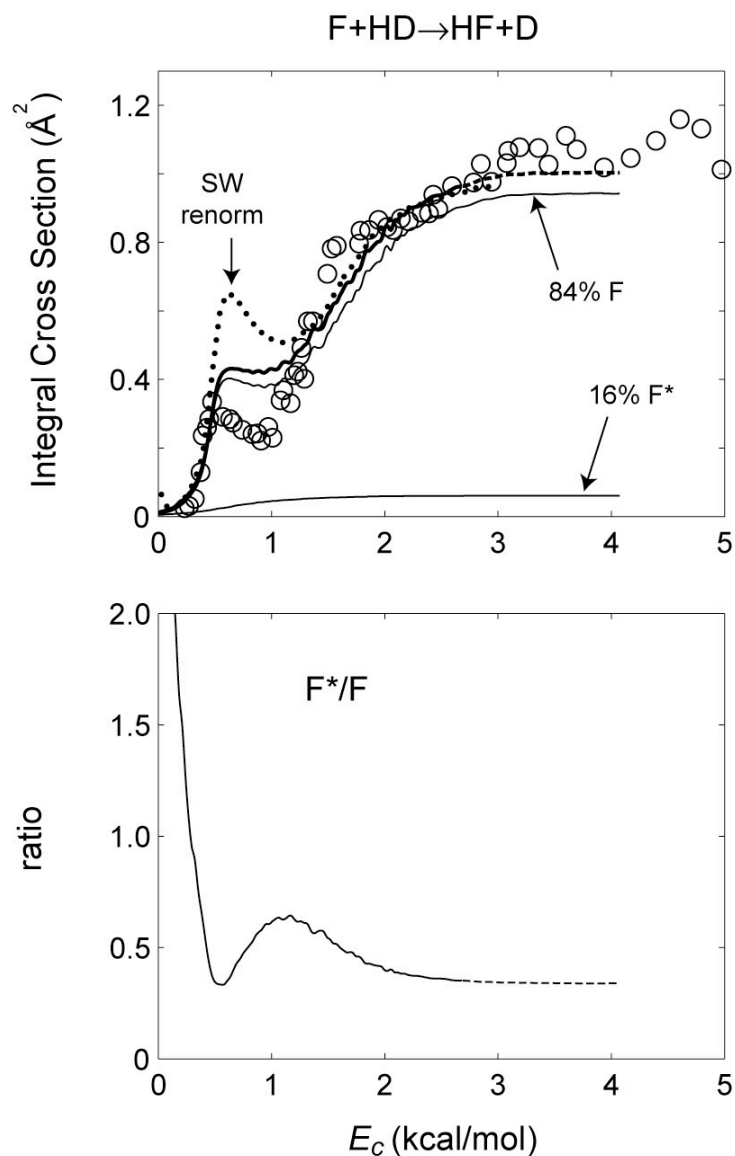


Figure 4.4 (Upper panel) Plot of the energy dependence of the total $F+HD \rightarrow HF+D$ reactive cross section. The renormalized experimental data by Liu and co-workers (Ref. 23) are indicated by open circles. The theoretical simulations based on the three-state ASW calculations are indicated by the heavy solid line. The renormalized single-state SW calculations (solid dots) are indicated, as well as the separate contribution for the ground (F) and excited-state (F*) reactions. (Lower panel) Ratio of the total cross sections for reaction of the ground and excited spin-orbit states, predicted by the multi-state ASW calculations, as a function of energy.

In general, as for the DF channel, the reactivity of F* (thin solid line) is small compared to that of F except at low collision energies. Nevertheless, because the F* excitation function does not show any resonance structure, we find that the integral cross section ratios, $\sigma(E_c; j_a=1/2)/\sigma(E_c; j_a=3/2)$, shown in the lower panel of Fig. 4.4, undergo a large variation in the collision energy range between 0.5 and 2.0 kcal/mol. The ratio first shows a dip near the center of the resonance peak at $E_c = 0.5$. This dip arises from the enhanced integral cross section for the ground-state reaction as a result of resonance scattering, which does not occur for reactions from F*. As the collision energy increases, the strength of the resonance scattering gradually decreases,⁷² but the reactivity of F* keeps increasing. Therefore, the ratio rises.

The ratio continues to rise until $E_c \approx 1.2$ and then starts falling. This drop is due to a competition between the decreasing rate of resonance scattering and the gradual leveling off of the F* reactivity. Beyond $E_c > 2.0$, direct scattering governs the F reactivity, and the F* reactivity levels off. Consequently the ratios also level off. Overall, the cross section ratio shows a bump centered around 1.2 kcal/mol. Because of a substantial amount of F* reactivity at collision energies near the resonance peak (~65% at full strength but only ~12% when the population of the two spin-orbit states is correctly accounted for), we find that the average over the population of F spin-orbit states has a substantial effect, by raising the high-energy side of the resonance feature. As a result, we see in the upper panel of Fig. 4.4, that in the total excitation function the resonance structure (thick line) is less pronounced than what is predicted by the single-state calculations on the SW PES.

Reaction of F* does affect the shape of the resonance feature in the collision energy range 0.5–1.5 kcal/mol. In contrast, we find that it does not make significant contributions to the disagreement with experiment in the energy range between 1.5–2.0 kcal/mol. In fact the excitation function calculated from the ASW calculation

agrees less well with experiment than that predicted by the calculations on the SW PES.

To investigate further the nature of this disagreement, we look at to the vibrational-specific excitation functions shown in the lower panel of Fig. 4.3. We see that the disagreement between 0.5 and 1.5 kcal/mol is due to the overestimation by theory of the height of the resonance peak for HF($v'=2$) products.

The disagreement with experiment between 1.5 and 2.0 kcal/mol arises mainly from the underestimation in the theoretical calculations of the cross section for formation of HF($v'=3$). The F* reaction does make some contribution here at $E_c < 1.5$ kcal/mol, where the $v'=3$ products are energetically inaccessible for reaction of the ground spin-orbit state. However, the F* reactivity is not large.

Unfortunately, the exoergicity of the F+HD \rightarrow HF+D reaction predicted by the ASW PES is 0.68 kcal/mol too low. Consequently, even after the 0.35 kcal/mol upward shift in the abscissa, the threshold for formation of HF $v'=3$ products by reaction of ground state F will be displaced 0.33 kcal/mol toward higher energy. However, it appears from lower panel in Fig. 4.3 that the onset of significant $v'=3$ flux is delayed by ~ 0.6 kcal/mol, which is too large to be explained by the remaining error in the exoergicity. Further, experiment indicates a larger $v'=3$ cross section than predicted by the calculations.

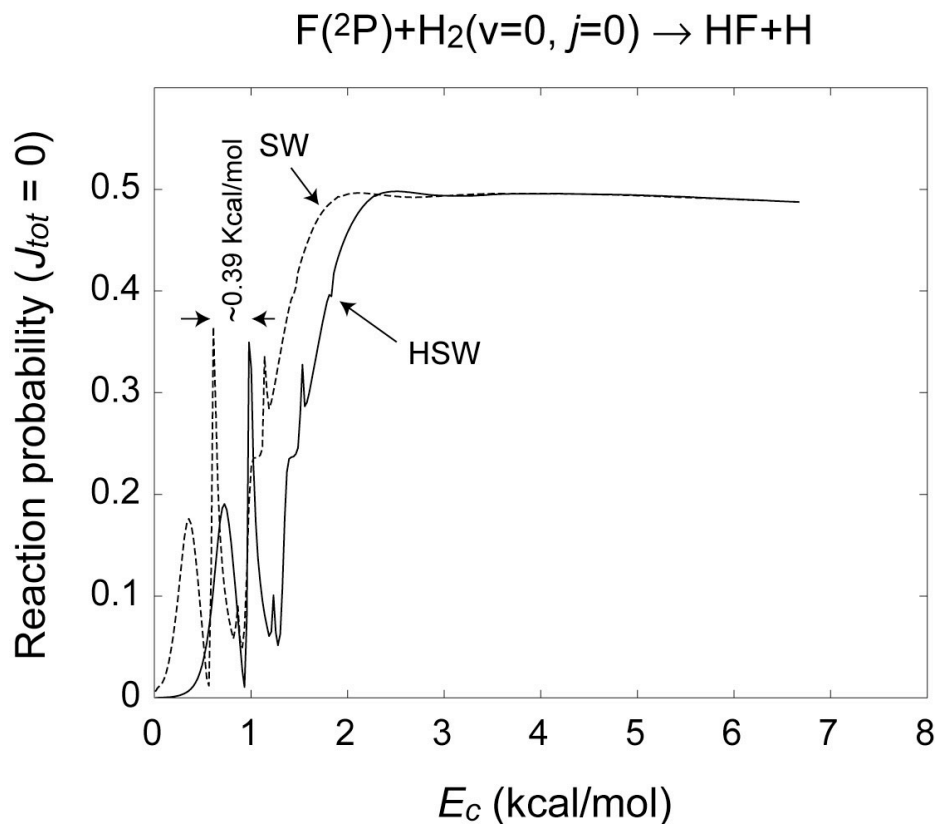


Figure 4.5 Comparison of the $F+H_2$ reaction probability distributions for the total angular momentum, ($J_{tot}=0$), as calculated on the HSW (solid line) and SW (dashed line) PES. The reaction probability has been divided by the multiple-PES factor of 2 by the same reason described in Section 4.2.3.

4.3.3 Justification for the shift of collision energies in ASW calculations

On the basis of comparisons between calculated and experimental thermal rate constants, several groups^{24,25} have concluded that, when spin-orbit coupling is properly taken into account, the barrier on the *ab initio* ASW PES for the $F+H_2$ reaction (1.91 kcal/mol) is too high, by ~ 0.3 - 0.4 kcal/mol. This is consistent with the analysis by Liu and co-workers of their experiment,²³ which suggests that the barrier on the SW PES is correct in height.²³ Because the SW PES does not take into

account the spin-orbit Hamiltonian, Liu's analysis implies that the barrier on the ASW PES is too high by ~ 0.39 kcal/mol. This is confirmed by the results of recent benchmark *ab initio* calculations.²⁶

To better understand the effect of this increased barrier height, we compare in Fig. 4.5 the reaction probability distributions for the total angular momentum ($J_{tot}=0$) of the $F+H_2(j=0)$ reaction calculated on HSW and SW PESs. The reason we compare the HSW and SW data rather than the ASW and SW is because that the ASW calculations involve non-adiabatic couplings between multiple electronic states¹, while the SW calculations are limited to the lowest adiabatically electronic state.^{4,11,16} Since non-adiabatic effect can change the reaction dynamics^{17,19} and give rise to less reaction probabilities,¹⁷ it becomes less intuitive to compare these two (ASW and SW) calculations. Nevertheless, we recognize that the HSW calculations are also limited to an adiabatic PES,¹⁶ which is almost identical to the lowest electronic state of the ASW PESs.¹ The HSW PES is obtained by adding the spin-orbit correction to the SW PES.¹⁵ Because the spin-orbit coupling lowers the energy of the $F+H_2$ reactants and leaves the reactive PES in the transition-state region unchanged.¹² Consequently, the reaction barrier on HSW PES is effectively raised by about 1/3 of the spin-orbit coupling (0.39 kcal/mol).^{1,12,15,19}

It is therefore because that the HSW PES represent the lowest electronic state of ASW PES and that the only difference between the HSW and SW PES is the barrier height, so that we compare the calculations on the HSW and SW PES to examine the effect of the increased barrier height. The comparison shows that the HSW and SW give rise to nearly identical reaction probability distributions for the total angular momentum ($J_{tot}=0$), except that they are shifted by ~ 0.39 kcal/mol, or by $\sim 1/3$ of the F spin-orbit splitting, or by the difference between the HSW and SW barrier height. The fact that a simple shift in collision energies bring the HSW reaction probability nearly identical to the SW implies that the effect of raised barrier

height mainly shift the distributions of the overall reaction probability upward, by an amount that equals the difference in barrier height. Given the observation, as described at the beginning of this subsection, that the SW PES predicts too high a barrier by $\sim 0.3\text{-}0.4$ kcal/mol, we choose to shift back the HSW, therefore ASW, collision energy by an amount of 0.35 kcal/mol. With this adjustment, the reaction probability of the ASW is almost the same as the normalized SW.

This simple upward shifting (by 0.35 kcal/mol) in the collision energies to compensate for the overestimation of the reaction barrier is further supported by our nearly perfect match with the experiment in the DF channel (see Section 4.3.1) and the improved agreement in the HF channel. It is only with this shift that we can obtain a reasonably good fit to experiment in both the DF and HF reaction channels.

4.4 Conclusions

In this Chapter we have presented the results of calculations of integral cross sections for both product channels of the F+HD reaction. From the detailed comparisons, we find theory and experiment give nearly perfect agreement for the DF product channel. In this channel, the reactivity of F*, weighted by the fractional population of F* in the beam, is very small, estimated at $\sim 5\%$ except at low collision energies. For the HF product channel agreement with experiment is less good. From Fig. 4.4 it may be argued that the multi-state calculations give a significantly better agreement with experiment, particularly the relative magnitude of the resonance feature compared with the cross section at higher energy.

Because reaction of F* does not give rise to any resonance features, averaging over the two spin-orbit states decreases the modulation depth of the resonance. The greater the fraction of F* in the incident beam, the less pronounced this resonance structure will be. Relative to the ground-state reaction, the fractional reactivity of F* is largest, $\sim 12\%$, at collision energies near $E_c = 1.2$ kcal/mol for the reaction yielding

HF products. The discrepancy in the collision energy range between $E_c = 1.5$ and 2.0 kcal/mol is attributed to the underestimation in formation of HF($v'=3$) products.

Comparisons between the SW and HSW reaction probability for the F+H₂ reaction (Fig. 4.5) and among the SW, ASW and experimental excitation functions for the F+HD reaction (Figs. 4.2 and 4.4) suggest that the best (and simplest) way to compensate for the overestimation of the reaction barrier height on the ASW PES is to shift the collision energy upward by ~ 0.35 kcal/mol. Although this gives rise to satisfactory comparison with the experiment, we find some discrepancy still exists in the HF product channel. Because the effect of F* reactivity is small over the range of collision energy probed in the experiments, the remaining disagreement with experiment reflects residual inaccuracies in the ASW and SW PESs, which were based on *ab initio* calculations which are now nearly 10 years old.

Recent test calculations²⁶ suggests that it is now possible to improve, substantially, the errors in the estimation of the F+H₂ reaction barrier and reaction exoergicity. Determination of a new, global, multi-state PES with similar methodology will provide the means for a quantitative understanding of the F+HD reaction dynamics.

5 The F+HD Reaction: The Reactivity of F*

5.1 Introduction

Over the past several years and in Chapter 3 and 4, we have presented a number of fully-quantum scattering studies of the reaction of F with H₂ and HD.^{1,8} One major goal of our studies is to understand the extent of participation of the spin-orbit excited state [F*(²P_{1/2})] in the reaction. An unresolved question is whether inclusion of the F*+HD reaction could resolve remaining discrepancies²³ between experimental results and earlier quantum scattering calculations²³ that were done under that assumption that the multiplet character of the F atom could be ignored and that only F atoms in their ground spin-orbit state could react. The inclusion of the open-shell character of halogen atoms in reactions with molecular hydrogen has been the object of intense recent theoretical interest.^{1,6-8,17,24,55,58,66,67}

As shown in Fig. 5.1, asymptotically, in the reactant arrangement, the spin-orbit Hamiltonian raises the degeneracy of the F atom.¹ The ground ²P_{3/2} and excited ²P_{1/2} spin-orbit states of the F atom are separated by 404 cm⁻¹ (≈ 1.16 kcal/mol).⁴⁷ In what follows, we shall use the more compact notation F* to designate the excited spin-orbit state of the atom. Three electronically adiabatic PESs are eigenstates of the FH₂ electronic Hamiltonian: 1A', 2A' and 1A''. Of these, only the 1A' PES correlates with HF (or DF) products in their electronic ground state (¹Σ⁺). In the reactant arrangement these three PESs are degenerate asymptotically. However, when the spin-orbit interaction is included, the excited spin-orbit state of the reactants (F*+HD) correlates only the excited 2A' PES.¹

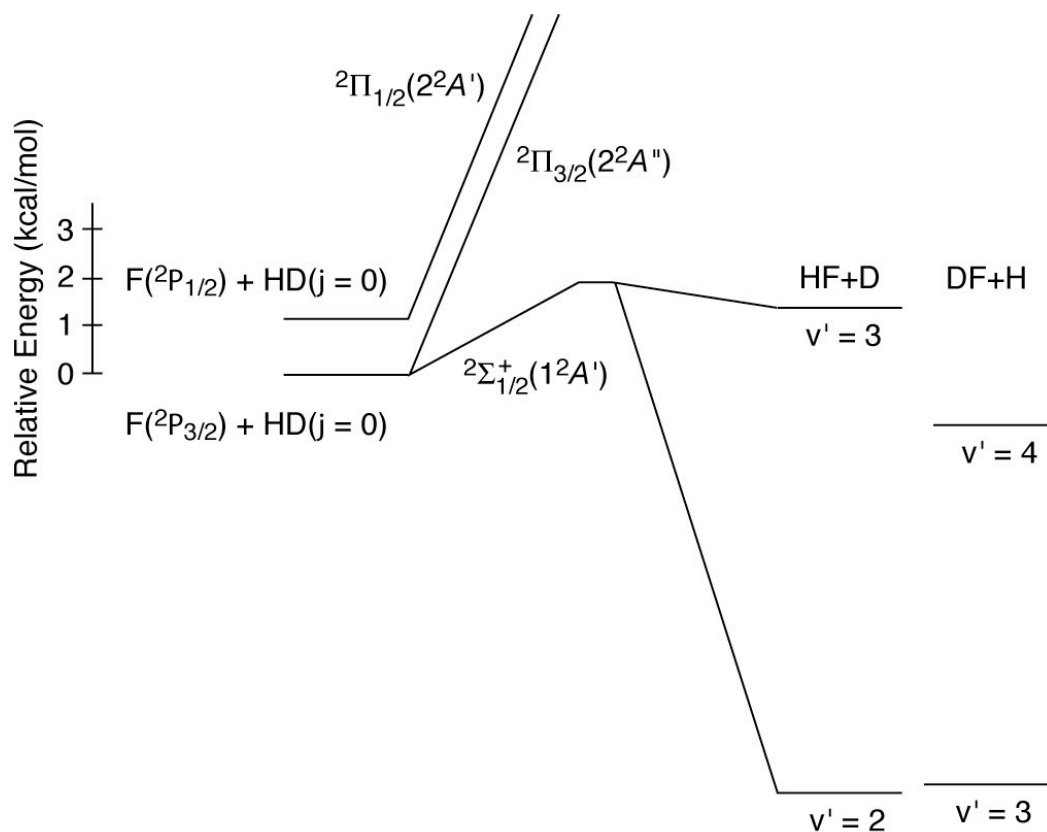


Figure 5.1 Relative energies (to scale) for the $F+HD \rightarrow HF+D$, $DF+H$ reaction, with a schematic representation of the three electronically adiabatic potentials after inclusion of the spin-orbit splitting. Only the two highest product vibrational levels are indicated.

Consequently, within the Born-Oppenheimer approximation, which constrains nuclear motion to a particular electronic adiabat, the excited spin-orbit state should not react. As the reactants approach the $1A'$ PES splits apart from the two other PESs, which are repulsive. Non-adiabatic transitions are most likely to at the point at which this splitting is roughly equal to the spin-orbit coupling.^{1,67,73} For the $F+H_2(HD)$ reaction this point occurs fairly far out in the reactant valley, well outside the barrier.¹ As the reactants approach the barrier, the splitting between the two electronically excited PESs ($2A'$ and $1A''$) and the reactive PES is so large that the

spin-orbit coupling can no longer cause nonadiabatic transitions to occur. The spin-orbit Hamiltonian plays no role in the product arrangement (for HF products in their electronic ground state) because $l=0$ for the $H(^2S)$ ground state.

In Chapters 3 and 4, we investigated how inclusion of the full open-shell character of the F atom affects the angular distributions (differential cross sections) for the $F+H_2$ reaction (Chapters 3), as well as the behavior of the overall $F+HD \rightarrow HF+D$ and $DF+H$ excitation functions (Chapters 4). In Chapter 4, we demonstrated that the reaction of F^* to yield HF did not show the resonance structure in the energy dependence of the integral cross sections, seen²² experimentally and in theoretical simulations based on the single Stark-Werner (SW)¹² PES. Consequently, the greater the fraction of F^* in the incident beam, the less pronounced will be this resonance structure.

Our determination of the reactive cross sections and product distributions involves a time-independent treatment of the scattering, based on four quasi-diabatic potential energy surfaces (PES), the Alexander-Stark-Werner (ASW)¹ PESs. All couplings (electronic mixing of the two states of A' reflection symmetry, spin-orbit, and Coriolis) are included, as exactly as possible. Recently, Han, Zhang and co-workers^{7,55} have developed an equivalent time-dependent approach for reactive scattering on multiple PESs, and have successfully applied it to the reactions of F with H_2 , D_2 and HD.

Because of the additional electronic energy of the spin-orbit excited state, at a given initial collision energy, the F^*+HD reaction can yield HF or DF product states which are energetically inaccessible in the ground-state reaction. In several papers, Nesbitt has argued that the only unambiguous probe of the extent of reactivity of the F atom spin-orbit excited state is the demonstration of the production of HF (or DF) which are energetically forbidden for the ground-state reaction.^{27,64,74} Unfortunately, the finite spread of translational energy in any molecular beam experiment, the

presence of excited rotational states of H₂ (or HD) in the beam, and the small magnitude of reactive cross sections at threshold will add ambiguity to this demonstration.

Nesbitt, Liu, and their coworkers have argued that the F+HD reaction is the best candidate to investigate the relative reactivity of the two spin-orbit states of F.^{23,27,64,74} As shown schematically in Fig. 5.2, the production of HF products in $v'=3$ is possible only for collision energies greater than 1.32 kcal/mol. By carrying out experiments at lower collision energies, and monitoring the HF products, Nesbitt, Liu and their co-workers have obtained direct evidence of the reactivity of the excited spin-orbit state.

As a complement to these experiments, and to help in understanding them, we present here the results of quantum scattering calculations on the F+HD→HF+D, DF+H reaction. We then use these results to carry out a careful simulation of the experiments of Liu, Nesbitt and their co-workers.^{23,27} This Chapter is organized as follows: Section 5.2 contains a brief review of the theoretical methods used. In Section 5.3, we compare with experiment the results of the simulation of the HF and DF product translational energy distributions. Section 5.4 reports a similar comparison for the product rotational distributions. A discussion and conclusion follow.

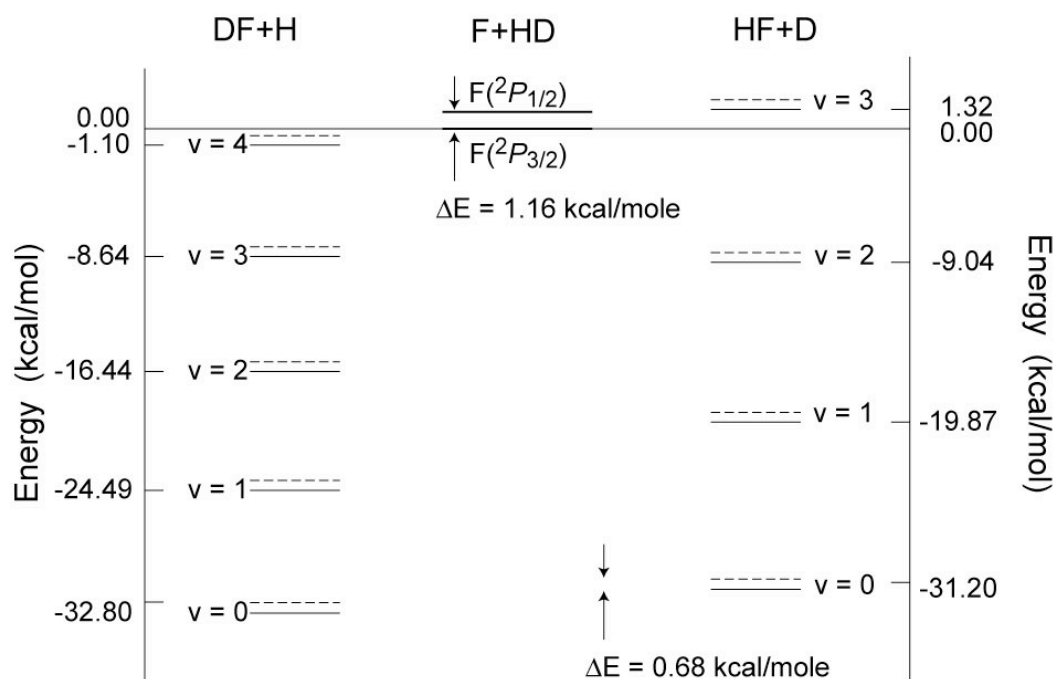


Figure 5.2 Energy level diagram (to scale) of the $j = 0$ HF and DF product vibrational-rotational states in the F+HD reaction. The solid and dashed lines refer to the experimental positions [computed from the known heats of formation (Table 5.1) and the HF (DF) spectroscopic constants] and the predictions based on the ASW FH₂ potential energy surface (Ref. 1).

5.2 Method

5.2.1 Details of the scattering calculations

The exact, quantum description of the reaction of F+HD follows the formalism presented earlier by Alexander, Manolopoulos and Werner.¹ A full description requires three potential energy surfaces (PESs) and an accurate

description of the couplings (non-adiabatic, spin-orbit, and Coriolis) among them. We refer the interested reader to Ref.1, and will reiterate here only those details directly relevant to the present investigation.

5.2.2 Comparison with experiment

To simulate as closely as possible the experiment of Liu and co-workers,²³ we have to take into account the energy spread of the molecular beams and the finite resolution of the detector. To do so, we choose a simple approach which consists in multiplying the integral cross section of Eq. (4.1) by a Gaussian function. The cross section for production of products with translational energy E_{tr} from reaction of $F(j_a)$ with $HD(v_j)$ is then given by

$$P_{j_a v_j}(E_{tr}) = \sum_{v' j'} \sigma_{j_a v_j \rightarrow v' j'}(E_{j_a v_j}) N \exp\left[-(E_{tr} - E_{v' j'})^2 / 2a^2\right], \quad (5.1)$$

Here N is the normalization constant for the Gaussian and $E_{v' j'}$ is the translational energy associated with particular product channel $v' j'$, which is given, similarly to Eq. (4.2) by

$$E_{v' j'} = E - e_{v' j'}. \quad (5.2)$$

We take the parameter a in Eq. (5.1) equal to 0.3 kcal/mol, which corresponds to a fwhm of the Gaussian convolution of 0.68 kcal/mol. The experiments reported in Ref. 23 determine only relative cross sections. For comparison we will compare simulated product translational energy distributions $P_{j_a v_j}(E_{tr})$ obtained by multiplying the cross sections of Eq. (5.1) by an overall constant scaling factor, identical for both the DF and HF product channels, to bring the theoretical cross sections to a magnitude comparable to the experiment. This scaling process is consistent with the normalization method used in the experiment (see the caption of Fig. 5 in Ref. 23).

Both F* and F are present in the initial molecular beam, as well as a distribution of HD rotational states. Thus an experimental observed distribution of HF (or HD) products with translation energy E_{tr} is simulated as

$$P(E_{tr}) = \sum_{j_a \nu_j} w_{j_a} p_{\nu_j} P_{j_a \nu_j}(E_{tr}), \quad (5.3)$$

where w_{j_a} and p_{ν_j} are, respectively, the relative populations of the atomic spin-orbit states and molecular vibration-rotation states. In our calculations we chose w_{j_a} to be given by a Boltzmann distribution at the temperature of 600K which characterizes the F atom velocity in the atom source used by Liu and co-workers,²³ so that $w_{F^*} = 0.16$ and $w_F = 0.84$.⁷⁵ We further assume that only the $\nu=0$ vibrational level is populated, and, further, that HD is confined to its two lowest rotational levels with $p_{j=0} = 0.82$ and $p_{j=1} = 0.18$ at the experimental rotational temperature of 50K.²³

Several groups^{24,25} have concluded, on the basis of comparisons with thermal rate constant measurements, that, when spin-orbit coupling is properly taken into account, the barrier on the *ab initio* ASW PES (1.92 kcal/mol),¹ is too high, roughly by ~ 0.3 - 0.4 kcal/mol. This is consistent with ongoing extensive *ab initio* calculations,²⁶ aimed at providing the framework for improvements in the SW and ASW PESs, which are now nearly a decade old. In our earlier paper,²¹ we concluded that outstanding agreement with the experimental F+HD \rightarrow FD+H reactive excitation function could be obtained by shifting the collision energy in the calculations by 0.35 kcal/mol, so that experimental cross sections at E_c would be compared with calculated cross section at a collision energy of $E_c + 0.35$ kcal/mol. This adjustment was also used here.

In addition, the calculated exoergicity of the F+HD \rightarrow FH+H reaction is 0.68 kcal/mol too low, as shown in Fig. 5.2. This has the consequence of lowering by 0.68 kcal/mol the translational energy of each product state. Because the goal of the present study is a direct comparison with product translational energy distributions,

we decided that the most accurate comparison could be achieved by (a) calculating all reactive cross sections at a collision energy equal to the nominal experimental collision energy *plus* 0.35 kcal/mol (as discussed in the preceding paragraph) and then (b) determining the available translational energy of each $v'j'$ product state by subtracting from the total available energy the true energy of this state. The latter is determined from the most recent estimate of the heats of reaction along with the experimental energies $e_{v',j'}^{ex}$ of all vibration-rotation energies of the HF or DF products. The latter are obtained from a standard Dunham expansion based on available spectroscopic coefficients for either HF⁷⁶ or DF.⁷⁷

As a result of these adjustments, the product translational energy, $E_{v'j'}$ in Eq. (5.2) becomes

$$E_{v'j'} = (E_{th} - 0.35) - \Delta E_{rxn} - e_{v',j'}^{ex}, \quad (5.4)$$

where E_{th} is the total energy in the theoretical calculation and ΔE_{rxn} is the experimental zero-point corrected heat of reaction (−31.20 kcal/mol for HF+D and −32.80 kcal/mol for DF+H) obtained from the available gas-phase thermochemistry data listed in Table 5.1.

To simulate the experiments of Nesbitt and co-workers,²⁷ in which infrared absorption was used to monitor HF product states obtained from a crossed-beam experiment, it is necessary to average the integral cross sections of Eq. (4.1) over a distribution of collision energies. We obtain

$$\langle \sigma_{j_a v_j \rightarrow v' j'} \rangle = \int \sigma_{j_a v_j \rightarrow v' j'}(E_{j_a v_j}) \exp\left[-(E_{col} - E_{j_a v_j})^2 / 2a^2\right] dE_{j_a v_j} \quad (5.5)$$

We chose the Gaussian parameter $a=0.170$ kcal/mol, so that the Gaussian distribution in Eq. (5.5) has a width (fwhm) of 0.4 kcal/mol, comparable to the spread in collision energy in the experiments.²⁷ We take the collision energy in Eq. (5.5) equal to 0.95 kcal/mol, which is the nominal collision energy in the experiments plus the same

upward shift of 0.35 kcal/mol invoked earlier in this Section to compensate for the excessively high barrier on the ASW PES.

We need, in addition, to average over the rotational distribution of the HD reactants. As in Eq. (5.3), we define

$$\langle \sigma_{j_a \rightarrow v'j'} \rangle = \sum_{vj} p_{vj} \langle \sigma_{j_a vj \rightarrow v'j'} \rangle, \quad (5.6)$$

where in the experiments of Nesbitt and co-workers, $p_{00}=0.9$ and $p_{01}=0.1$.²⁷

Table 5.1 Heats of formations $\Delta_f H^0_{gas}$ (kJ/mol and kcal/mol) used to determine [Eq. (5.4)] the zero-point corrected exothermicities (ΔE_{rxn}) of F+HD reactions.^a

Species	kJ/mol	kcal/mol
H ₂	0	0
HD	0.32	0.077
DF	-275.52	-65.851
HF	-272.55	-65.141
F	79.39	18.975
D	221.72	52.992
H	218.00	52.103

a. M. W. Chase, Jr., NIST-JANAF Thermochemical Tables, Fourth Edition, J. Phys. Chem. Ref. Data, Monograph **9**, 1, (1998) (<http://webbook.nist.gov>). 1 kcal/mol = 4.184 kJ/mol.

5.3 Results: Product Translational Energy Distributions

In the discussion that follows we will compare the calculated product translational energy distributions with those obtained experimentally by Liu and co-workers.²³ In the simulations it is possible to distinguish two reaction mechanisms. The first is product formation by reaction of the ground spin-orbit state [$F(^2P_{3/2})$]. This pathway is adiabatically allowed by reaction on the lowest electronically adiabatic PES which correlates directly reactants, in their electronic ground state, with HF (or DF) products in their electronic ground state ($^1\Sigma^+$). The second mechanism is reaction of the excited spin-orbit state [$F(^2P_{1/2})$] which is adiabatically forbidden, because the excited spin-orbit state correlates adiabatically only to HF (or DF) products in their first excited electronic ground state ($^3\Pi$), which is quite high in energy and therefore inaccessible for reactions at moderate collision energies.^{57,70}

5.3.1 $F+HD\rightarrow DF+H$

Using the simulation procedures described above we obtain the calculated product translational energy distributions $P(E_{tr})$ for the $F+HD\rightarrow DF+H$ reaction shown in Fig. 5.3, at the nominal collision energies reported by Liu and co-workers.²³ These have also been compared with experiment (dashed lines). The thin and thick solid lines depict, respectively, the total contributions [Eq. (5.3)] of reaction of the ground and excited spin-orbit states of the F atom and the relative contribution of just the excited spin-orbit state. Each panel contains a smaller inset panel that compares in more detail the distribution of products with low translational energy.

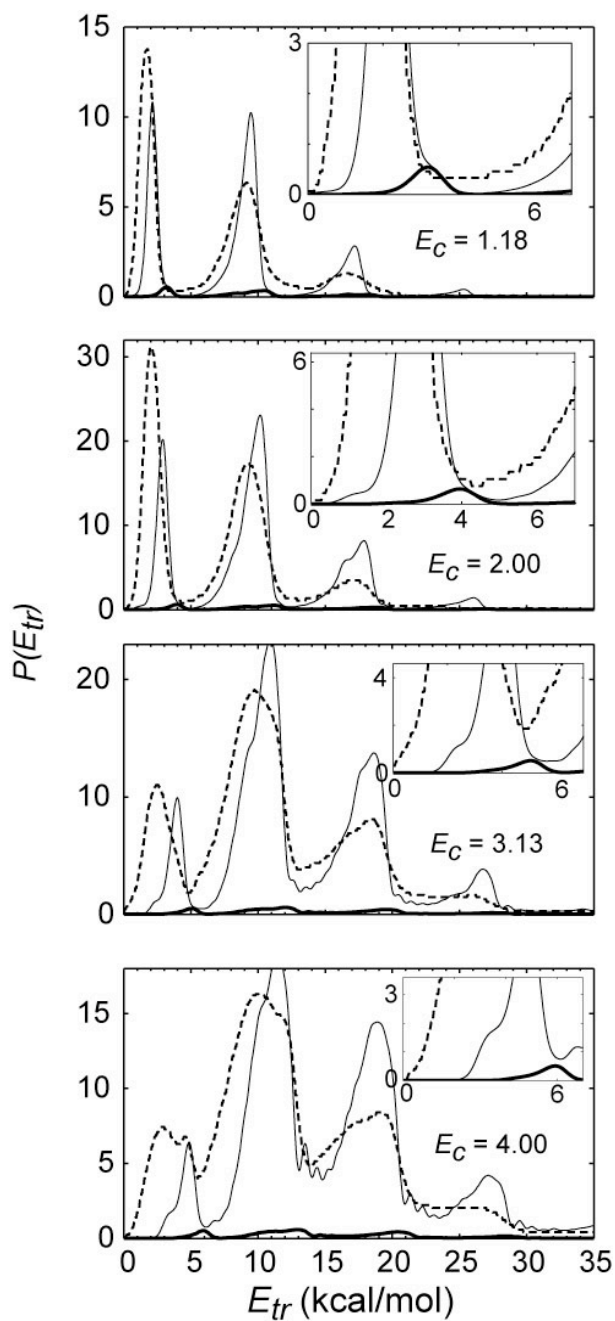


Figure 5.3 Comparisons of theoretical and experimental product translational energy distributions for the $F+HD \rightarrow DF+H$ reaction at collision energies of 1.18, 2.00, 3.13 and 4.00 kcal/mol. The dashed curves are the experimental results from Ref. 23, the thin solid curve is the predicted distribution of Eq. (5.3), and the thick solid curve is the predicted distribution but containing just the contribution of the reaction of $F(^2P_{1/2})$, obtaining by limiting the sum in Eq. (5.3) just to $j_a = 0.5$.

Given the excellent agreement with experiment we reported for the overall excitation functions of this channel, we are surprised here to find noticeable disagreements in the translational energy distributions. The most noticeable disagreement is an underestimate of the higher rotational states of the DF($v' = 4$) products at all the experimental collision energies. This is shown by an underestimation of products with the lowest translational energy in Fig. 5.3. A similar underestimation of the higher rotational states of DF($v' = 3$) products is also apparent at the two higher [$E_c = 3.13$ and 4.00 kcal/mol] collision energies. In addition, the theoretical simulations consistently overestimate the formation of DF($v' = 2$ and 1) products at all collision energies.

To analyze these differences we refer to the vibrational-state-specific reactive cross sections in the upper panel of Fig. 4.3 and compare these with experiment. These quantities are defined by

$$\sigma_{v'}(E_c) = \sum_{j_a v_j} w_{j_a} p_{v_j} \sum_{j'} \sigma_{j_a v_j \rightarrow v' j'}(E_{j_a v_j}) . \quad (5.9)$$

Because of the finite range of total energies subtended in the scattering calculation, calculations of cross sections for reaction of the excited spin-orbit atom are possible only for $E_c \leq 2.68$ kcal/mol (see Table 4.2). Because of the higher internal energy of the F* reactant, for a given total energy, the collision energy is larger for F atoms in their ground spin-orbit state. Consequently, the range of total energies subtended in the scattering calculations allow determination of cross sections for the adiabatically-allowed ground-state reaction up to collision energies of 3.82 kcal/mol. We can compare with experiment at collision energies between 2.68 and 3.82 kcal/mol by extrapolating the F*+HD cross sections, which make only a small contribution to the total, and then adding these to the exact F+HD cross sections. The results of this extrapolation are indicated by dashed lines in Fig. 4.3.

The experimental values in Fig. 4.3 were taken from Figs. 6 and 8 of Ref. 23. These values were normalized so that the overall experimental excitation function, obtained by summing over all energetically-accessible product vibrational levels, agreed as closely as possible with the total reactive cross section, again summed over product vibrational levels. The normalization procedure is discussed in more detail in Ref. 23.

We note that there is a re-distribution of reaction flux such that the underestimate in the higher rotational states of $v'=4$ (and, at higher energies, $v'=3$) products is well compensated by an overestimate of the cross section for formation of $DF(v'=2)$ and (not shown) $v'=1$. As a result, when summed over product vibrational state, the excitation functions agree perfectly with experiment.

We see in Fig. 5.3 that reaction of $F(^2P_{1/2})$ makes only a small contribution to the $F+HD \rightarrow DF+H$ reaction. Likely, this is one reason why earlier calculations,^{5,22,35} which did not consider the reactivity of F^* , agree well with experiment for the $F+HD \rightarrow DF+H$ channel. Also, as seen most clearly in the insets in Fig. 5.3, the reactivity of $F(^2P_{1/2})$ makes little contribution to the formation of products in $v'=4$ since this vibrational state is always energetically accessible for reaction of $F(^2P_{3/2})$.

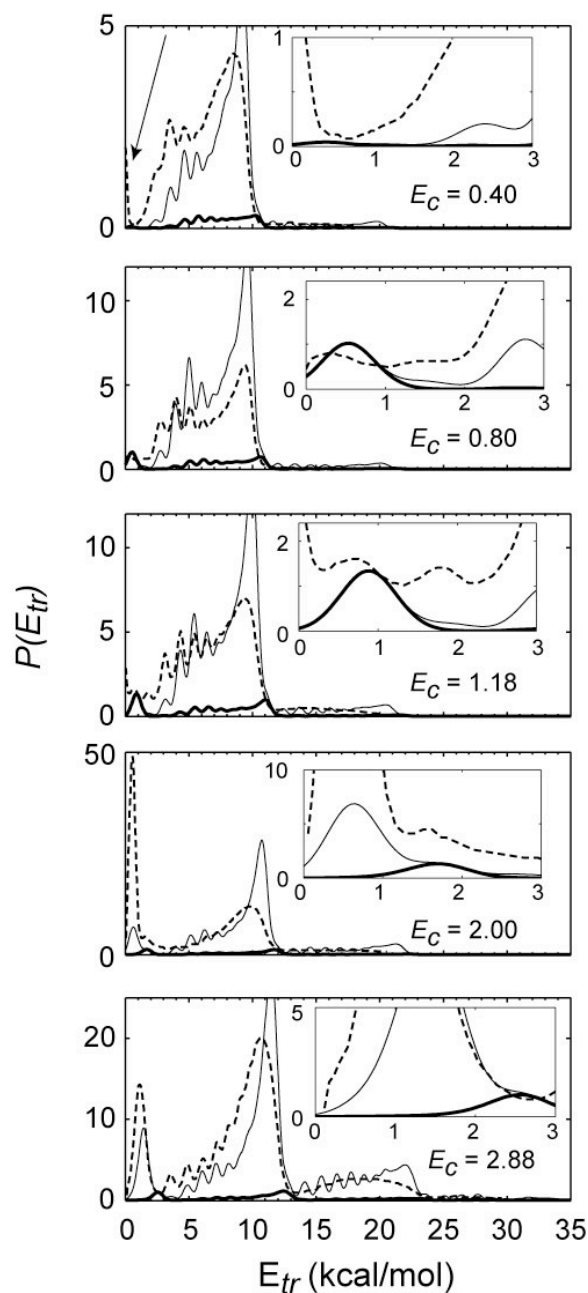


Figure 5.4 Comparisons of theoretical and experimental product translational energy distributions for the $F+HD\rightarrow HF+D$ reaction at collision energies of 0.40, 0.80, 1.18, 2.00 and 2.88 kcal/mol. The dashed curves are the experimental results from Ref. 23, the thin solid curve is the predicted distribution of Eq. (5.3), and the thick solid curve is the predicted distribution but containing just the contribution of the reaction of $F(^2P_{1/2})$, obtaining by limiting the sum in Eq. (5.3) just to $j_a = 0.5$.

5.3.2 F+HD → HF+D

Product translational energy distributions for the HF channel are shown in Fig. 5.4, in a format similar to Fig. 5.3. The corresponding vibrational-state-specific excitation functions are shown in the lower panel of Fig. 4.3. The largest peak corresponds, at each collision energy, to formation of products in $v'=2$. At higher translational energy, the much less intense product energy distributions correspond to formation of products in $v'=1$. As seen in Fig. 5.2, formation of products in $v'=3$ is forbidden for $E_c < 1.32$ kcal/mol. In the two lower panels of Fig. 5.4, which correspond to $E_c = 2.00$ and 2.88 kcal/mol,⁷⁸ the sharp peak at low translational energy corresponds to products in $v'=3$. At $E_c = 0.80$ and 1.18, appears a small hint of this larger $v'=3$ peak. At these collision energies, formation of $v'=3$ products is allowed by reaction of F($^2P_{1/2}$), in which the additional spin-orbit energy (1.2 kcal) renders $v'=3$ products energetically accessible.

The insets in the second and third panels of Fig. 5.4 show that reactivity of the spin-orbit excited state is responsible for virtually all the formation of HF products in $v'=3$ products formation, which have the lowest translational energy. As the collision energy increases, the reaction of the spin-orbit ground state to yield HF($v'=3$) becomes energetically allowed. This is manifested by the sharp increase in the magnitude of the translational energy distributions, especially at low E_{tr} . At the higher values of E_c the contribution of the adiabatically forbidden reaction of the spin-orbit excited atom is less significant.

We observe that the oscillations predicted in the translational energy distributions for HF products in $v'=2$ matches, almost exactly, the oscillations seen experimentally. This is a consequence of using the exact HF vibrational-rotation energies and the exact reaction exothermicity in Eq. (5.4). Since the HF vibration-rotation energies are predicted well by the ASW PES, replacement of the

experimental vibration-rotation energies values of $e_{v'j'}$ with the theoretically predicted values causes little change in the predicted translational energy distributions.

We note that the simulations fails to reproduce the prominent spike near zero translational energy for reaction at $E_c = 0.4$ kcal/mol. This is marked by an arrow in the top panel in Fig. 5.4. Liu and co-workers assigned this peak to HF($v'=3$) products formed by the reaction of $F(^2P_{1/2})$. This discrepancy is a consequence of the error of 0.68 kcal/mol in the exothermicity of the $F+HD \rightarrow FH+D$ reaction predicted by the ASW PES. As shown in Fig. 5.2, the $F^*+HD \rightarrow HF(v'=3, j=0)+D$ channel becomes energetically accessible for $E_c > 0.16$ kcal/mol. However, because of this error in the exothermicity, in the theoretical scattering calculations this $v'=3$ channel becomes open only for $E_c > 0.84$ kcal/mol. Although an upward shift of $\Delta E_c = 0.35$ kcal/mol has been applied in the simulations, to compensate for an excessively high barrier on the ASW PES, despite this shift the $v'=3$ channel is still closed in the theoretical simulations at $E_c = 0.4$ kcal/mol. Consequently, at $E_c = 0.4$ kcal/mol, the theoretical simulations predict that reaction of $F(^2P_{1/2})$ will produce only products in $v' \leq 2$, and therefore give any indication of the peak at threshold seen in the experimental data.

We observe a large difference in the predicted as compared to experimental intensities at low translational energies ($E_{tr} \approx 0.5$ kcal/mol), and hence associated with HF products in $v'=3$, as seen in the $E_c = 2.00$ kcal/mol panel. The inset to this panel shows that in this range the F^* reaction makes little contribution. Examination of Fig. 4.3 shows that for collision energies in the range $1.5 \leq E_c \leq 2$ kcal/mol, the scattering calculations, even when the collision energy is shifted up by an additional 0.35 kcal/mol, show very little reactivity into HF($v'=3$). Thus the large underestimation of the low translational energy peak in the panels for $E_c = 2.00$ and (too a lesser extent) 2.88 kcal/mol can be attributed to errors in the predicted dynamics of reaction of spin-orbit ground state F atom.

We observe good, but not perfect, agreement between the simulations and experimental product translational energy distributions over the range of values of E_{tr} , which correspond to HF products in $v'=2$. As can be seen in Fig. 5.4, reaction of the excited spin-orbit state makes only a very small contribution here. Consequently, we conclude that the disagreement is an indication of an imperfect prediction of the prediction of product formation by the adiabatically-allowed reaction of ground-state F.

Looking at Fig. 4.3, we see that for production of $v'=2$ the simulations overestimate the vibration-specific excitation functions for collision energies < 3 kcal/mol. In particular, the calculations overestimate the height of the resonance peak at $E_c \cong 0.5$ kcal/mol. It is for this reason that the simulations overestimate the product translational energy distributions in the range of $E_{tr} = 4-10$ kcal/mol for collision energies of 0.8, 1.18, and 2.00 kcal/mol. This overestimation is true in particular for large peak near $E_{tr} = 10$ kcal/mol, which corresponds to production of HF in low rotational levels of the $v'=2$ manifold.

Because of the finite range of energies sampled in the scattering calculations, the vibration-specific excitation functions were extrapolated for $E_c > 2.68$ kcal/mol, as described in the section 5.3.1. The extrapolated simulated excitation functions drop below the experimental values for HF($v'=2$) at higher energies.

In summary, then, we see that although the reactivity of the spin-orbit excited (F^*) atom is small, it does provide the only mechanism for the formation of HF products in $v'=3$ when this vibrational manifold is not energetically accessible by reaction of the spin-orbit ground state atom. As the collision energy increases to the point where reaction of $F(^2P_{3/2})$ is energetically allowed, this adiabatically allowed mechanism rapidly dominates. Consequently, deviations between experiment and theory for the product translational energy distributions associated with energetically allowed product channels (HF in $v'=2$ and $v'=1$), reflect inadequacies in the

simulation of the reaction dynamics on the lowest (adiabatically allowed) potential energy surface.

5.3.3 Statistical weighting of the ground and the spin-orbit excited states

In our simulation we assumed that the populations of the $F(^2P_{3/2})$ and $F(^2P_{1/2})$ states in the beam are in thermal equilibrium at the temperature (600K) which characterizes the speed of the F atoms in the beam source.²³ This leads to a prediction of a relative population of 16% in the spin-orbit excited state. Unfortunately, there is no direct experimental measurement of this population ratio.²³ From Fig. 5.4 we see that at collision energies of 0.8 and 1.18 kcal/mol, the HF products with translation energy < 1 kcal/mol are predicted to arise almost exclusively from reaction of F^* atoms, while the products at higher translational energy are due to reaction of spin-orbit ground-state atoms. The overall excellent agreement with the entire range of product translational energy distributions for these two collision energies, strongly suggests that the thermal population ratio (0.16:0.84) is an excellent predictor of the atom populations in the molecular beam. It is also clear that the assumption of a purely statistical ratio based on the electronic-state degeneracy (0.33:0.67) will substantially overestimate the $F(^2P_{1/2})$ reactivity. If this latter ratio were assumed, the product translational distributions for $E_{tr} \leq 1$ kcal/mol in the second and third panels of Fig. 5.4 would be predicted to be substantially greater (by roughly a factor of two) than seen experimentally.

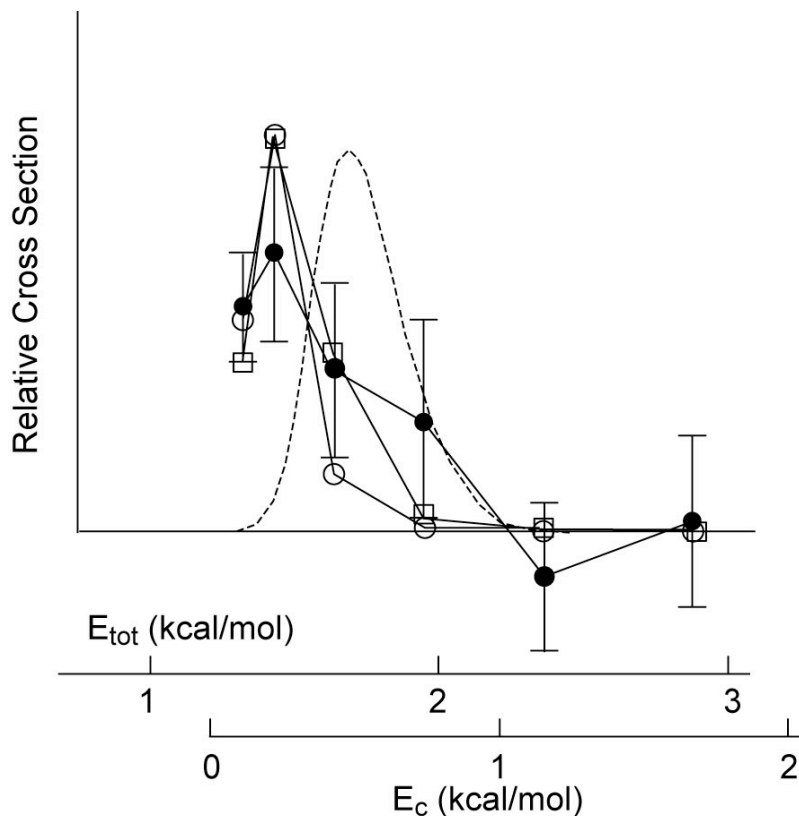


Figure 5.5 Comparison of simulated HF($v'=3$) rotational distributions with those obtained by Nesbitt and co-workers (Ref. 27, closed circles) at a nominal collision energy of 0.6 kcal/mol (see Fig. 9 of this reference). The simulated distributions (open circles) were obtained from cross sections calculated over a range of collision energies, shifted by +0.35 kcal/mol, and then averaged over a Gaussian distribution with fwhm=0.4 kcal/mol, and further averaged over a distribution of rotational populations of the HD reactant identical to those reported in Ref. 27. The open squares display similar simulated distributions, but with an energy shift of +0.68 kcal/mol. The upper abscissa corresponds to the total energy, measured with respect to $F(^2P_{3/2})+HD(v=0, j=0)$. This is the same energy scale as shown in Fig. 5.2. The lower abscissa corresponds to the initial relative energy of the F^*+HD reactants. The dashed curve indicates the width of the collision energy distribution (centered at 0.6 kcal/mol), taken from Ref. 27.

5.4 Results: Product Rotational Distributions

Figure 5.5 displays the simulated product rotational distributions for the HF products in $v'=3$, following reaction of F+HD at $E_c = 0.6$ kcal/mol. These are compared with the experimental results of Nesbitt and coworkers.²⁷ At this nominal collision energy, only the reaction of the excited spin-orbit atom can produce HF products in $v'=3$.^{23,27} Since the collision energy distribution is negligible for $E_c \geq 1$ kcal/mol (Fig. 5.5), and the spin-orbit splitting in the F atom is 1.16 kcal/mol, the contribution of the adiabatically allowed F+HD reaction can be neglected with confidence.

We observe in Fig. 5.5 a reasonable agreement between the simulated rotational distributions and the results of the experiment. Notwithstanding the considerable error bars in the experimental data, the simulated distributions are noticeably colder than seen experimentally. Because of the *ab initio* value of the exoergicity is 0.68 kcal/mol too low (Fig. 5.2), the ($v'=3, j'=3$) level of HF is inaccessible for collision energies below 1.47 kcal/mol in reaction of F* with HD($j=0$) and below 1.21 kcal/mol in reaction of F* with HD($j=1$). Even when our shift of 0.35 kcal/mol is taken into account, the range of collision energies sampled in the experiments of Nesbitt and co-workers is still too low to allow significant population in HF($v'=3$) rotational levels greater than $j'=2$.

If we shift the collision energy up by 0.68 kcal/mol, to compensate, somewhat, for the error in the calculated exothermicity, we obtain a somewhat hotter rotational distribution. This is shown by the open squares in Fig. 5.5. However, even with this correction, the distribution is colder than seen experimentally, although certainly within the error bars of the experiment.

5.5 Discussion And Conclusion

One major shortcoming in the present treatment is our shift of the collision energy in the theoretical simulations by 0.35 kcal/mol above the experimental value. This was done to compensate, albeit somewhat artificially, for an overly high barrier on the ASW PES. Ongoing *ab initio* studies²⁶ indicate the barrier on the ASW PES is roughly 0.25-0.30 kcal/mol too high. The remaining disagreements with the experimental translational energy distributions, which are primarily due to errors in the description of the adiabatically-allowed reaction of the ground spin-orbit state, suggest that this simple shift in collision energy is not sufficient to correct fully for errors in the ASW PES. In addition, recently Skodje, Mebel and co-workers have used *ab initio* calculations to correct artifacts in the SW PES in the van der Waals region in the product arrangement.⁷⁹ It is clear that a more accurate, global set of PESs is necessary to improve our ability to simulate well the reaction of F with hydrogen and its isotopomers.

Another drawback is the underestimation of the reaction exothermicity in the *ab initio* calculations of Stark and Werner, published nearly a decade ago.¹² In the determination of the product translational energy distributions this is compensated for by use of the experimental exothermicity in the calculation of the product internal energies. However, in the comparison with the experimental HF($v'=3$) product rotational distributions, especially for $j' > 2$, it is not clear whether the observed disagreement is due to this error in the calculated exothermicity or due to subtle inaccuracies in the *ab initio* PESs.

One might ask whether an improved *ab initio* calculation will change the non-adiabatic electronic couplings and, by consequence, alter the degree of predicted nonadiabaticity in the reaction. In a recent investigation of the Cl+H₂ reaction Alexander and co-workers⁶⁷ find that among three possible mechanisms for non-adiabatic transitions (electrostatic mixing between the reactive and repulsive

potentials of A' symmetry, Coriolis coupling, and spin-orbit coupling), it is the latter which dominates. Since the nonadiabatic transitions occur fairly far out in the reactant arrangement, where the spin-orbit splitting is virtually identical to its asymptotic value in the Cl atom, it is unlikely that small changes in the potential energy surfaces will alter the strength of the spin-orbit coupling. Likely the same conclusion will apply to the F+H₂ and F+HD reactions, so that improvements in the PESs will have little effect on the degree of nonadiabaticity in the reaction. In other words our conclusion on the magnitude and relative importance of the reactivity of the spin-orbit excited F atom as well as the agreement with experiment will be unaffected even if the PESs are subjected to small-scale modifications.

One major limitation of any crossed-beam experiment is the inability to measure absolute cross sections. However, it might be possible to extract the relative reactivity of F as compared to F*, as Liu and co-workers have done for the similar Cl+H₂ reaction.⁸⁰ As demonstrated in the first three panels of Fig. 5.4, at low collision energies, the ratio of the HF product distributions at low translational energy, which arise primarily by reaction of F* with those at higher translational energy, which arise predominately by reaction of ground-state atoms, can reveal the relative reactivity of the ground and spin-orbit excited channels. This relative reactivity is well predicted by the simulations presented here. We believe this indicates that our scattering calculations provide an accurate estimate of the relative efficiency of the non-adiabatic reaction of F(²P_{1/2}) as compared to the adiabatically-allowed reaction of F(²P_{3/2}).

In this Chapter we have presented the results of calculations of the product translational energy distribution functions and vibrational-specific excitation functions for the F+HD→FH+D and FD+H reactions, as well as product rotational distributions for the F+HD→FH(v'=3)+D reaction. From the detailed comparisons we find that theory and experiment agree well in describing the importance of the

reactivity of the spin-orbit excited atom. The major differences between the simulated and experimental product translational energy distribution functions are associated with errors in the predicted reactivity of the ground-spin-orbit-state atom $F(^2P_{3/2})$ rather than $F(^2P_{1/2})$. In the case of the HF($v'=3$) product rotational distributions it is the errors in the calculated reaction exothermicity which limit the accuracy of the simulation.

Our analysis leads to the following conclusions. First, there is clear evidence of the reactivity, albeit small, of $F(^2P_{1/2})$. This is particularly true at collision energies low enough that reaction of $F(^2P_{3/2})$ to form HF($v'=3$) is energetically forbidden. For collision energies and for product channels where reaction of the ground-spin-orbit state is energetically allowed, this process dominates the adiabatically forbidden reaction of the excited spin-orbit state. The simulations do not lead to perfect agreement with experiment, due to residual inaccuracies in the existing *ab initio* PESs, in particular the height of the barrier and the predicted exothermicity. The discrepancies between theory and experiment are not artifacts of an improper treatment of nonadiabaticity in this reaction. Consequently, we encourage further refinement and improvement of global FH₂ potential energy surfaces. Finally, comparison of the simulation product translational energy distributions with experiment indicates strongly that the relative population of the two spin-orbit states of the F atom in the beam is well predicted by a thermal equilibrium at the translational temperature of the halogen.

6 Summary

In this dissertation we have presented the quantum mechanical study of the open-shell character of the F atom in the F+H₂ and F+HD reactions. The calculations involved multi-state [Alexander-Stark-Werner (ASW)] potential energy surfaces (PES) and included an accurate treatment of the non-adiabatic couplings among them. Overall, except at low collision energies, the reactivity of F spin-orbit excited state (F*) is small, at most ~25% of the reactivity of the F ground state. After taking into account the (16%) fractional population of F* in the F beam under typical experimental conditions, the F* reactivity becomes negligible, contributing at most ~5% of the reaction cross section. As a result of this small reactivity, we find that reaction from the F* cannot account for the remaining discrepancies [Fig. 3.8 for the F+H₂ reaction and Fig. 4.1 for the F+HD reactions] between the experiment and the calculations on the adiabatic SW PES.

Despite the low overall reaction probability of the excited spin-orbit state,¹ we have shown in the studies of the F+HD → HF+D reaction (Chapter 4) that the excited spin-orbit state is responsible for noticeable features in the reaction (Chapter 4). For this reaction, the integral cross section for reaction of the ground spin-orbit state of F shows a strong resonance feature at low collision energies,²² but that of F* does not. As a result, the exact shape of the resonance feature in the energy dependence of the overall reaction cross section sensitively depends on the amount of F* present in the beam.

From our accurate prediction of the relatively small contribution of F* reactivity in the F+HD reaction (Chapter 5), we find that the discrepancies between theory and experiment, on the intensity of resonant structure at $E_c \sim 0.5$ kcal/mol and on the small bump of the HF product excitation functions at E_c between 1.5 and 2.0

kcal/mol, are not artifacts of an improper treatment of nonadiabaticity in this reaction. Therefore, the explanation of these discrepancies will rely on further investigation for the reaction on the lowest electronic state. Given the fact that there remain residual inaccuracies in the existing *ab initio* PESs,²⁴⁻²⁶ in particular the height of the barrier, we consequently encourage further refinement and improvement of global FH₂ potential energy surfaces.

The most surprising and significant effect associated with the F* is the consequence of non-adiabatic couplings accompanying the treatment of the spin-orbit couplings. As discussed at length, the approach of an F atom in a ²P electronic state to molecular hydrogen gives rise to three PESs (1²A', 2²A', and 1²A'') (Fig. 2.4). The existence of spin-orbit and other non-adiabatic couplings among these PESs offer additional reaction pathways for the lowest electronic state, which are not present in a single-electronic-state treatment of the dynamics. These couplings alter the F+H₂ reaction dynamics. As described in Chapter 3, our calculations show that non-adiabatic couplings greatly reduce the backward scattering of HF products. After rescaling, the reduced backward scattering in the CM frame leads to enhanced forward and sideways scattering in the simulated laboratory ADs. Consequently, the three-state calculations (ASW PESs) are in better agreement with the classic molecular beam experiments of Neumark *et al.* Since backward scattering corresponds to collisions at small impact parameter, in future work, it would be worthwhile to investigate whether there is an associated increase in inelastic scattering at small impact parameters.

One major shortcoming in the present study is our shift of the collision energy in the theoretical simulations by 0.35 kcal/mol above the experimental value. This was done to compensate, albeit somewhat artificially, for an overly high barrier on the ASW PES. Ongoing *ab initio* studies²⁶ indicate the barrier on the ASW PES is roughly 0.25-0.30 kcal/mol too high. Comparisons between the SW and HSW

reaction probability for the F+H₂ reaction (Fig. 4.5) and among the SW, ASW and experimental excitation functions for the F+HD reaction (Figs. 4.2 and 4.4) suggest that the best (and simplest) way to compensate for the overestimation of the reaction barrier height on the ASW PES is to shift the collision energy upward by ~0.35 kcal/mol. Although this gives rise to satisfactory comparison with the experiment, we find some discrepancy still exists in the HF product channel. Because the effect of F* reactivity is small over the range of collision energy probed in the experiments, the remaining disagreement with experiment reflects residual inaccuracies in the ASW and SW PESs, which were based on *ab initio* calculations which are now nearly 10 years old.

Recent test calculations²⁶ suggests that it is now possible to decrease, substantially, the errors in the estimation of the F+H₂ reaction barrier and reaction exoergicity. Determination of a new, global, multi-state PES with similar methodology will provide the means for a quantitative understanding of the F+H₂ and F+HD reaction dynamics.

Through this dissertation, we find that the F* reactivity is either too small (Chapters 4 and 5, F+HD reactions) to make a significant contribution to the reaction or non-detectable (Figs. 3.9-3.10, F+H₂ reaction). Notwithstanding, experiment by Liu and co-workers⁸¹ show that the DCS for the F*+HD → HF(v'=3)+D reaction are essentially forward scattered, but the DCS for the reaction of F is more evenly distributed, at low collision energies ($E_c < 2.0$ kcal/mol). Because that the spin-orbit excited state lies 1.16 kcal/mol higher than the ground state (Fig. 5.2) and the energy threshold for F+HD → HF(v'=3)+D reaction is 1.32 kcal/mol (Fig. 5.2), the F* reactivity for the formation of HF(v'=3) products is comparable to the reactivity of F in this low energy range, as shown in the lower panel of Fig. 4.3 (HF, v'=3).

Giving the fact that the DCS of HF(v'=3) products from reaction of F*+HD is dominated by forward scattering and that its intensity is comparable to that of F in the

energy range $E_c < 2.0$ kcal/mol, we would expect the F* reaction to make a significant contribution to the forward scattering peaks in this energy range. Perhaps this is the reason why earlier calculations on the SW PES at 1.35 kcal/mol failed to reproduce the forward scattering feature of the HF($v'=3$) products.³⁵ Future calculations of DCSs for the F+HD reaction in this energy range will certainly predict an important role for the F* reaction.

Bibliography

1. M. H. Alexander, D. E. Manolopoulos, and H. J. Werner, *J. Chem. Phys.* **113**, 11084 (2000).
2. K. L. Kompa and G. C. Pimentel, *J. Chem. Phys.* **47**, 857 (1967); J. H. Parker and G. C. Pimentel, *J. Chem. Phys.* **48**, 5273 (1968).
3. R. D. Levine and R. B. Bernstein, *Molecular reaction dynamics and chemical reactivity*. (Oxford University Press, New York, 1987); S. C. Althorpe and D. C. Clary, *Annu. Rev. Phys. Chem.* **54**, 493 (2003).
4. D. E. Manolopoulos, *J. Chem. Soc., Faraday Trans.* **93**, 673 (1997).
5. K. Liu, R. T. Skodje, and D. E. Manolopoulos, *Phys. Chem. Comm.* **4**, 27 (2002).
6. V. Aquilanti, S. Cavalli, D. De Fazio, A. Volpi, A. Aguilar, X. Gimenez, and J. M. Lucas, *Phys. Chem. Chem. Phys.* **4**, 401 (2002).
7. Y. Zhang, T. X. Xie, K. L. Han, and J. Z. H. Zhang, *J. Chem. Phys.* **119**, 12921 (2003).
8. M. H. Alexander, Y.-R. Tzeng, and D. Skouteris, in *Chemical Reaction Dynamics*, edited by G. Lendvay (Kluwer Academic, Dordrecht, NL, 2003), pp. 45.
9. S. F. Wu, B. R. Johnson, and R. D. Levine, *Mol. Phys.* **25**, 839 (1973); S. F. Wu and R. D. Levine, *Mol. Phys.* **22**, 881 (1971); D. G. Truhlar and A. Kuppermann, *J. Chem. Phys.* **56**, 2232 (1972); D. G. Truhlar and A. Kuppermann, *J. Chem. Phys.* **52**, 3841 (1970).
10. D. M. Neumark, A. M. Wodtke, G. N. Robinson, C. C. Hayden, and Y. T. Lee, *J. Chem. Phys.* **82**, 3045 (1985).
11. J. F. Castillo, D. E. Manolopoulos, K. Stark, and H. J. Werner, *J. Chem. Phys.* **104**, 6531 (1996).
12. K. Stark and H. J. Werner, *J. Chem. Phys.* **104**, 6515 (1996).
13. F. J. Aoiz, L. Banares, V. J. Herrero, V. S. Rabanos, K. Stark, and H. J. Werner, *Chem. Phys. Lett.* **223**, 215 (1994).
14. F. J. Aoiz, L. Banares, B. Martínez-Haya, J. F. Castillo, D. E. Manolopoulos, K. Stark, and H. J. Werner, *J. Phys. Chem. A* **101**, 6403 (1997).

15. B. Hartke and H. J. Werner, Chem. Phys. Lett. **280**, 430 (1997).
16. J. F. Castillo, B. Hartke, H. J. Werner, F. J. Aoiz, L. Banares, and B. Martínez-Haya, J. Chem. Phys. **109**, 7224 (1998).
17. M. H. Alexander, G. Capecchi, and H. J. Werner, Science **296**, 715 (2002).
18. D. E. Manolopoulos, Science **296**, 664 (2002).
19. Y. R. Tzeng and M. H. Alexander, to be published.
20. Y. R. Tzeng and M. H. Alexander, to be published.
21. Y. R. Tzeng and M. H. Alexander, to be published.
22. R. T. Skodje, D. Skouteris, D. E. Manolopoulos, S. H. Lee, F. Dong, and K. Liu, J. Chem. Phys. **112**, 4536 (2000).
23. F. Dong, S. H. Lee, and K. Liu, J. Chem. Phys. **113**, 3633 (2000).
24. F. J. Aoiz, L. Banares, and J. F. Castillo, J. Chem. Phys. **111**, 4013 (1999).
25. D. H. Zhang, S. Y. Lee, and M. Baer, J. Chem. Phys. **112**, 9802 (2000).
26. H.-J. Werner, M. Kallay, and J. Gauss, to be published.
27. W. W. Harper, S. A. Nizkorodov, and D. J. Nesbitt, J. Chem. Phys. **116**, 5622 (2002).
28. See, for example, the excellent review article by Manolopoulos in Ref. 4.
29. In the system of atomic units, the specific charge e , electron mass m_e , and reduced Planck's constant (\hbar) are all equal to 1.
30. F. Jensen, *Introduction to computational chemistry*. (Wiley, Chichester ; New York, 1999).
31. B. T. Sutcliffe, in *Advances in Quantum Chemistry, Vol. 28* (1997), pp. 65; W. Kolos and L. Wolniewicz, J. Chem. Phys. **41**, 3663 (1964).
32. G. C. Schatz and A. Kuppermann, J. Chem. Phys. **65**, 4642 (1976).
33. D. Skouteris, J. F. Castillo, and D. E. Manolopoulos, Comput. Phys. Commun. **133**, 128 (2000).
34. F. T. Smith, Phys. Rev. **120**, 1058 (1960); F. T. Smith, J. Chem. Phys. **31**, 1352 (1959).
35. J. F. Castillo and D. E. Manolopoulos, Faraday Discuss. **110**, 119 (1998).

36. R. T Pack and G. A. Parker, *J. Chem. Phys.* **87**, 3888 (1987).
37. L. M. Delves, *Nucl. Phys.* **20**, 275 (1960); L. M. Delves, *Nucl. Phys.* **9**, 391 (1959).
38. M. Born and R. Oppenheimer, *Ann. d. Phys.* **84**, 457 (1927).
39. H. Lefebvre-Brion and R. W. Field, *Perturbations in the spectra of diatomic molecules*. (Academic Press, Orlando, 1986).
40. B. R. Johnson, *J. Comput. Phys.* **13**, 445 (1973); L. D. Thomas, M. H. Alexander, B. R. Johnson, W. A. Lester, J. C. Light, K. D. Mclenithan, G. A. Parker, M. J. Redmon, T. G. Schmalz, D. Secrest, and R. B. Walker, *J. Comput. Phys.* **41**, 407 (1981); D. E. Manolopoulos, *J. Chem. Phys.* **85**, 6425 (1986).
41. M. L. Dubernet and J. M. Hutson, *J. Phys. Chem.* **98**, 5844 (1994).
42. G. C. Schatz, *J. Phys. Chem.* **99**, 7522 (1995).
43. D. M. Brink and G. R. Satchler, *Angular momentum*, 2nd ed. (Clarendon P., Oxford, 1968); J. J. Sakurai and S. F. Tuan, *Modern quantum mechanics*, Rev. ed. (Addison-Wesley Pub. Co., Reading, Mass., 1994).
44. M. L. Goldberger and K. M. Watson, *Collision theory*. (Wiley, New York, 1965); W. H. Miller, *J. Chem. Phys.* **50**, 407 (1969); J. Z. H. Zhang and W. H. Miller, *J. Chem. Phys.* **91**, 1528 (1989).
45. C. S. Maierle, G. C. Schatz, M. S. Gordon, P. McCabe, and J. N. L. Connor, *J. Chem. Soc., Faraday Trans.* **93**, 709 (1997); G. C. Schatz, P. McCabe, and J. N. L. Connor, *Faraday Discuss.*, 139 (1998); T. W. J. Whiteley, A. J. Dobbyn, J. N. L. Connor, and G. C. Schatz, *Phys. Chem. Chem. Phys.* **2**, 549 (2000).
46. M. H. Alexander, G. Parlant, and T. H. Hemmer, *J. Chem. Phys.* **91**, 2388 (1989).
47. C. E. Moore, *Atomic Energy Levels, NSRDS-NBS 35*. (U. S. Government Printing Office, Washington, 1971).
48. The differential cross section is defined as the number of scattered particles detected by the detector per second per solid angle divided by the total number of incident particles per unit area per second per target particle, or in other words, divided by the rate of flow of incoming particles across unit area and by the total number of target particles. Consequently, the differential cross section has the unit of area/(solid angle).
49. L. I. Schiff, *Quantum Mechanics*, 3rd ed. (McGraw-Hill, New York, 1968).

50. G. L. Catchen, J. Husain, and R. N. Zare, *J. Chem. Phys.* **69**, 1737 (1978).
51. M. S. Child, *Molecular collision theory*. (Academic Press, London ; New York, 1974).
52. The LAB AD simulation is performed using the package developed by B. Martínez-Haya and F. J. Aoiz (Ref. 14).
53. T. T. Warnock and R. B. Bernstein, *J. Chem. Phys.* **49**, 1878 (1968); T. T. Warnock, *J. Chem. Phys.* **51**, 4682 (1969).
54. B.-H. Yang, H.-T. Gao, K.-L. Han, and J. Z. H. Zhang, *J. Chem. Phys.* **113**, 1434 (2000).
55. T. X. Xie, Y. Zhang, M. Y. Zhao, and K. L. Han, *Phys. Chem. Chem. Phys.* **5**, 2034 (2003).
56. J. C. Tully, *J. Chem. Phys.* **60**, 3042 (1974).
57. M. B. Faist and J. T. Muckerman, *J. Chem. Phys.* **71**, 233 (1979).
58. M. H. Alexander, H. J. Werner, and D. E. Manolopoulos, *J. Chem. Phys.* **109**, 5710 (1998).
59. G. C. Schatz, *Chem. Phys. Lett.* **150**, 92 (1988).
60. G. A. Parker and R. T Pack, *J. Chem. Phys.* **98**, 6883 (1993).
61. F. J. Aoiz, L. Banares, V. J. Herrero, V. S. Rabanos, K. Stark, and H. J. Werner, *J. Chem. Phys.* **102**, 9248 (1995); M. Faubel, B. Martínez-Haya, L. Y. Rusin, U. Tappe, J. P. Toennies, F. J. Aoiz, and L. Banares, *Chem. Phys.* **207**, 227 (1996).
62. R. T Pack, *J. Chem. Phys.* **81**, 1841 (1984).
63. J. T. Muckerman and M. D. Newton, *J. Chem. Phys.* **56**, 3191 (1972).
64. S. A. Nizkorodov, W. W. Harper, and D. J. Nesbitt, *Faraday Discuss.* **113**, 107 (1999).
65. A. Suits (unpublished).
66. V. Aquilanti, S. Cavalli, D. De Fazio, and A. Volpi, *J. Chem. Phys.* **109**, 3805 (1998); A. Kuppermann and R. Abrol, in *Role of Degenerate States in Chemistry* (2002), Vol. 124, pp. 283; N. Balucani, D. Skouteris, L. Cartechini, G. Capossa, E. Segolini, P. Casavechia, M. H. Alexander, G. Capecchi, and H.-J. Werner, *Phys. Rev. Lett.* **91**, 013201 (2003).

67. M. H. Alexander, G. Capecchi, and H.-J. Werner, *Faraday Disc. Chem. Soc.* **127**, in press (2004).
68. See, for example, the discrepancy in the F+H₂ reaction for scattering in the sideways direction as shown in Fig. 3 of Ref. 16 and the discrepancy in the F+HD reaction for the intensity of the resonant structure as shown in Fig. 1 of Ref. 23.
69. These fractional weights take into account the fine-structure splitting as well as the degeneracy factor ratio F:F* = 2:1.
70. M. Bettendorf, R. J. Buenker, S. D. Peyerimhoff, and J. Römelt, *Z. Phys. A.* **304**, 125 (1982).
71. Several steps are used to extrapolate the F* integral cross sections shown as the dashed lines in Fig. 4.2. First, we assume the excitation functions of F and F* for each (initial HD rotational state)-to-(product vibrational state) reaction channel share the same slope in the energy range of extrapolation. Second, we make sure the function obtained in the first step is differentiable at the junction of the calculated and extrapolated data. In general, extrapolation from the first step produces reasonable excitation functions. Only a few adjustments are required.
72. This feature is best seen from the plot of partial cross sections in Fig. 5 of Ref. 22.
73. E. E. Nikitin, in *Chemische Elementarprozesse*, edited by H. Hartmann (Springer, Berlin, 1968); V. Aquilanti and G. Grossi, *J. Chem. Phys.* **73**, 1165 (1980).
74. W. B. Chapman, B. W. Blackmon, and D. J. Nesbitt, *J. Chem. Phys.* **107**, 8193 (1997).
75. These fractional weights take into account the fine-structure splitting as well as the degeneracy factor ratio F:F* = 2:1.
76. J. W. C. Johns and R. F. Barrow, *P. Roy. Soc. Lond. A Mat.* **251**, 504 (1959).
77. D. U. Webb and K. N. Rao, *J. Mol. Spectrosc.* **28**, 121 (1968).
78. The panel labelled E_c=2.28 in Fig. 5 of Ref. 23 should be labeled 2.88 (K. Liu, private communication, 2003).
79. M. Hayes, M. Gustafsson, A. M. Mebel, and R. T. Skodje, *J. Chem. Phys.*, in press (2004).
80. S.-H. Lee and K. Liu, *J. Chem. Phys.* **111**, 6253 (1999); F. Dong, S.-H. Lee, and K. Liu, *J. Chem. Phys.* **115**, 1197 (2001).

81. S. H. Lee, F. Dong, and K. P. Liu, *J. Chem. Soc., Faraday Trans.* **127**, in press (2004).